Juel-4381

Jülich Center for Hadron Physics (JCHP)
Institut für Kernphysik (IKP)
COSY

Spin tune change induced by change of magnetic field

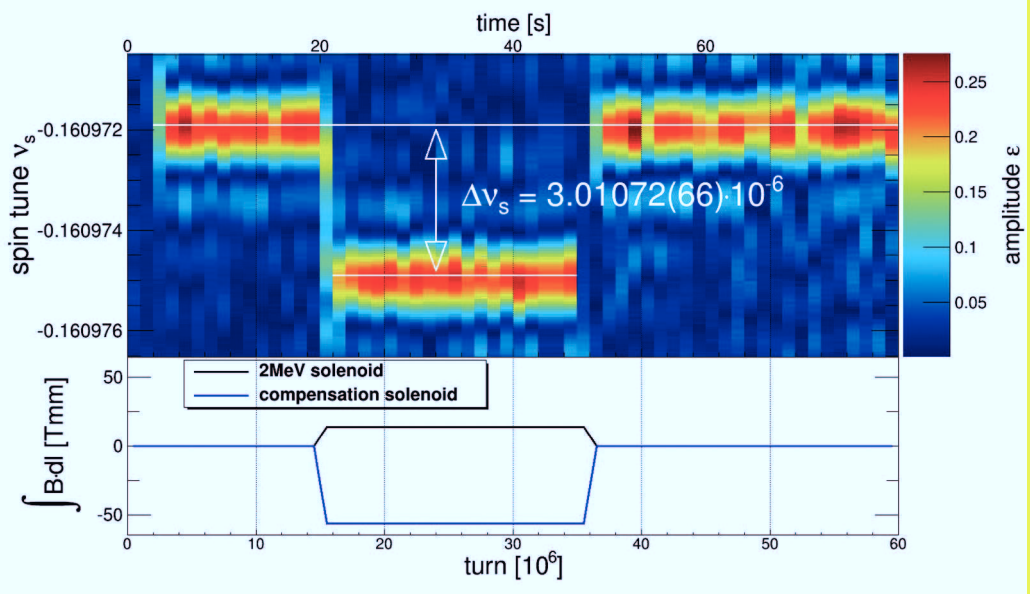

Annual Report 2014

JÜLICH
FORSCHUNGSZENTRUM

Annual Report 2014

Jülich Center for Hadron Physics / Institut für Kernphysik / COSY

Cover picture:
The cover picture shows a measurement of the spin tune change $\Delta\nu_s$, induced by a change of the magnetic field of two solenoids in COSY. A new technique was developed to determine the spin tune with unprecedented precision — up to $\sigma_{\nu_s} \approx 1 \cdot 10^{-10}$ — and, for the first time, continuously over a period of about 100 s. This technique made it possible to measure the influence of tiny changes in the accelerator setup in the course of a full accelerator cycle. This has been used during the JEDI beam time in September 2014 to probe the ring imperfections of COSY by applying artificial imperfections by means of the e-cooler solenoids. A cycle setup with a long spin coherence time and an electron cooled beam was applied: after 20 seconds measurement time the strength of the e-cooler compensation solenoid and the strength of the main solenoid of the 2 MeV e-cooler were changed for 25 seconds. By varying the changes of the solenoids and measuring the corresponding spin tune change, the longitudinal component of the stable spin axis can be determined at the positions of the solenoids. While spin tune changes down to $\Delta\nu_s \approx 10^{-8}$ have been measured, the given example shows a setup for which the resulting spin tune jump is clearly visible in the plot. (For details on the spin tune measurement, see also page 17 in this annual report.)

Contents

Preface

An important milestone has been reached in 2014: The evaluation of both the experimental and the theoretical proposal for the third period of programme-oriented funding (PoF) of the Helmholtz Association resulted in excellent reports on the proposals presented by IKP. Consequently the base funding of the institute up to the end of 2019 has been secured.

The institute thanks Prof. Dr. R. Maier for his strong scientific leadership of IKP-4 during the past thirty years, which has made a major contribution to the success of the IKP. He will continue to support the institute by his ideas and advice. We thank Prof. A. Lehrach for his fine interim management of IKP-4 after Prof. Maier's retirement in early 2014. On December 1, IKP has welcomed the new director of IKP-4, Prof. Mei Bai.

In the next five years, COSY will concentrate on two activities. In preparation of FAIR, COSY will test components of the high energy storage ring HESR and the detector system PANDA. Within the Jülich-Aachen research alliance (JARA), a precursor experiment for the determination of the electromagnetic dipole moment (EDM) of charged particles in a storage ring will be developed by the JEDI collaboration. The experimental activities in hadron physics at COSY have ended in 2014. The program advisory committee (PAC) has completed its mission in 2014. The research center thanks both present and past members for their expert advice in choosing the most promising experiments. Beam time at COSY remains a precious commodity. The new COSY beam advisory committee (CBAC) will help to make the future COSY activities a success.

In 2014 the following experimental and theoretical highlights have been achieved:

FAIR: Numerous test measurements of systems for PANDA and other FAIR eperiments have been performed. These were instrumental e.g. to refine the Straw Tube Tracker readout system in a high rate environment where both position and specific energy loss are measured. Furthemore, successful tests of silicon strip sensors and readout electronics, including the ToPix4 ASIC were performed.

EDM: The JEDI collaboration has achieved a high-precision determination of the spin tune using the EDDA detector: 10^{-8} in a macroscopic time interval of $\Delta t = 2$ sec. Spin coherence times of about 1000 sec have been reached.

Resonance in dipionic fusion: The analysing power for the double-pionic fusion reaction $\vec{n}p \to d\pi^0\pi^0$ near 90^0 exhibits a structure near 2.4 GeV not seen in the published SAID partial wave analysis. While such a resonant structure was found previously in other reaction involving two pions, this is the first time it is seen as a genuine s-channel resonance. This investigation was made possible by the unique combination of the WASA detector system and the polarized beam at COSY.

Scattering length η'-proton: The excitation function of the reaction $pp \to pp\eta'$ was measured with a precision $\Delta Q = 0.1$ MeV down to $Q = 0.76$ MeV, using the high mass resolution of the COSY-11 detector system and the cooled proton beam. The η' proton scattering length was determined as $a = (0.00 \pm 0.43 + i(0.37 \pm 0.4))$ fm.

Theory, hadron physics: The nucleon-nucleon interation at fifth order in chiral effective

field theory has been worked out, confirming a good convergence of the chiral expansion. This work paves the way for *ab initio* calculations of few- and many-body systems.

Theory, EDM: The first complete calculations of both two- and three-nucleon interactions contributing to the EDMs of the deuteron, helion, and triton have been achieved in chiral effective field theory. This allows systematic studies of the EDMs of light nuclei which may discriminate between effects due to the theta term of QCD and to minimal left-right symmetric interactions.

It is a pleasure to thank our national and international collaboration partners for their activities and support and especially our coworkers in Jülich for their commitment.

Jülich, February 2015 James Ritman

1 Introduction – Physics program and strategy

1.1 Proton and Deuteron Beams

The major part of the experimental program of the Institut für Kernphysik (IKP) during 2014 was conducted at the cooler synchrotron and storage ring facility COSY on our campus at Forschungszentrum Jülich (FZJ). Proton and deuteron beams were used to finalize the hadron physics experiments at the WASA detector. The ANKE and TOF facilities were still operational but no further measurements were performed. With the end of 2014, IKP and the management of FZJ have decided to terminate the hadron physics program at COSY. An increasing fraction of beamtime was devoted to preparatory measurements for FAIR, comprising detector tests for the CBM and the PANDA facilities, as well as accelerator equipment investigations. For these investigations, both the internal target stations and the extracted beamlines were used: the KOALA-collaboration performed first tests using the ANKE cluster jet target, and tests of detector components for CBM and PANDA were conducted in the NEMP, TOF and BIG KARL areas. Once the Siberian Snake, which has been ordered some time ago, will be delivered, it is planned to perform a longitudinal spin-filtering experiment with (originally unpolarized) protons at the PAX internal target place. In addition, a significant amount of time with polarized deuteron beams was used for research and development studies for the EDM-project (see below).

1.2 Antiprotons

Preparations for the design and construction of the High Energy Storage Ring (HESR) at FAIR (Facility for Antiproton and Ion Research) at GSI Darmstadt as well as for the PANDA internal experiment with antiproton beams are one more major activity of IKP. Factory acceptance tests of HESR magnets have been finished and the delivery of first dipoles and quadrupoles to Jülich, where they will be further tested, assembled and stored, is expected soon. Similarly, the construction of components for the PANDA tracking detectors has started. It will take a few more years until antiproton beams will be available at FAIR, but since the required technologies (storage ring, polarized atomic beam source (ABS) plus storage cell) are available, it is appropriate to start thinking and preparing for the next step, which could be, e.g., polarized antiprotons. The PAX-collaboration intends to establish spin-filtering as the method to produce an intense beam of polarized antiprotons in a storage ring. In a first step, corresponding tests with protons at COSY are conducted and foreseen (see above). Whether the collaboration will subsequently continue its preparations with antiprotons at CERN/AD or at another storage ring, for example at FAIR, remains to be further explored.

1.3 Precision Experiments

After termination of the hadron reaction physics program (see above), IKP is preparing to exploit the uniqueness of the COSY storage ring for a new project, called JEDI (Jülich Electric Dipole moment (EDM) Investigations), which aims to search for EDMs of charged particles (proton, deuteron,...). The idea is to store a beam of particles, polarized along the momentum direction, in a ring, apply a radial electric field and observe the slow rotation of the polarization vector into the vertical direction. While conceptually straightforward, such a measurement will constitute enormous technological and methodological challenges. IKP has therefore developed a stepwise approach, in which COSY plays a central role: (i) performing R&D, e.g., to investigate spin coherence time of a stored beam, to establish ways to precisely determine the beam's spin tune as well as its polarization, (ii) conducting a so called "precursor-experiment" with the available conventional (magnetic) storage ring, and (iii) design (and possibly build) a new dedicated precision storage ring to search for EDMs with unprecedented sensitivity ($\sim 10^{-29}$ e cm), exploiting COSY as an injector.

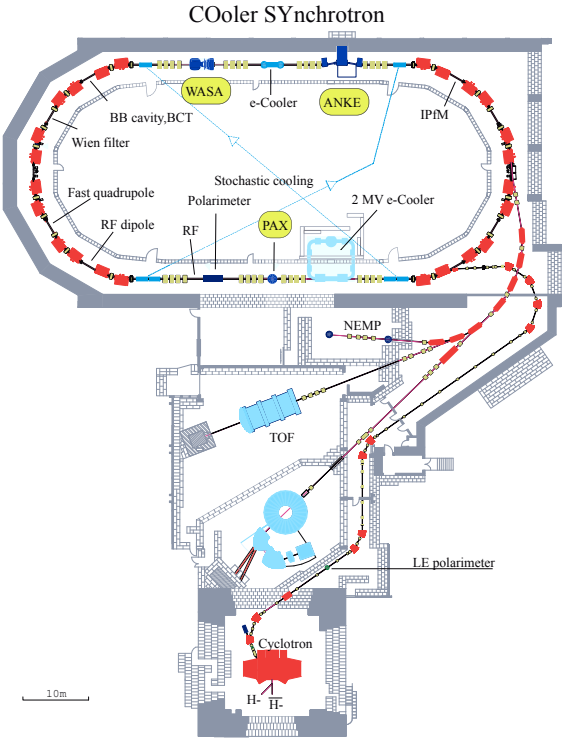

Fig. 1: The Cooler Synchrotron COSY indicating the experiments and installations as of 2014.

2 COSY - Highlights from Hadron Physics

2.1 The neutron-proton elastic amplitude studies in the $\vec{d}p$ and $p\vec{d}$ charge-exchange reactions

It is a consequence of the nucleon spins that five complex amplitudes are needed to describe neutron-proton elastic scattering. This means that, above the pion production threshold, at least nine independent measurements are required at each scattering angle to allow an unambiguous partial wave decomposition. Some of the resulting observables, which could depend on up to three spin projections, are difficult to determine directly and values may have to be obtained indirectly through combinations of other measurements. It was shown that the tensor analyzing power in the deuteron charge exchange on hydrogen, $\vec{d}p \to \{pp\}_s n$, is closely linked to the spin transfer in neutron-proton large angle scattering, $\vec{p}n \to \vec{n}p$, provided that the excitation energy E_{pp} in the final diproton is very low. Due to the Pauli principle the two protons are then dominantly in the $^1S_0$ state with antiparallel spins, here denoted by $\{pp\}_s$. There is thus a spin-isospin flip to this state from the initial deuteron.

Information on the neutron-proton scattering amplitudes can also be obtained through measurements of vector analyzing powers and spin correlations in the $\vec{d}\vec{p} \to \{pp\}_s n$ reaction. Experiments of this type were carried out at deuteron beam energies of $T_d = 1.2$, 1.6, 1.8, and 2.27 GeV to investigate the np amplitudes at neutron kinetic energies of $T_n \approx \frac{1}{2}T_d = 600$, 800, 900, and 1135 MeV. The transverse spin correlations and deuteron and proton analyzing powers were investigated and the results were found to be consistent with modern partial wave solutions at $T_n = 600$, 800, 900 MeV, while failing badly at 1135 MeV. These conclusions reinforce those already drawn on the basis of the deuteron tensor analyzing power results.

A similar investigation was carried out with a vector polarized deuteron beam at $T_d = 726$ MeV in a very high statistics experiment, where small effects could be studied in detail. Since it is expected that the np partial wave amplitudes should be fairly reliable at 363 MeV, this is the ideal testing ground to establish quantitatively the validity of the theoretical modelling of deuteron charge exchange. The measurements were undertaken with the ANKE magnetic spectrometer in parallel with those used to determine the spin correlation in the quasi-free $\vec{n}\vec{p} \to \{pp\}_s\pi^-$ reaction.

The resulting $dp \to ppn$ data were binned in momentum transfer q between the deuteron and diproton and the diproton excitation energy E_{pp} (typically $E_{pp} < 3$ MeV).

For vector polarized deuteron beams, the ratio of the numbers of polarized $N(q,\phi)$ to unpolarized $N^0(q)$ events has the form:

$$\frac{N(q,\phi)}{N^0(q)} = 1 + p_p A_y^p(q)\cos\phi + \tfrac{3}{2}p_d A_y^d(q)\cos\phi + \\ + \tfrac{3}{4}p_d p_p[(1+\cos 2\phi)C_{y,y}(q) + (1-\cos 2\phi)C_{x,x}(q)], \quad (1)$$

where the y direction is perpendicular to the COSY plane and the x direction is in this plane but perpendicular to the beam direction. The azimuthal angle ϕ is defined by $\tan\phi = y/x$.

By studying the ϕ dependence of the count rates for four combinations of beam and target polarisations it is possible to extract separately the values of the proton and deuteron vector analyzing powers as well as the two spin correlations. The corresponding results are shown in Figs. 2 and 3.

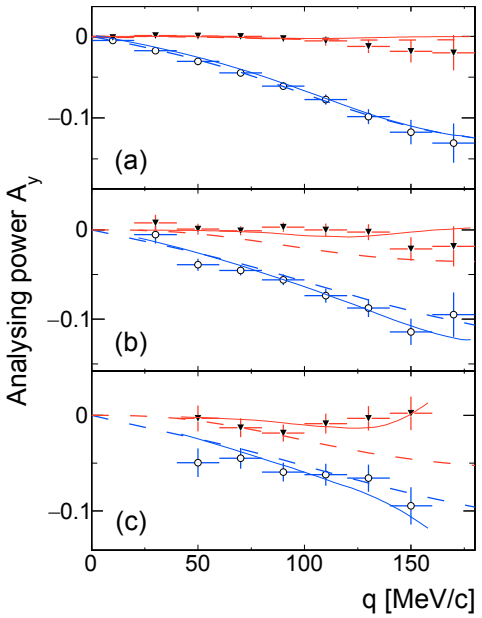

Fig. 2: Values of the deuteron (vector) analyzing power A_y^d (black inverted triangles) and proton analyzing power A_y^p (blue open circles) for the $dp \to \{pp\}n$ reaction at 726 MeV. Data were placed in bins of (a) $E_{pp} < 2$ MeV, (b) $4 < E_{pp} < 6$ MeV, and (c) $8 < E_{pp} < 10$ MeV. The curves are impulse approximation estimates folded with experimental acceptance. These used the current SAID neutron-proton partial wave solution as input. The dashed lines neglect the predicted dependence on the angle between the relative momentum in the diproton and the momentum transfer. The model predictions for this are included in the solid lines.

In impulse approximation the amplitude for the $dp \to \{pp\}n$ charge-exchange reaction is proportional to the $np \to pn$ charge-exchange amplitude times a form factor that represents the overlap of the initial deuteron wave function with that of the outgoing diproton. The elementary $np \to pn$ amplitude can be written in terms of five

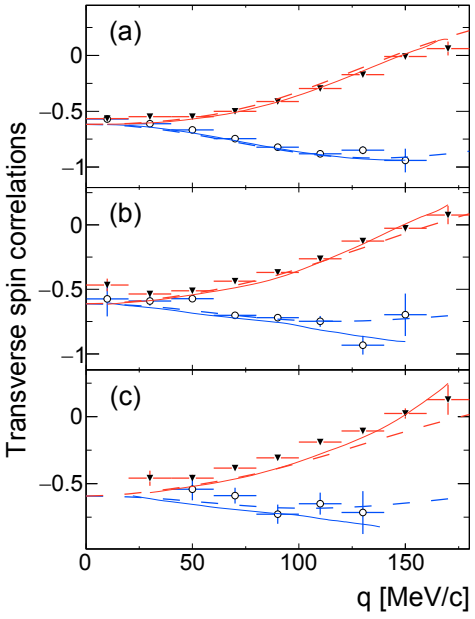

Fig. 3: Values of the spin correlations $C_{y,y}$ (black inverted triangles) and $C_{x,x}$ (blue open circles) for the $dp \to \{pp\}_s n$ reaction at 726 MeV. The conventions are identical to those of Fig. 2.

scalar amplitudes in the np c.m. frame as

$$f_{np} = \alpha(q) + i\gamma(q)(\vec{\sigma}_1 + \vec{\sigma}_2)\cdot\vec{n} + \beta(q)(\vec{\sigma}_1\cdot\vec{n})(\vec{\sigma}_2\cdot\vec{n}) + \delta(q)(\vec{\sigma}_1\cdot\vec{m})(\vec{\sigma}_2\cdot\vec{m}) + \varepsilon(q)(\vec{\sigma}_1\cdot\vec{l})(\vec{\sigma}_2\cdot\vec{l}), \quad (2)$$

where $q = \sqrt{-t}$ is the three-momentum transfer between the initial neutron and final proton and the Pauli matrices $\vec{\sigma}$ are sandwiched between neutron and proton spinors. Values of the amplitudes can be extracted from the current partial wave solution of the SAID group.

Although the resulting $dp \to \{pp\}n$ amplitudes can be evaluated reliably with modern deuteron and pp wave functions, it is useful for a qualitative discussion to consider the results if one considers only the pp $^1S_0$ configuration.

In the $^1S_0$ limit the spin correlations at $q = 0$ are linked to a combination of neutron-proton spin-correlation and spin-transfer parameters, through

$$C_{x,x}(0) = C_{y,y}(0) = \frac{2[A_{00nn}(\pi) - D_{n0n0}(\pi)]}{3 - K_{0l l0}(\pi) - 2K_{0nn0}(\pi)}. \quad (3)$$

The curves shown in Figs. 2 and 3 represent the full impulse approximation calculations and these lead to a slight deviation from the $^1S_0$ prediction of $A_y^d = 0$ due to the finite value of E_{pp}.

The general shapes of the $C_{x,x}/C_{y,y}$ predictions in Fig. 3 are very much in line with the measured data, though there are significant quantitative differences. $C_{y,y}$ changes sign, as one would expect from the simple one-pion-exchange contribution to the δ amplitude, though this happens at a few MeV/c higher than the prediction. The details of this study can be found in the recent submission: arXiv:nucl-ex/1255.2465.

The major constraint on the ANKE program is the maximum deuteron energy of 2.3 GeV available at the COSY. To continue the studies to higher energies, where there is great uncertainty in the neutron-proton amplitudes, the experiments have to be carried out in inverse kinematics, with a proton beam incident on a polarized deuterium target.

When measuring the $\vec{d}p \to \{pp\}_s n$ reaction with a polarized deuteron beam, by detecting the two fast protons in the ANKE forward detector, it was possible to investigate regions where the momentum transfer q between the deuteron and the diproton and the diproton energy E_{pp} were both small. This is no longer the case in inverse kinematics when the two slow protons are measured using a pair of Silicon Tracking Telescopes (STT) placed symmetrically to the left and right of the cell target. If the two protons are measured in the same STT, then E_{pp} can be small but the momentum transfer has a lower limit of $q \gtrsim 2 \times 70$ MeV/c.

Data were taken by flipping the target deuteron polarisations between different modes. The results of the two deuteron tensor analyzing powers are shown in Fig. 4 with the standard E_{pp} cut. They are there compared with ANKE data at lower momentum transfers and also with impulse approximation predictions. With the $E_{pp} <$ 3 MeV cut, the $^1S_0$ state dominates at small q but P and higher waves will become more important as q increases.

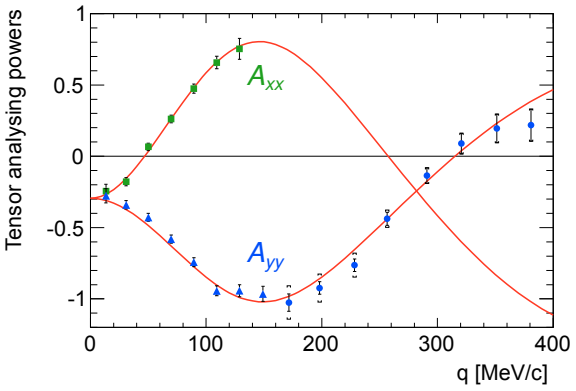

Fig. 4: Tensor analyzing powers A_{xx} (green squares) and A_{yy} (blue triangles) of the $\vec{d}p \to \{pp\}_s n$ reaction with $E_{pp} < 3$ MeV from the earlier deuteron beam measurements at 600 MeV/nucleon. The current A_{yy} results (blue dots) were obtained in inverse kinematics. The curves are impulse approximation predictions.

The new A_{yy} results of Fig. 4 join quite smoothly onto the lower momentum transfer data obtained with the polarized deuteron beam. Furthermore the data seem to be essentially consistent with impulse approximation predictions. Having shown that a polarized deuterium cell can be successfully used for charge-exchange studies in an energy region where the neutron-proton amplitudes are well understood, measurements at higher energies are

very important. The details of this program can be found in the recent publication: Phys. Lett. B 741 (2015) 305.

2.2 The $d^*(2380)$ dibaryon resonance – from observation to verification

The trace to this resonance was initially laid by the so-called ABC-effect, which denotes an unusual low-mass enhancement in the invariant-mass spectrum of a pion pair produced in fusion reactions to light nuclei. The first exclusive and kinematically complete measurements of solid statistics on this issue were carried out with WASA – at that time still at CELSIUS. As a result of these new data the idea was born that the ABC effect could be the result of a quasi-bound Δ pair. If this hypothesis was true then the total cross section should exhibit some resonance structure. Indeed, first measurements of the basic double pionic fusion reaction $pn \to d\pi^0\pi^0$ – with neutrons being used in the quasi-free mode – exhibited some peak structure in the total cross section in correlation with the appearance of the ABC effect.

With having WASA moved to COSY this reaction channel was reexamined not only with much better precision over the full reaction phase space, but also with two orders of magnitude higher statistics. As a result a pronounced Lorentzian emerged in the data for the total cross section (blue dots in the top panel of Fig. 5) at an energy of 2.37 GeV with a width of about 70 MeV. From the angular distributions spin-parity of this structure could be determined to be $J^P = 3^+$.

Since in two-pion production initiated by pp collisions no such structure was observed, this Lorentzian needed to be of purely isoscalar nature. In a subsequent run this hypothesis could be confirmed by measuring simultaneously the reactions $pn \to d\pi^0\pi^0$, $pp \to d\pi^+\pi^0$ and $pn \to d\pi^+\pi^-$. Whereas the first reaction is purely isoscalar, the second one (black squares in top panel of Fig. 5) is purely isovector and does not exhibit any resonance structure. The third reaction (red triangles) is isospin mixed and shows the resonance effect on top of the large isovector background as expected from isospin decomposition.

If this phenomenon constituted a genuine isoscalar resonance, than it needed to show up also in other two-pion production reactions, where the nucleons do not fuse, but where also an isoscalar reaction component was present. Therefore also measurements of the reactions $pn \to pn\pi^0\pi^0$ and $pn \to pp\pi^0\pi^-$ were carried out. The WASA results are shown as blue dots in second and third panels from top in Fig. 5. Since we deal here with a four-body phase space in the exit channel, the cross section starts steeply rising from the threshold. The black solid lines give the description of conventional processes. As we see, the calculations fall low compared to the data in both channels. However, by adding the hypothetical resonance (red dashed lines) as deduced from isospin coupling and explicit theoretical calculations, respectively, we obtain a quantitative description of the data.

Though the hypothesis of an isoscalar resonance is ob-

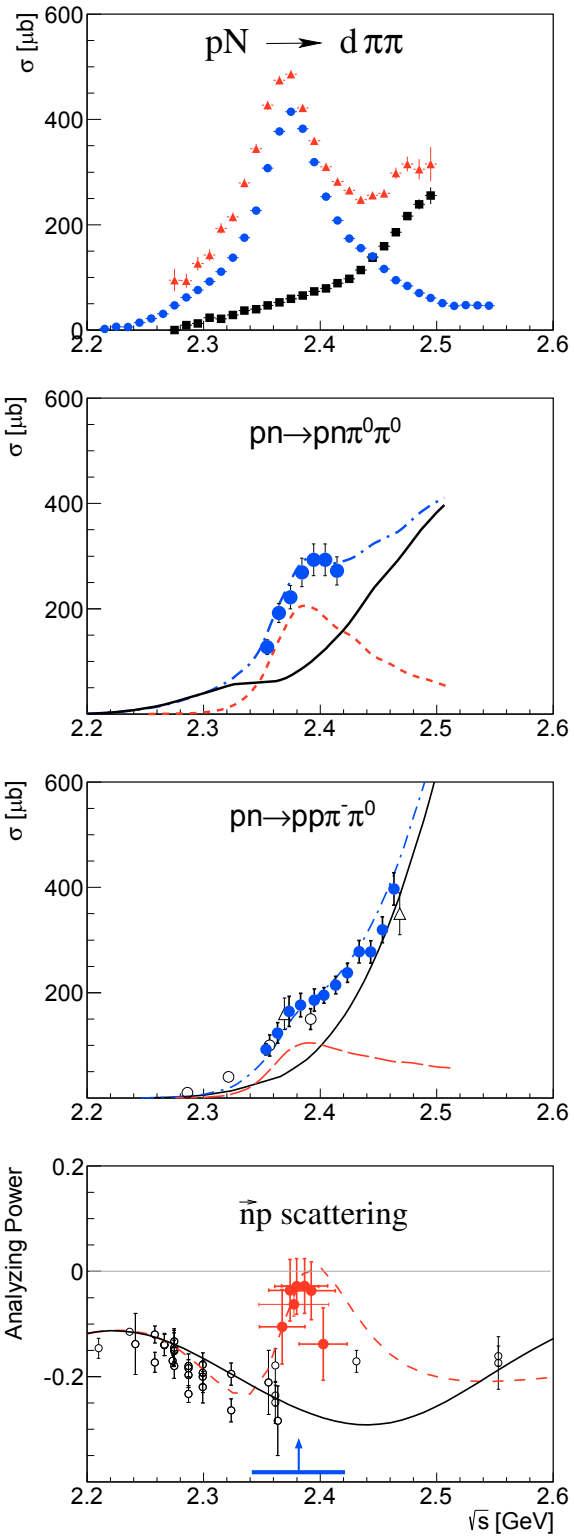

Fig. 5: $d^*(2380)$ in various reaction channels. Top: Total cross sections for the double-pionic fusion processes $pn \to d\pi^+\pi^-$ (red), $pn \to d\pi^0\pi^0$ (blue) and $pp \to d\pi^+\pi^0$ (black). Second from top: Total cross section of the non-fusion double-pionic reaction $pn \to pn\pi^0\pi^0$. Third from top: Total cross section of the non-fusion double-pionic reaction $pn \to pp\pi^0\pi^-$. Bottom: Analyzing power of $\vec{n}p$ scattering near 90°.

viously in agreement with all two-pion production channels, this is not yet a proof of a genuine s-channel resonance. For this end it has to be sensed also in the entrance channel, *i.e.* in elastic np scattering. From the measured decay branchings into the various two-pion channels we can estimate the resonance contribution in the np channel to be in the order of 170 μb, which is tiny compared to the total np cross section of nearly 40 mb. Hence the only observable, which could sense such a tiny contribution is the analyzing power, since it is composed of only interference terms in the partial waves. With having $I(J^P) = 0(3^+)$ we expect the resonance effect to be in the ${}^3D_3 - {}^3G_3$ coupled partial waves. Since it should contribute in angular dependence of the analyzing power like the associated Legendre polynomial P_3^1, the resonance effect is expected to be largest at 90°, where the differential cross section is smallest.

Unfortunately, there were no analyzing power data available in the energy region of interest from previous experiments. The situation is illustrated in the bottom panel of Fig. 5, which exhibits the energy dependence of the analyzing power at a scattering angle of 83°, *i.e.* close to 90°, and where all the analyzing power data available from previous experiments are plotted by black symbols.

Hence, in a final experiment on this issue, polarized np scattering was measured at WASA in inverse kinematics by having a polarized deuteron beam hitting the hydrogen pellet target. By detecting the fast spectator proton in the forward detector and the scattered proton and neutron in forward as well as central detectors of WASA we achieved again kinematically complete measurements covering the full angular region over the energy region of interest.

The new data from WASA are depicted for a scattering angle of 83° in the bottom panel of Fig. 5 by red symbols. They deviate substantially from the results of previous experiments at lower energies and clearly exhibit some resonance-like structure – right at the position were we expect the resonance signal. The SAID partial-wave solution SP07 based just on previous experimental results is shown in Fig. 5, bottom panel as black solid line. It can not account for the new WASA results. However, when these are included in the SAID data base, they produce a new solution, which contains a pole in the coupled ${}^3D_3 - {}^3G_3$ partial-waves at $(2380 \pm 10) + i(40 \pm 5)$ MeV. The new solution is shown in Fig. 5, bottom panel, by the red dashed line.

The fact that the new WASA data produce a pole in the SAID partial-wave analysis corresponding to a $I(J^P) = 0(3^+)$ resonance in the np system at the designated position certifies the resonance structure observed in two-pion production to be a genuine s-channel resonance. For its denotation we chose the expression $d^*(2380)$ following the nomenclature used for nucleon excitations.

As it turns out after all the WASA measurements, the golden channel for the discovery of $d^*(2380)$ is the $d\pi^0\pi^0$ channel, since there the background relative to the resonance signal is by far lowest, see Fig. 5. However, there were no data at all for this channel from previous experiments. This is not of a surprise, since before WASA there was no detector setup available on a suited hadron accelerator, which could have covered the full reaction phase space of the many emitted charged and neutral particles. So it was left solely to the unique combination of WASA and COSY to investigate this channel in very detail and thus observe a resonance signal in an unprecedented clarity, which in turn urged us to a deeper inspection. All WASA measurements on this issue have been published meanwhile in peer-review journals – see, *e.g.*: Phys. Rev. Lett. **106** (2011) 242302, Phys. Rev. C **86** (2012) 032201(R), Phys. Lett. B **721** (2013) 229, Phys. Rev. C **88** (2013) 055208, Phys. Rev. Lett. **112** (2014) 202301, Phys. Rev. C **90** (2014) 035204, Phys. Rev. C **91** (2015) 015201, Phys. Lett. B **743** (2015) 325

2.3 Observation of the isovector dibaryon-like resonance state with mass of 2181 MeV/c^2

A problem of resonances in the dibaryon systems arose about 50 years ago but yet stays actual at present. It became exciting since prediction of such a phenomenon in the framework of quarkbag models. The corresponding extensive search for the short-range six-quark objects has led to discovery of resonances in the ${}^1D_2$, ${}^3F_3$ and ${}^3P_2$ states of the elastic pp scattering. Position of the corresponding poles in the complex energy plane close to the $\Delta(1232)N$ branching line led to a commonly accepted interpretation as conventional states of the ΔN channel. Nevertheless, quark models are used last decades to describe these dibaryon systems too. Since the physical nature of these resonances stays rather uncertain, the experimental and theoretical study of them continues to be actual. The observed isovector resonances are highly inelastic so their study is preferable in a single pion production processes. In this respect, new options provides the reaction $pp \to \{pp\}_S\, pi^0$, where diproton $\{pp\}_S$ is a ${}^1S_0$ proton pair. Non-separated contributions of the ${}^1D_2p$, ${}^3F_3d$, ${}^3P_2d$ transitions form a famous peak around 560 MeV in the cross section of the $pp \to d\pi^+$ reaction. For the diproton channel only the ${}^3P_2d$ transition is allowed from this set and it gives an immediate way for study the P-wave ΔN resonance interaction.

The earlier ANKE at COSY data for the $pp \to \{pp\}_S\pi^0$ differential cross section $d\sigma/d\Omega$ in the Δ excitation region [Phys. Lett. B **661** 22 (2008); Phys. Lett. B **712** 370 (2012)] were supplemented by additional points. First time the analyzing power A_y of the reaction has been measured in this energy range. They are well described by the equations:

$$\frac{d\sigma}{d\Omega} = \frac{d\sigma_0}{d\Omega}\left(1 + \kappa \sin^2\theta_{pp}\right),\ A_y = \frac{A_y^{\max}\sqrt{1+\kappa}\sin 2\theta_{pp}}{1+\kappa\sin^2\theta_{pp}},$$

where $d\sigma_0/d\Omega$ means cross section at the zero angle, κ is a slope parameter and $A_y^{\max}$ is a maximal value of A_y, acquired when $\sin^2\theta = 1/(2+\kappa)$. Figure 6 exhibits some

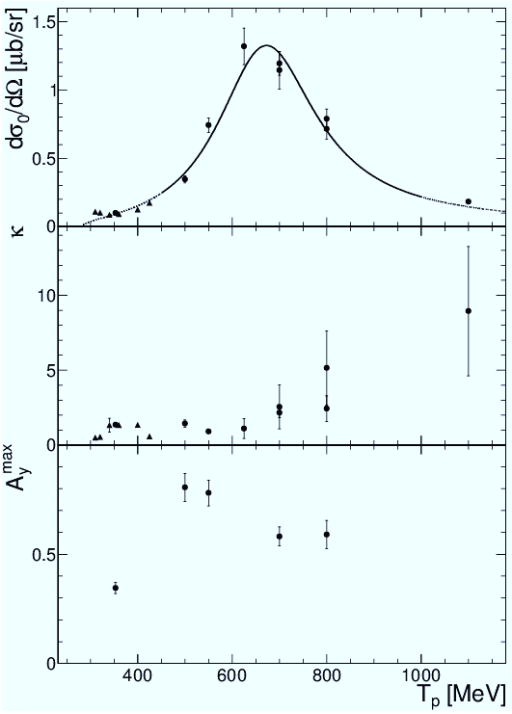

Fig. 6: Cross section at zero angle $d\sigma_0/d\Omega$, angular distribution slope parameter κ and maximal analyzing power $A_y^{\max}$ (top to bottom). ▲ — WASA@CELSIUS, • — ANKE@COSY data.

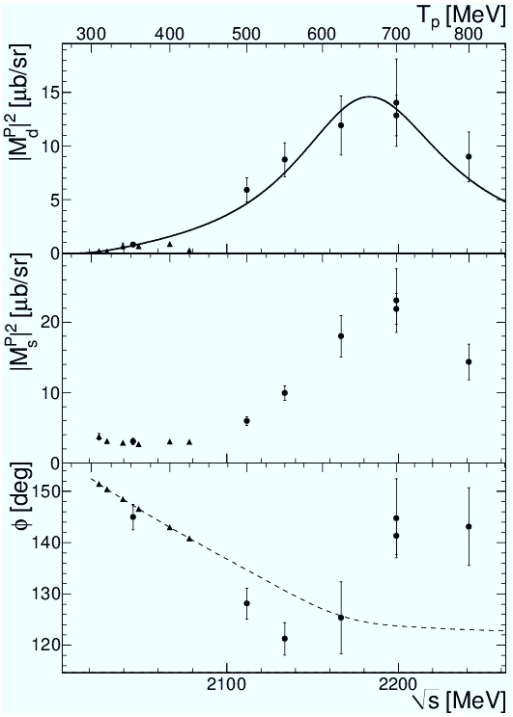

Fig. 7: The amplitudes squared of two dominant transitions and their relative phase (from top to bottom). The data are marked as in Fig. 6. The curve for $\left|M_d^P\right|^2$ is a modified Breit-Wigner function. The dashed curve — the relative phase of the $pp \to pp$ scattering ${}^3P_0$ and ${}^3P_2$ transitions.

prominent features of the data: a clean peak of the forward differential cross section around 675 MeV; a slow variation of the slope parameter with a dip at the zero angle; a significant analyzing power.

If to assume that in the $\Delta(1232)$ excitation region the M_d^F amplitude and the ones corresponding to the g and higher pion waves are small for the $pp \to \{pp\}_S\pi^0$ reaction similarly to the $pp \to d\pi^+$ one, the obtained data can be described in terms of only two amplitudes, M_s^P and M_d^P, corresponding to the transitions ${}^3P_0 \to {}^1S_0 s$ $(J^P = 0^-)$ and ${}^3P_2 \to {}^1S_0 d$ (2^-). Figure 7 shows that $\left|M_d^P\right|^2$ is well reproduced by the Breit-Wigner dependence corrected by the Blatt-Weisskopf penetration factor for proximity of the resonance to the threshold. $\left|M_s^P\right|^2$ has also a significant enhancement in the Δ excitation region. Relative phase between the amplitudes follows the Watson theorem dependence near the threshold and differs from that already at about 400 MeV. Position of the $I(J^P) = 1(2^-)$ resonance, 2181 ± 8 MeV/c^2, ($\Gamma = 108 \pm 24$) indicates on about 50 MeV strength attraction in the P-wave *varDeltaN* pair if to interpret the resonance in terms of the meson-baryon approach.

2.4 Isospin effects in the exclusive $dp \to {}^3\mathrm{He}\pi^+\pi^-$ reaction

Two-pion production in nuclear scattering processes has been the subject of intensive research for many years, especially due to the appearance of the so-called ABC effect. Though distinct progress in its understanding has been made, there are still important questions to be answered. In particular, the role of the Roper N^* isobar in double pionic fusion is so far only poorly examined. The excitation and decay of the Roper in the $dp \to {}^3\mathrm{He}\pi^+\pi^-$ reaction can lead to a difference between the $M_{^3\mathrm{He}\pi^+}$ and $M_{^3\mathrm{He}\pi^-}$ invariant-mass distributions. The reason for this may be found in the difference between the Clebsch-Gordan coefficients for the decay channels $N^* \to \Delta\pi^- \to N\pi^+\pi^-$ and $N^* \to \Delta\pi^+ \to N\pi^-\pi^+$. With the benefit of the good momentum resolution of the ANKE detector, the resulting differences in the $M_{^3\mathrm{He}\pi}$ invariant mass spectra could be investigated more quantitatively than in the pioneering WASA experiment.

The ANKE experiment was carried out at an excess energy of 265 MeV with respect to the reaction threshold. Events with coincident hits of ^{3}He nuclei in the forward detection system and at least one of the pions in the negative or positive detection system were used in the analysis. The data were modeled in terms of the sequential decay $N^*(1440) \to \Delta(1232)\pi \to N\pi\pi$, which was also used as an input for a Monte Carlo based correction of the limited detector acceptance. The explicit form of the ansatz is:

$$\sigma \propto \left| \left[m_\pi^2 + \alpha \vec{k}_1 \cdot \vec{k}_2 \right] \left(3\Delta^{++} + \Delta^0 \right) \right|^2, \qquad (4)$$

where $\alpha = 0.2 + i0.3$ is a fitted parameter, $\vec{k}_i$ are the pion

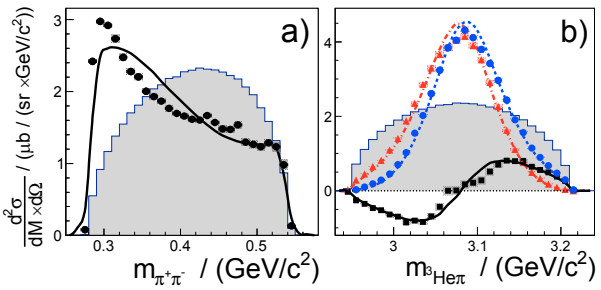

Fig. 8: Centre-of-mass double-differential cross sections for the $dp \to {}^3\mathrm{He}\pi^+\pi^-$ reaction averaged over $143^\circ < \vartheta^{CMS}_{^3\mathrm{He}} < 173^\circ$ in terms of the invariant masses (a) $M_{\pi^+\pi^-}$, (b) $M_{^3\mathrm{He}\pi^+}$ (blue circles), and $M_{^3\mathrm{He}\pi^-}$ (red triangles). The differences between the two $M_{^3\mathrm{He}\pi}$ distributions are plotted as black squares. The curves correspond to Eq. (4) and the shaded areas are phase-space distributions, normalised to the integrated cross section.

momenta in CMS, and Δ^{++} and Δ^0 are Breit Wigner functions of the respective nucleon excitation. The factors 3 and 1 reflect different isospin couplings coming from the Roper decay.

The differential cross section for the ^{3}He $dp \to {}^3\mathrm{He}\pi^+\pi^-$ reaction, averaged over the production angle interval $143^\circ < \vartheta^{CMS}_{^3\mathrm{He}} < 173^\circ$ was determined to $\langle d\sigma/d\Omega^{CMS}\rangle = 480 \pm 3 \pm 35$ nb/sr, where the first error is statistical and the second systematic.

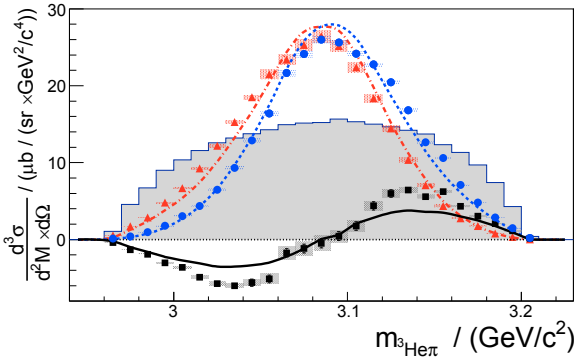

Fig. 9: $M_{^3\mathrm{He}\pi}$ cross section spectra for the $dp \to {}^3\mathrm{He}\pi^+\pi^-$ reaction as in Fig. 8 but only for those events where $M_{\pi^+\pi^-} < 340$ MeV/c^2.

Double-differential cross sections for the ^{3}He $dp \to {}^3\mathrm{He}\pi^+\pi^-$ reaction are shown in Fig. 8 as functions of the three possible invariant-mass combinations, where the acceptance corrections were made on the basis of Eq. (4). However, a model-independent multidimensional approach gave rather similar results.

As known from earlier measurements on the ABC effect, the strong enhancement at small $M_{\pi^+\pi^-}$ and the central peaking of the $M_{^3\mathrm{He}\pi^+}$ distributions appear as the most obvious characteristics of the spectra. The latter is well reproduced by the curves according to Eq. (4), but the ABC peak in the $\pi^+\pi^-$ mass distribution is not quite sharp enough, though this could be adjusted through the introduction of a modest $\pi^+\pi^-$ form factor.

In addition, the difference between the $M_{^3\mathrm{He}\pi}$ spectra could be deduced with high precision. It shows that there must be some $I_{\pi\pi} = 1$ production that interferes with the dominant $I_{\pi\pi} = 0$ of the ABC enhancement.

In the approach proposed here, the isospin factors of 3 and 1 in Eq. (4) ensure that the $\Delta(1232)$ plays a more important role in the $M_{^3\mathrm{He}\pi^+}$ distribution than in that of the $M_{^3\mathrm{He}\pi^-}$, with the latter being mainly a kinematic reflection of the $\Delta^{++}(1232)$ in the available phase space. If this is true, it would mean that a very different picture would emerge if the experiment were repeated at a significantly lower or higher energy, where the kinematic reflections would be changed. At lower energy, for example, one would expect the $M_{^3\mathrm{He}\pi^-}$ distribution to peak at lower masses than for $M_{^3\mathrm{He}\pi^+}$ because of the more restricted phase space.

If the two-pion invariant mass is restricted to $M_{\pi^+\pi^-} < 340$ MeV/c^2, the charge difference becomes more pronounced than that predicted by the model, as can be seen from Fig. 9. There is hence a noticeable isovector part even close to the $\pi^+\pi^-$ threshold. The effects seem much larger than anything resulting from isospin violation and call for a renewed effort to clarify the production mechanism in this reaction.

2.5 Charge Symmetry Breaking in $dd \to {}^4\mathrm{He}\pi^0$

Symmetries and symmetry breaking patterns in the non-perturbative regime of QCD is a key issue of the physics program of WASA-at-COSY. One objective is the determination of higher partial wave contributions to the charge symmetry breaking amplitude in the reaction $dd \to {}^4\mathrm{He}\pi^0$ at an excess energy of $Q = 60$ MeV. Charge symmetry is a subgroup of isospin symmetry being broken by the different masses of the up and down quarks as well as by electromagnetic interaction. In order to get access to quark mass effects on the hadronic level it is favorable to look at charge symmetry breaking (CSB) observables as the relative pion mass difference, which is of electromagnetic origin, does not contribute. The reaction $dd \to {}^4\mathrm{He}\pi^0$ is forbidden by charge symmetry and, thus, a measure of the CSB amplitude. While the reaction has been measured close to threshold at IUCF resulting in an energy dependence of the total cross section compatible with s-wave, data sensitive to higher partial waves were missing. Such data are, however, crucial for calculations within the framework of Chiral Perturbation Theory currently under way.

In a first step the focus was on an exclusive measurement of the reaction $dd \to {}^3\mathrm{He}n\pi^0$. The goal was to provide data for studying the dd initial state interaction at small angular momenta, which is one missing information in the microscopic description of the charge symme-

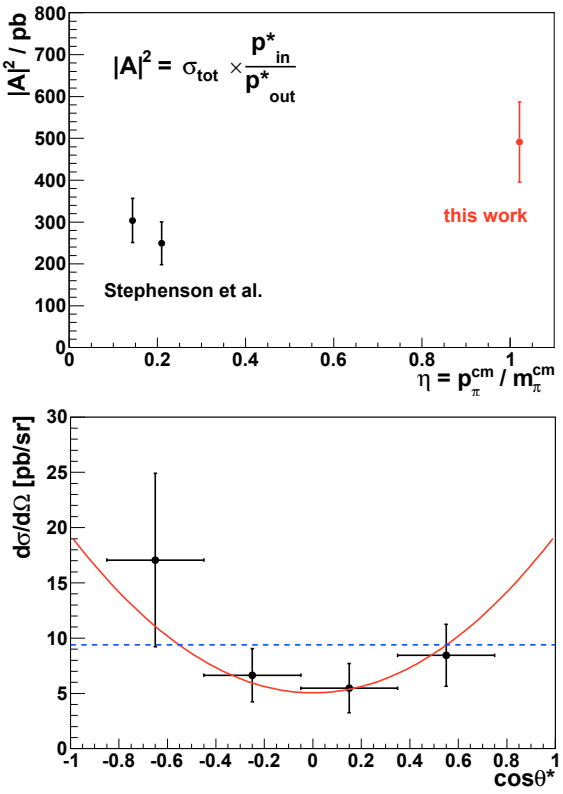

Fig. 10: Top: Energy dependence of the reaction amplitude squared $|A|^2$. In the absence of initial and final state interaction a constant amplitude would indicate that only s-wave is contributing. Bottom: differential cross section. The blue dashed line represents an isotropic distribution, the solid red curve shows the fit with the Legendre polynomials P_0 and P_2.

try breaking reaction. In addition, this channel is used for absolute normalization for the reaction $dd \to {}^4\mathrm{He}\pi^0$. The data set amounts to about 3.4×10^6 fully reconstructed and background-free events. A total cross section of $\sigma_{tot} = (2.89 \pm 0.01_{stat} \pm 0.06_{sys} \pm 0.29_{norm})\,\mu$b has been extracted. Differential distributions have been compared to the incoherent sum of a quasi-free reaction model and a partial-wave expansion limited to at most one p-wave in the final state. The contribution of the quasi-free processes accounts for about 1.1 μb of the total cross section matching the prediction of the quasi-free reaction model. The partial wave decomposition reveals the importance of p-wave contributions in the final state.

While the previous measurements of $dd \to {}^4\mathrm{He}\pi^0$ close to reaction threshold were limited to the total cross section, in order to extract constraints on higher partial waves additional information on the differential cross section are essential. For this, an exclusive measurement detecting the ^{4}He ejectile as well as the two decay photons of the π^0 has been carried out. Separation between ^{3}He and ^{4}He has been done by means of a kinematic fit testing the final-state hypotheses ${}^3\mathrm{He}n\gamma\gamma$ and ${}^4\mathrm{He}\gamma\gamma$ requiring overall energy and momentum conservation. No constraint for the π^0 has been included in order not to introduce a fake π^0 signal. Thereby, the number of ^{3}He ejectiles falsely identified as ^{4}He has been reduced by about four orders of magnitude. The final missing mass plot contains about 100 signal events. For the acceptance correction an isotropic angular distribution has been assumed, for absolute normalization the reaction $dd \to {}^3\mathrm{He}n\pi^0$ has been used. A total cross section of $\sigma_{\mathrm{tot}} = (118 \pm 18_{\mathrm{stat}} \pm 13_{\mathrm{sys}} \pm 8_{\mathrm{ext}})$ pb has been extracted. This result can be compared with the values measured close to threshold by dividing out phase space (see Fig. 10 top). A constant value could be interpreted as a dominating s-wave, but one has to keep in mind that the energy dependence of the formation of a ^{4}He in the $4N$ final state might have some influence here, too. Figure 10 (bottom) shows the differential cross section. Due to the identical particles in the initial state, odd and even partial waves do not interfere and the angular distribution is symmetric with respect to $\cos\theta^* = 0$. As the p-wave and s-d interference terms contribute to the quadratic term and the p-wave also adds to the constant term, the different partial waves cannot be directly disentangled. However, a fit including the Legendre polynomials $P_0(\cos\theta^*)$ and $P_2(\cos\theta^*)$ — although not excluding — does not show any evidence for contributions of higher partial waves:

$$\frac{\mathrm{d}\sigma}{\mathrm{d}\Omega} = (9.8 \pm 2.6)\,\mathrm{pb/sr} \cdot P_0(\cos\theta^*) + (9.5 \pm 7.4)\,\mathrm{pb/sr} \cdot P_2(\cos\theta^*).$$

Based on these results a new measurement aiming at higher statistics and using a modified detector setup has been performed in 2014: a 1.5 m time-of-flight path in forward direction improves the ^{3}He-^{4}He separation and the kinetic energy reconstruction.

For further details see Phys. Rev. C **88** (2013) 014004, and Phys. Lett. B **739** (2014) 44-49.

2.6 Dependence of the Λ Angular Distribution on the Λ Momentum in the Reaction pp → pK$^+$Λ

Former COSY-TOF measurements show that the $l = 2$ Legendre Polynomial coefficient, which is a measure for higher partial waves, rises with increasing beam momentum [Eur. Phys. J. **A**46 (2010) 27]. High statistics data, which are available now, allow for the first time to extract the Legendre coefficients not only from the integrated angular distribution but from a series of angular distributions, each constructed for a bounded range of the center of mass momentum. This dependence of the coefficients on the momentum provides a new comparison and optimization tool for future partial wave analyses.

The data, which were measured with a beam momentum of 2.95 GeV/c in 2010 and 2012, comprises more than 170.000 reconstructed pK$^+$Λ events. The magnitude of the Λ center of mass momentum - distributed between 0 and 0.51 GeV/c - is divided into 6 intervals. For each segment the Λ angular distribution is fitted according to

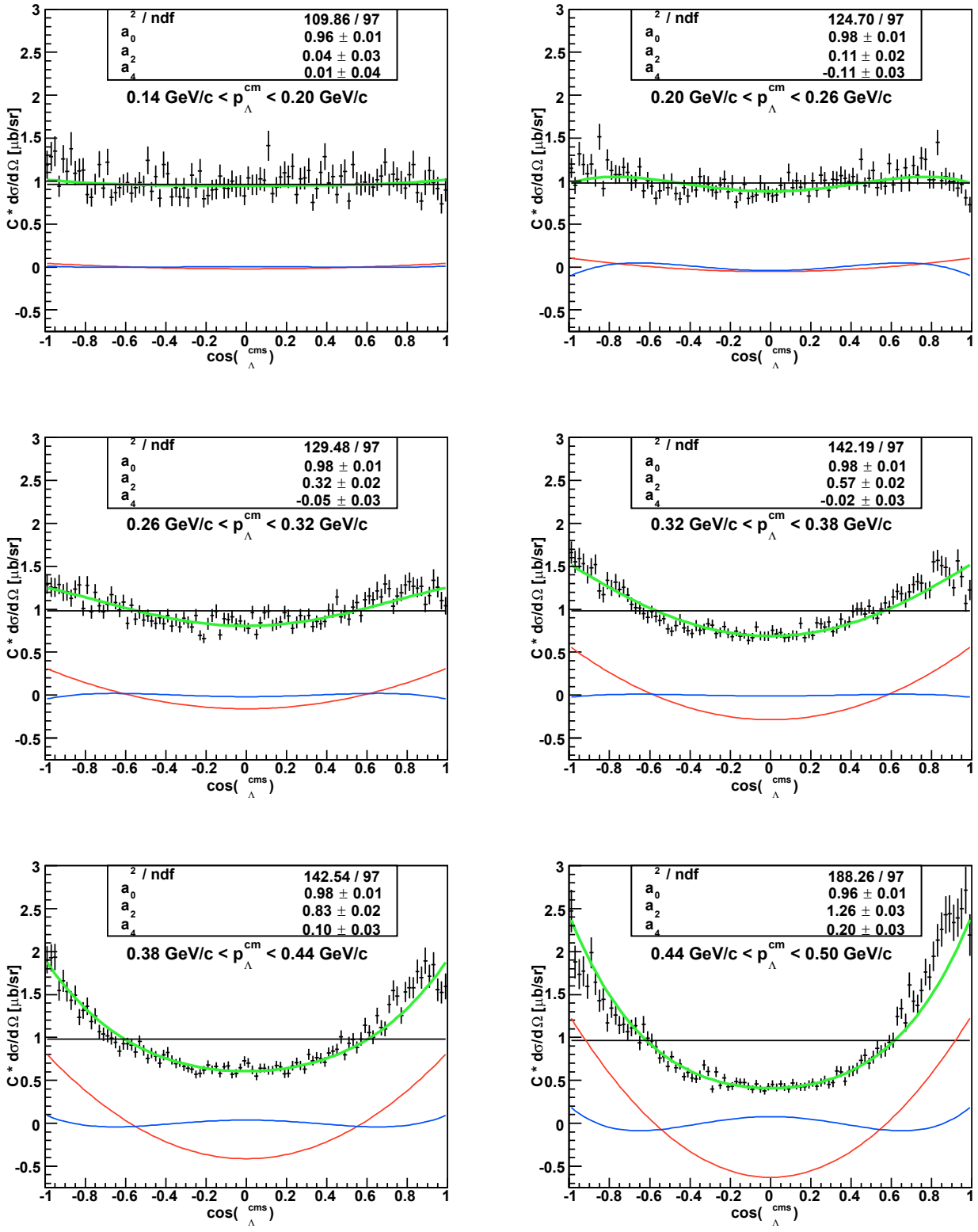

Fig. 11: Λ angular distributions for different ranges of the Λ center of mass momentum. The green curve shows the fit result. The contributions of the Legendre Polynomials P_0, P_2, and P_4, weighted with the corresponding coefficient are plotted in black, red, and blue.

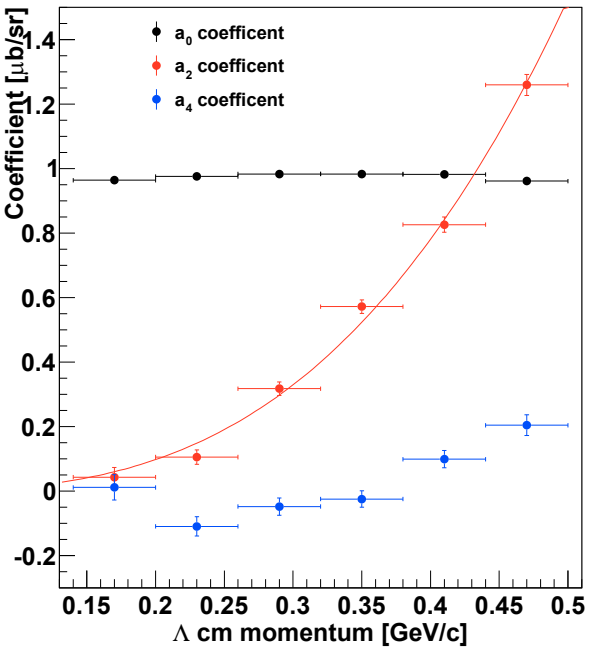

Fig. 12: The dependence of the fit coefficients on the Λ center of mass momentum of the P_0, P_2, and P_4 Legendre Polynomials are shown with the black, red, and blue points. The distribution of the coefficient a_2 is fit with $c \cdot x^3$ (continuous red line).

the formula

$$\frac{d\sigma}{d\cos\vartheta^{\rm cm}} = C \cdot (a_0 P_0 + a_2 P_2(\cos\vartheta^{\rm cm}) + a_4 P_4(\cos\vartheta^{\rm cm}))$$

C is a normalization constant. This formula describes the differential cross section directly as a sum of Legendre polynomials by neglecting the interference terms. Due to identical particles in the initial state, the angular distributions in the center of mass system have to be symmetric about $\cos(\vartheta^{\rm cm})$=0. Therefore the coefficients a_1 and a_3 are set to zero. With this parameterization the coefficient a_2 contains products of SD, PP, and DD partial wave amplitudes, and a_4 contains only the DD partial wave product. The angular distributions are normalized for each range of the center of mass momentum separately in order to be independent of the variation of the cross section with the center of mass momentum.

The angular distributions are shown in Fig. 11 together with the Legendre polynomials P_0, P_2, and P_4 weighted with the corresponding fit coefficients.

The variation of the coefficients a_0, a_2, and a_4 with the Λ center of mass momentum are shown in Fig. 12.

The coefficient a_2 rises by the power of three with the momentum, while the coefficient a_4 is close to 0. A two parameter fit shows in comparison that only for the highest momentum range the reduced χ^2 of the fit is improved, when the term $a_4 P_4$ is included in the formula.

2.7 η decays with WASA-at-COSY

The $\eta \to 3\pi$ decays proceed via strong isospin violation with the matrix element proportional to the light quark mass difference $m_d - m_u$. There are many recent measurements studying $\eta \to 3\pi^0$, but there is only one large statistics measurement — performed by the KLOE collaboration — for the decay $\eta \to \pi^+\pi^-\pi^0$. These data show a deviation compared to the Chiral Perturbation Theory calculations. While dispersive calculations can be used to set precise boundaries on the light quark mass ratios, they have to be accompanied with further experimental input, which is now available from WASA-at-COSY.

The results given below are based on $1.2 \cdot 10^5$ $\eta \to \pi^+\pi^-\pi^0$ events in the final data sample, where the η meson has been produced in the reaction $pd \to {}^3{\rm He}\eta$ at 1 GeV beam energy. All particles were detected in the experiment and overall kinematic constraints were used to improve the resolution. Figure 13 shows the final ^{3}He missing mass distribution.

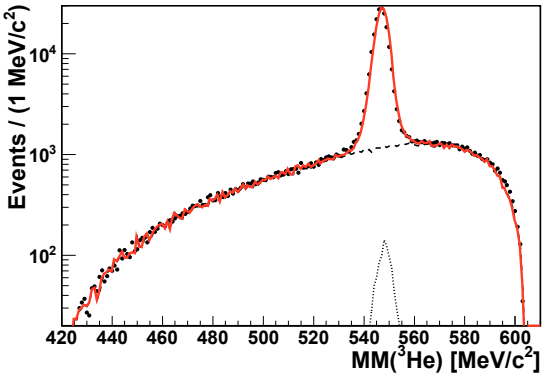

Fig. 13: The ^{3}He missing mass distribution for the final data sample (dots) agrees well with the simulated distributions for signal and backgrounds (red solid). Also shown: simulated background from $\eta \to \pi^+\pi^-\gamma$ (dotted) and 3π production (dashed).

The data could be presented using Dalitz plot where the event yields are obtained using bin-wise background subtraction and are corrected for the acceptance. The differential density of the Dalitz plot can be parameterized:

$$|\mathcal{A}(X,Y)|^2 = N\left(1 + aY + bY^2 + dX^2 + fY^3\right),$$

where X and Y are the Dalitz plot variables and a, b, d, f are the parameters to be determined. The final fit, including statistical and systematical uncertainties, yields

$$\begin{aligned} -a &= 1.144 \pm 0.018(stat) \\ b &= 0.219 \pm 0.019(stat) \pm 0.047(syst) \\ d &= 0.086 \pm 0.018(stat) \pm 0.015(syst) \\ f &= 0.115 \pm 0.037(stat). \end{aligned}$$

These results are based on the first part of the WASA-at-COSY data from the $pd \to {}^3{\rm He}\eta$ reaction. More

data are available from WASA-at-COSY also from the $pd \to pp\eta$ reaction. Together with expected results from other experiments the goal of a precise determination of the $\eta \to \pi^+\pi^-\pi^0$ Dalitz plot parameters might soon be reached.
The presented data have been published in Phys.Rev. C **90** (2014) 4, 045207.

2.8 Determination of the η'-Proton Scattering Length in Free Space

The high mass resolution of the COSY-11 detector combined with the low-emittance proton beam of the cooler synchrotron COSY allowed a determination of the excitation function of the reaction $pp \to pp\eta'$ down to an excess energy of Q = 0.76 MeV, with a precision ΔQ of 0.1 MeV. The by more than a factor of 5 with respect to previous measurements improved resolution enabled a quantitative extraction of the η'-proton scattering length in free space. In the COSY-11 experiment the η' meson was

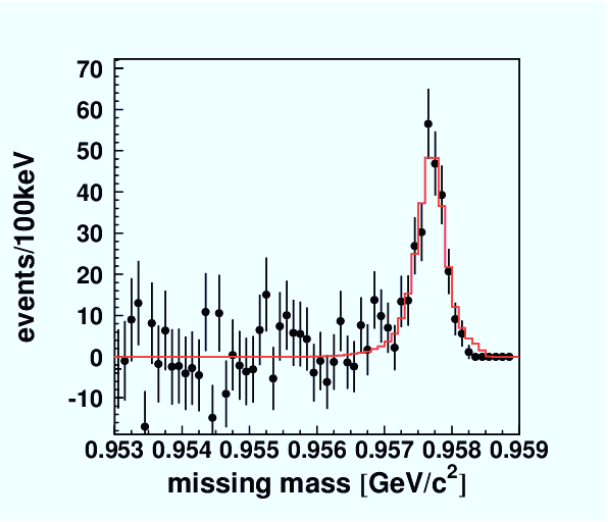

Fig. 14: Missing mass spectrum from experimental data (dots) and simulations (histogram, normalized to the data) for a beam momentum of 3210.7 MeV/c corresponding to a Q-value of 0.76 MeV.

produced in collisions of the COSY proton beam with an internal hydrogen cluster target. The four-momenta of outgoing protons from the $pp \to ppX$ reaction were measured in two drift chambers and scintillator detectors and the η' meson was identified via the missing mass technique. The measurement was performed at five excess energies in the range of Q = 0.76 to Q = 4.78 MeV. The determination of the absolute value of Q was based on the position of the η' signal in the missing mass spectra. Q was determined with a precision of 0.10 MeV, where 0.06 MeV is due to the uncertainty of the η' meson mass and 0.04 MeV comes from the possible misalignment of the relative setting of the detection system components and the center of the region of the beam and target overlap. The latter was monitored by the measurement of elastically scattered protons. In order to reduce the the spread of excess energy to a negligible level a rectangular target stream with a dimension of 0.9 mm x 9 mm at the proton beam position was prepared by a suitable collimator resulting in an excess energy spread of 0.02 MeV. A typical missing mass spectrum for experimental data and Monte Carlo (MC) simulations is shown in Fig. 14.
The excitation function is shown in Fig. 15 from which the η'-proton scattering length has been extracted.

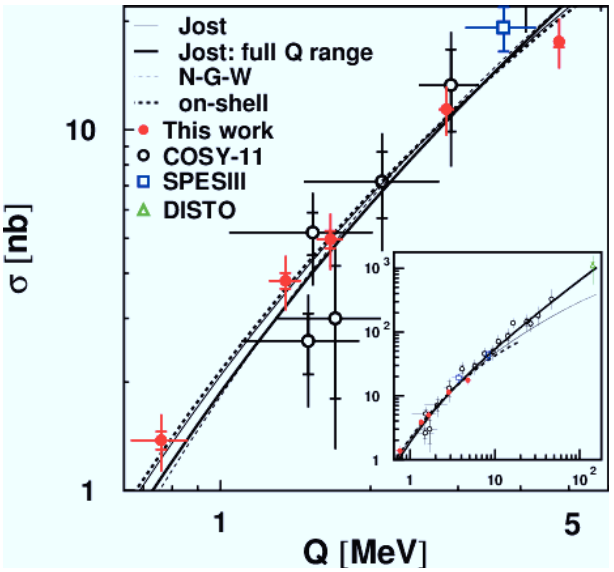

Fig. 15: Total cross sections for the $pp \to pp\eta'$ reaction as a function of the excess energy. Solid circles represent the new results from COSY-11 and results from previous experiments are shown with symbols, as indicated in the legend. The statistical and systematic errors are separated by dashes. The superimposed curves show fit results with the η'-proton scattering length as a free parameter and parametrizing of the pp-FSI enhancement factor by calculating pp-scattering with optical potential including Coulomb (thick dashed line), the inverse of the squared Jost function (thin solid line), and the Niskanen-Goldberger-Watson model (thin dashed line). The insert shows the excitation function up to Q = 180 MeV.

The experimental excitation function was compared to the results of calculations taking into account proton-proton and η'-p interactions, where the real and imaginary parts of the η'-p scattering length were varied as free parameters. At threshold, the distance probed by the $pp \to pp\eta'$ reaction is determined by the momentum transfer between colliding nucleons and equal to about 0.2 fm, whereas the typical range of the strong nucleon-nucleon or meson-nucleon interaction is of the order of a few Fermi. In addition, the energy range considered here is 2 orders of magnitude smaller than

the four-momentum transfer (1 GeV) governing the production amplitude. Therefore, the calculations were carried out using a Watson-Migdal approximation and the complete transition matrix element of the reaction was factorized as $|M_{pp\to pp\eta'}|^2 \approx |M_0|^2 |M_{FSI}|^2$ with the total short range production $|M_0|^2$ and the final state interaction enhancement factor $|M_{FSI}|^2$ which was approximated assuming a factorization into two-particle scattering amplitudes: $M_{FSI} = M_{pp}\ M_{p_1\eta'}\ M_{p_2\eta'}$. For the proton-proton enhancement factor the inverse of the squared Jost function was used and to estimate the model dependence of the result, two other extreme solutions for the proton-proton enhancement factor were considered, the Niskanen-Goldberger-Watson parametrization and the square of the on-shell amplitude of the proton-proton scattering calculated in the frame of the optical potential, with phase shift including strong and Coulomb interactions.
The best fit to the experimental data corresponds to:
$\mathrm{Re}(a_{p\eta'}) = 0.00 \pm 0.43_{stat}$ fm (systematic error negligible)
$\mathrm{Im}(a_{p\eta'}) = 0.37^{+0.02_{stat}+0.38_{syst}}_{-0.11_{stat}-0.05_{syst}}$ fm.
As seen from Fig. 15 the result is independent of the proton-proton FSI model used in the fit.

2.9 Machine developments for spin-filtering experiments at COSY

An intense beam of polarized antiprotons will open new experimental opportunities to investigate the structure of the nucleon [see PAX Collaboration Technical Proposal at http://www.fz-juelich.de/ikp/pax]. The only experimentally proven method to polarise in-situ a stored beam is the spin-filtering. It exploits the spin-dependence of the strong interaction using a polarized internal target. The first spin-filtering experiment was performed by the FILTEX group at the TSR ring in Heidelberg in 1992. In 2012, the PAX Collaboration performed a new experiment at the COSY-ring that provided an additional measurement to the existing one and confirmed the validity of the filtering-method to polarize a stored beam. Figure 16 shows the spin-dependent cross-section measured at COSY together with the other existing measurement performed by the FILTEX collaboration. The solid line represents the theoretical prediction from the nucleon-nucleon interaction. The good agreement between experiment and theory confirms that spin-filtering of a stored proton beam is well-described taking into account only the contributions from proton-proton scattering [Phys. Lett. B 718 , 64 (2012)].
In a polarisation buildup experiment, different parameters have to be optimised. First of all, the kinetic energy of the beam has to be wisely chosen; secondly, the beam lifetime has to be made as long as possible in presence of a polarized gas target with high density and polarization. To achieve this last requirement, extended beam studies have been performed at the COSY ring that have been recently published in a extensive paper [Phys. Rev. ST Accel. Beams 18, 020101 (2015)]. Some of the results are briefly summarised in the following paragraphs.

Fig. 16: Measured spin-dependent polarizing cross section for the interaction (only statistical errors are shown). The solid line represents the prediction from the SAID database

- **Betatron tune mapping.** To increase the beam lifetime, a search for the optimal betatron tunes was performed for several machine settings. In this procedure, called *tune-mapping*, the currents in the quadrupole magnet families of the COSY arcs were varied in the $\pm$ 3 % range, while monitoring the beam-lifetime. The betatron tune scans showed a large variation in the beam lifetime by a factor 6 in a small range of betatron tunes (see Fig. 17). Maximum beam lifetimes were observed close to a working point of Q_x = 3.58 and Q_y = 3.62.

Fig. 17: Beam lifetime as a function of the working point (Q_x, Q_y). The beam lifetime increases with decreasing tune difference $\Delta Q = Q_x - Q_y$. The exact condition ΔQ = 0 (dashed line) could not be reached because of coupling.

- **Orbit correction.** Misalignment or field errors in the magnets, cause the real orbit in a machine to deviate from the ideal one. In regions where the β-functions are large, these deviations lead to local restrictions of the machine aperture, and reduce the lifetime of the beam. A closed orbit correction scheme, based on the *Orbit Response Matrix*

(ORM), was implemented to increase the machine acceptance and to improve the beam lifetime.

- **Commissioning of a low-β section at the PAX interaction point.** The use of a narrow storage cell of diameter d = 9.6 mm and length l = 400 mm to increase the target areal density, would have significantly restricted the machine acceptance for the standard COSY lattice. Assuming single Coulomb scattering as the dominating particle loss mechanism, this would have been directly accompanied by a reduction of the beam lifetime. To obtain small-β functions and thereby overcome the acceptance limitation at the target, a low-β insertion consisting of four additional quadrupole magnets was installed in the drift space in front and behind the target. The β-functions at the position of the PAX quadrupoles have been measured by changing the quadrupole strength by Δk and measuring the corresponding tune change ΔQ of the machine:

$$\bar{\beta}_{x,y} = \frac{4\pi}{l} \mid \frac{\Delta Q_{x,y}}{\Delta k} \mid . \tag{5}$$

The measured $\bar{\beta}_x$ and $\bar{\beta}_y$ agree well with the lattice model calculation and allowed to estimate the β-functions at the center of the target to β_x = 0.31 m and β_y = 0.46 m (see Fig. 18). Consequently, the implemented low-β section avoids a restriction of the machine acceptance.

- **Space charge studies.** The impact of space-charge effects on particle loss can be investigated by studying the effect of the beam emittance on the beam lifetime. The mechanism can qualitatively explained from the repulsion between the charged particles in the beam causing a betatron amplitude-dependent incoherent tune shift for a non-uniform charge distribution. This effect was counteracted by reducing the cooling performance of the electron cooler by tilting its beam with respect to the proton beam. The increased beam emittance reduces the so-called *tune.spread*, the associated area in the tune diagram shrinks, fewer betatron resonances are excited, and the observed beam lifetime increases. The investigations showed an increase of the beam lifetime from 6300 s to 9200 s by increasing the four-dimensional beam emittance $\varepsilon = \varepsilon_x \varepsilon_y$ from about 0.2 to 1.3 mm^2 mrad^2.

Fig. 18: Model calculation of the β-functions at the PAX-TP and measured values of β_x and β_y at the magnet positions. In blue the four new PAX quadrupole magnets are indicated. Magnet 1 and 4 form the defocusing (D) pair (PAX1), while magnets 2 and 3 the focusing (F) pair (PAX2). Each pair is operated with a single power supply. In addition the storage cell and the beam direction are shown.

3 COSY – Accelerator Developments

3.1 First beam cooling with the 2 MeV electron cooler at COSY

3.1.1 Introduction

The 2 MeV electron cooler at COSY is the first device utilizing the idea of magnetized cooling in this energy range, being an important step towards relativistic electron cooling required for the HESR at FAIR. The new system enables electron cooling in the whole energy range of COSY. The construction of the 2 MeV cooler began at the Budker Institute of Nuclear Physics (BINP) in 2009 and ended 2012. In spring 2013 the cooler was installed in the COSY ring. First beam cooling results were obtained in October 2013 by the joint BINP-COSY team. Further beam cooling experiments followed during a two-week period of dedicated beam time beginning of 2014. At that time the first attempt to use electron and stochastic cooling in the same machine cycle was made. In addition, electron cooling of proton/deuteron beam into a barrier bucket was demonstrated. Further experimental electron cooling studies were carried out in November 2014. So far electron cooling of proton beam up to 1670 MeV kinetic energy was demonstrated. The maximum electron beam energy achieved amounted to 1.25 MeV. A voltage up to 1.6 MV was demonstrated. The cooler was operated with an electron current up to 0.9 A.

3.1.2 The 2 MeV electron cooler

Due to a very wide energy range of 0.025-2 MeV the electron beam is guided by a longitudinal magnetic field all the way from the electron gun to the collector. The electrostatic accelerator consists of 33 individual sections of identical design. The electrical power to each section is provided by a cascade transformer. To satisfy the requirement on the straightness of magnetic field of the order of 10^{-5} in the cooling section, the main solenoid is made of numerous short coils. The individual coils can be adjusted mechanically in two degrees of freedom.

An in-vacuum system for measuring the straightness of magnetic field based on a magnetic mirror reflecting laser beam is permanently installed in the cooling section.

Energy range	0.025 – 2 MeV
HV stability	$< 10^{-4}$
Electron current	up to 3 A
Electron beam diameter	10 – 30 mm
Length of cooling section	2.7 m
Toroid radius	1 m
Magnetic field	0.5 – 2 kG
Vacuum	$10^{-9} - 10^{-10}$ mbar

Table 1: Parameters of the 2 MeV electron cooler.

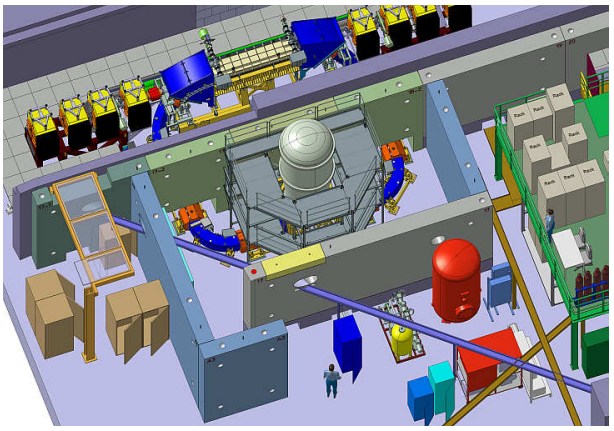

Fig. 19: A 3D drawing showing the 2 MeV electron cooler installed in the COSY ring. The electrostatic accelerator is shown surrounded by the radiation shielding. The concrete elements on top of the cooler bunker are not shown.

3.1.3 Electron cooling at 200 MeV

At this energy the magnetic field in the cooling section was set to 480 G. Figure 20 shows the result of transverse cooling of a dc proton beam using 200 mA electron beam at 109 keV. The number of protons in the ring was intentionally lowered to 10^8 in this particular machine cycle to exclude intensity effects and to minimize the particle loss rate. The Ionization Profile Monitor (IPM) was used to acquire beam profile data in real time.

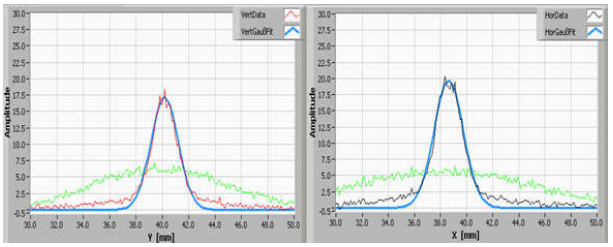

Fig. 20: Horizontal and vertical profiles of the electron cooled proton beam. Profiles of an uncooled beam are shown in green, cooled beam profiles in black and red, the corresponding Gaussian fits in blue. Widths of cooled beam $\sigma_h = 1.2$ mm and $\sigma_v = 1.15$ mm were measured.

In another machine cycle much higher beam intensity was injected. Figures 21 and 22 show transverse and longitudinal cooling in the same machine cycle. The cycle duration was set to 514 s. At t = 30 s in the cycle (flat top) the electron current was ramped up to 200 mA causing the beam to shrink transversally and longitudinally. At this energy cooling was also accompanied by significant beam losses.

In the middle of the machine cycle about $4 \cdot 10^9$ particles remained in the ring. After the e-beam was turned off at t = 350 s, the proton beam size as well as the width of the longitudinal spectra increased again due to intra-beam

Fig. 21: Evolution of horizontal and vertical beam width and beam current. The 200 mA electron beam was turned on at t = 30 s and turned off at t = 350 s.

scattering. In contrast to the initial cooling the beam can be cooled again (not shown in Figs. 21 and 22) without losses. A standard COSY beam position monitor was used to measure the Schottky spectra

Fig. 22: Evolution of the longitudinal Schottky spectra. The 200 mA electron beam was turned on at t = 30 s and turned off at t = 350 s. The upper plot shows the spectra of the uncooled (red) and cooled (blue) beam and a spectrum after the e-current was turned off (orange). Black lines represent the corresponding time markers in the spectrogram (lower plot). Time scale in minutes is shown on the left edge of the spectrogram.

Figure 23 shows the effect of electron cooling of bunched beam on bunch length. After finishing acceleration the RF amplitude was reduced to about 100 V. Cooling with 200 mA resulted in an equilibrium bunch length of 27 ns.

Fig. 23: Proton bunch shortening during electron cooling with 200 mA. Shown are the bunch shapes for the cooled and uncooled proton beam as reported by the bunch phase monitor.

3.1.4 Electron cooling at 1670 MeV

At 1670 MeV the magnetic field in the cooling section was set to 1.3 kG.

Fig. 24: Evolution of the beam width and proton beam current during electron cooling with 320 mA.

In addition to Fig. 24 showing the effect of electron cooling on transverse beam size, the effect of precooling using the stochastic cooling system is shown in Fig. 25.

Fig. 25: Evolution of the beam width and beam current during transverse stochastic (first half of the machine cycle) and electron cooling with 320 mA (second half).

Horizontal and vertical stochastic cooling was active in

the first half of the machine cycle leading to a significant reduction of the transverse beam size without significant beam loss. The longitudinal behavior of the beam in the same machine cycle is shown in Fig. 26. One can see that the beam becomes wider due to the absence of longitudinal cooling in the beginning. Fast cooling of the beam core and somewhat slower cooling of the tails of the distribution has been observed after electron cooling was turned on at t = 2 min.

Fig. 26: Longitudinal electron cooling of proton beam at 1670 MeV. A pickup of the stochastic cooling system was used to measure the Schottky spectra. Only a part of the machine cycle is shown. Transverse stochastic cooling was active until t = 2 min, after that electron cooling was turned on. In the upper plot the red curve corresponds to the longitudinally uncooled beam while the blue one shows the spectrum of the cooled beam.

Figure 27 shows the reduction of bunch length as a result of electron cooling. A bunch length of about 8 ns was demonstrated.

Fig. 27: Electron cooling of bunched proton beam at 1670 MeV. Shown are the bunch shapes for the cooled and uncooled proton beam as reported by the bunch phase monitor.

3.1.5 Summary

The 2 MeV electron cooler is being put into operation at COSY. A first series of experiments were carried out by the joint BINP-COSY team. Electron cooling of a proton beam up to 1670 MeV corresponding to 908 keV electron energy was demonstrated. The maximum electron beam energy achieved so far was 1.25 MeV. A high voltage up to 1.6 MV was obtained. Cooling of a deuteron beam at low energy was successful. Cooling into a barrier bucket as well as simultaneous electron and stochastic cooling was successfully demonstrated. The first impression is that the overall cooling time becomes shorter; the two systems however, need to be carefully matched. The emphasis of the recent experiments was put on the cooler hardware. The interaction of the cooler with the machine, in particular the cooling rates will be studied in detail during the upcoming dedicated beam time in March 2015. The data obtained so far suggests a more favorable scaling of the longitudinal cooling time with energy as compared to the $\beta^4\gamma^5$ scaling. At low energy a significant beam loss was observed during the cooling process, similar to the losses typically observed using the 100 kV cooler. At higher energies the losses are much less pronounced. The loss mechanism has to be investigated in more detail. The recently developed software includes an automated correction of uncompensated transverse kicks, the electron beam experiences when passing the bent sections of the transport line. This is the first step towards a model based operation of the cooler.

4 Storage Ring Based EDM Search – Achievements and Goals

4.1 Introduction

Permanent Electric Dipole Moments (EDM) of fundamental particles violate both time invariance T and parity P. Assuming the CPT theorem this implies CP violation. The Standard Model (SM) predicts non-vanishing EDMs, their magnitudes, however, are expected to be unobservably small with current experimental techniques. The discovery of a non-zero EDM would be a signal for new physics and could explain the matter-antimatter asymmetry observed in our Universe. Different approaches to measure EDMs of charged particles are pursued at Brookhaven National Laboratory (BNL) and Forschungszentrum Jülich with an ultimate goal to reach a sensitivity of 10^{-29} e·cm in a dedicated storage ring. The Jülich-based JEDI Collaboration has been formed to exploit and demonstrate the feasibility of such a measurement and to perform the necessary R&D work towards the design of a dedicated storage ring. As a first step R&D work at COSY is pursued. Subsequently, an EDM measurement of a charged particle will be performed at COSY with limited sensitivity, and, on a longer time scale, the design and construction of a dedicated storage ring will be carried out.

The measurement of an EDM in a storage ring is based on the following principle: the spin is precessing in the horizontal plane governed by the magnetic dipole moment (MDM). If an EDM exists, the spin vector will experience an additional torque resulting in a change of the original spin direction that creates a vertical spin component. The vertical spin component, proportional to the size of the EDM, will be measured by scattering the stored beam at an internal target and analyzing the azimuthal distribution of the scattered particles. A coherent buildup of the vertical polarization only takes place within the time the spins of the particle ensemble stays aligned. Since the spin tune is a function of the betatron and synchrotron amplitudes of the particles in the six-dimensional phase space, spin decoherence is caused by beam emittance and momentum spread of the beam and leads to a gradual decrease of the polarization buildup rate in the vertical direction. To reach the anticipated statistical sensitivity of 10^{-29} e·cm a Spin Coherence Time (SCT) of 1000 s has to be reached. The mean challenge of such kind of experiment is a very small expected vertical component of the spin excited by the EDM and the relatively large contribution by false spin rotations due the field and misalignments errors of accelerator elements.

4.2 Experimental Results at COSY

For the measurements and the results discussed below a common experimental setup at the Cooler Synchrotron COSY has been used. A polarized deuteron beam with an intensity of $\approx 10^9$ particles was accumulated, electron-cooled to reduce the equilibrium beam emittance, and accelerated to the final momentum of 970 MeV/c. The beam polarization, perpendicular to the ring plane, was alternated from cycle to cycle using two vector-polarized states and an unpolarized one. An rf cavity was used to bunch the beam during the full cycle, while after the beam was prepared the electron cooler was turned off for the remaining measurement period. An rf solenoid induced spin resonance was employed to rotate the spin by 90° from the initially vertical direction into the horizontal plane. Subsequently, the beam was slowly extracted onto a carbon target using a white noise electric field applied to a stripline unit. Elastically scattered deuterons were detected in the scintillation detectors of the EDDA polarimeter consisting of rings and bars around the beam pipe and forming four quadrants up, down, right, and left. The corresponding rate asymmetries are used to analyze the polarization states of the beam throughout the cycle.

4.2.1 Spin Tune Measurement and its Applications

The spin tune ν_s is defined as the number of spin revolutions relative to the momentum vector per particle revolution around the invariant spin axis. In an ideal planar magnetic ring $\nu_s = \gamma \cdot G$ with γ being the Lorentz factor and G the magnetic anomaly. Aiming at a high sensitivity of EDM searches using storage rings, one of the limiting factor is the control of the spin motion in the presence of small fluctuations of electric and magnetic fields. Thus, a precise determination of the spin tune as a function of time in the accelerator cycle is one important tool for the R&D activities at COSY towards a first precursor experiment and the design of a dedicated ring.

In order to determine the spin tune, asymmetries are formed using the time-dependent counts of the up (U) and down (D) detector quadrants of EDDA. As the high precession frequency of $\gamma \cdot G \cdot f_{\mathrm{rev}} \approx 120$ kHz makes it impossible to use detector rate asymmetries accumulated over time intervals in the order of seconds, a sophisticated read-out system has been developed, which can time stamp the individual event arrival times with respect to the beginning of each cycle. This was achieved by using one long-range time-to-digital converter (TDC) in a dedicated continuous mode, which is also recording the frequency of the COSY rf cavity with the same reference clock. This information was then used to unambiguously assign the number of orbit revolutions n since the start of the cycle to each recorded event. Further details on the experimental setup can be found in Phys. Rev. STAB **17** 052803 (2014).

It is not possible to determine the spin tune ν_s from the observed event rates $R_{\mathrm{U,D}}(t)$ directly by a simple fit, because at a detector rate of $\approx 5\,\mathrm{s}^{-1}$ only about one event is detected per 24 spin revolutions. Instead, the analysis uses a pre-assumed, fixed spin tune ν_s^0 to calculated for each event the spin phase advance $\varphi_s = 2\pi\nu_s^0 n$. In the further analysis, the information from both detector quadrants are combined such, that the spin precession is reflected in a harmonic oscillation around zero. Finally,

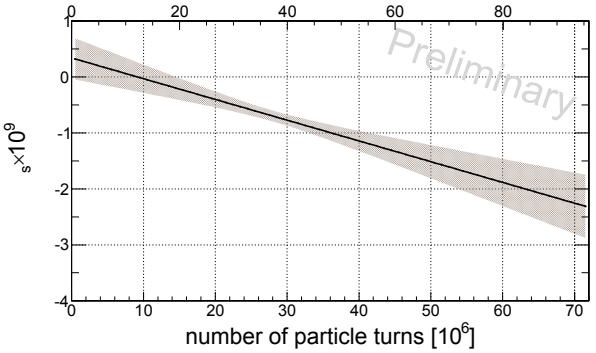

Fig. 28: Deviation $\Delta\nu_s$ of the spin tune from the value of $\nu_s^{fix} = -0.160975407$ as a function of turn number in the cycle. The grey band includes statistical errors only.

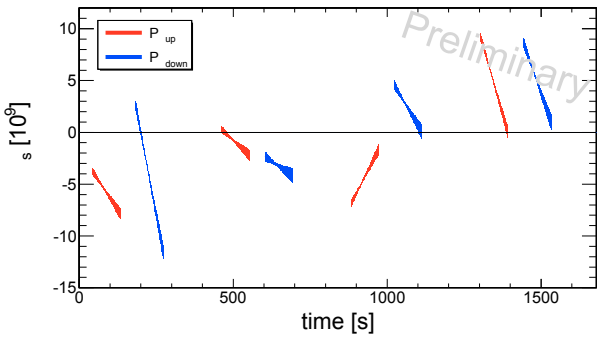

Fig. 29: Walk of the spin tune during eight consecutive cycles with alternating initial vector polarization. The third cycle is depicted in Fig. 28 as well. Cycles with unpolarized beam that followed the down state (blue) are not shown.

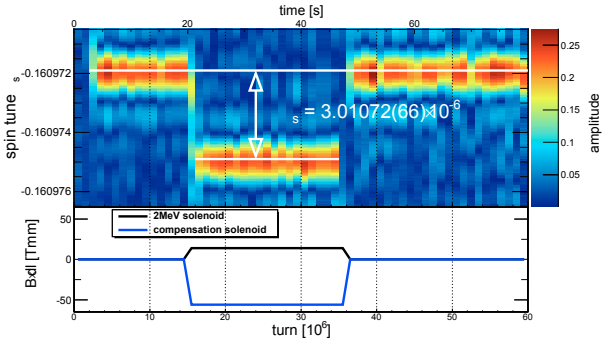

Fig. 30: Measurement of the spin tune jump (top) caused by the artificial imperfections originating from the additional solenoid fields (bottom) as described in the text. An enlarged version of this figure is shown on the front cover of this annual report.

the signals are mapped into a phase interval of 2π for fitting. This is done separately for intervals of $\Delta n = 10^6$ corresponding to 2.6 s. In a next step, a range of spin tunes are tested around the nominal value of $\nu_s = \gamma \cdot G$ and the one yielding the largest asymmetry in the fit is used as a first estimate with an uncertainty of $\Delta\nu_s \approx 10^{-6}$. The precision can be further improved to about 10^{-10} by analyzing the phase advance of the fit throughout the cycle. As an example, the deviation of the spin tune from the assumed one is shown in Fig. 28 as function of time in the cycle. A publication with a more detailed description of this method in currently under preparation.

As a first application this method can be used to monitor the stability of the spin tune in the accelerator for longer time periods. Figure 29 shows the observed spin tune changes from cycle to cycle, which are of about the same order (10^{-8} to 10^{-9}) as those within a single cycle. This is remarkable because COSY was never intended to provide a level of stability below $\approx 10^{-6}$ with respect to magnetic fields, orbit corrections, and stabilization of power supplies. Investigations are presently underway to understand the observed variations and to study possible means to stabilize them even further, *e.g.* by the development of a feedback system to COSY.

As discussed above the spin motion in a storage ring is perturbed by spin kicks from the imperfection fields in the ring. This leads to a tilt of the invariant spin axis with respect to the vertical axis of a perfect ring. One measurement followed the idea to probe the in-plane imperfections by adding well-known artificial imperfections and to observe the effects on the spin tune. As artificial imperfections the solenoids of the old and the new electron cooler have been used. These have been switched on during the measurement period for certain time resulting in a jump of the measured spin tune. This is depicted in Fig. 30: the magnetic field of the solenoids are given in the lower panel while the effect on the spin tune is plotted above. After switching off the solenoids the spin tune restores to its original values. A two-dimensional scan varying both fields independently can be used to determine the direction of invariant spin axis in the ring (see corresponding article in Appendix K).

4.2.2 Spin Coherence Time

One requirement for the EDM storage ring experiment is that the polarization be maintained in the direction of the beam velocity for times as long as 1000 s. The polarization in this direction is generally unstable. The spin directions of individual particles precess at rates given by the particle momentum, a quantity that is sensitive to differences in path length around the storage ring and oscillations along the beam direction. These differences may be reduced by electron-cooling the beam and gathering the beam into a bunch, which guarantees that all particles have the same average ring revolution time. Additional corrections may be added to compensate for second-order effects arising from path length differences. The best way to do this requires adding sextupole fields in the arcs of the storage ring.

There are three main families of sextupole magnets located in COSY. They differ in their sensitivities to various beam properties. The MXS family is located where the

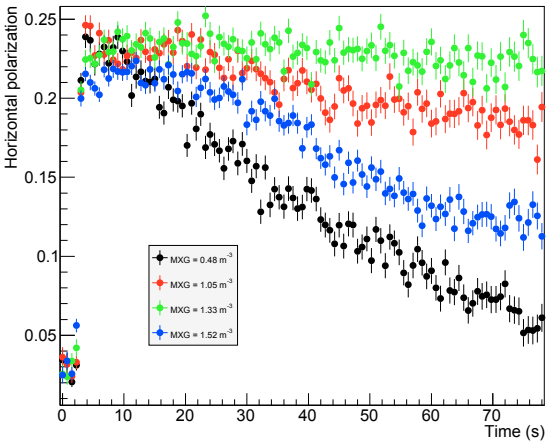

Fig. 31: Measurements of the horizontal polarization, including reductions due to the polarized source and the polarimeter, as a function of time during the storage of the beam. The four curves represent four different settings of the MXG sextupole field. The polarization is best preserved when the field is 1.33 /m^{-3}.

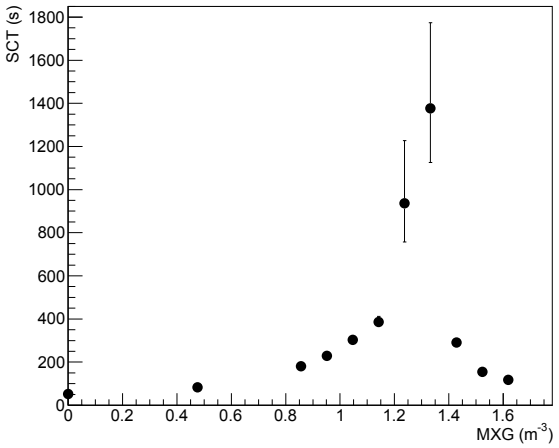

Fig. 32: Measurements of the exponential horizontal polarization lifetime for a series of MXG sextupole settings. The values go through a maximum for sextupole values near 1.3 /m^{-3}. The best values exceed 1000 s.

beam is horizontally wide. Likewise, the MXL family is located where it is tall. A third family, MXG, samples a region where the beam is spread out horizontally according to the momentum of the particles in the beam. In each case, the particular sextupole family associated with each beam feature is located in a place where it can correct the contributiion to depolarization from that feature, which covers horizontal, vertical, and longitudinal oscillations within the beam as it is confined within COSY.

Knowing how to make the right correction requires the measurement of the horizontal polarization, as described above. Figure 31 shows four sets of measurements made at regular intervals while the beam is being stored. For an MXG sextupole setting of 1.33 /m^{-3}, the polarization has the highest rate of survival during the observation time. The comparison can be made more quantitave by assigning a lifetime to each polarization curve. If the data are represented by an exponential decay, then the decay constant may represent this lifetime. A graph of all of the lifetime measurements in the group sampled in Fig. 31 is shown in Fig. 32. Here there is a clear maximum near 1.3 /m^{-3}. The polarization lifetime in this region exceeds 1000 seconds, the requirement for an EDM storage ring experiment at the best projected sensitivity. A more precise sextupole value may be obtained by looking instead at the reciprocal of the lifetime, which varies linearly near the maximum lifetime and thus permits a more precise determination of the location of the best value. A large number of scans such as that shown in Fig. 32 are possible with various combinations of settings for the three main sextupole families. So some scheme is needed to organize this effort.

The sextupole magnets also control another property called chromaticity. This property measures the changes in the rate at which particles oscillate about the center of the beam as their momentum changes. For best storage ring beam lifetime, it is usual to adjust the sextupole fields so that the chromaticity is near zero, which means that the oscillation rates are independent of momentum. In the first studies of the polarization lifetime it appeared that the best results also came when the chromaticity was close to zero. In the final set of experiments, chromaticity and polarization lifetime were measured together.

Figure 33 shows two planes the represent the values of the chromaticity as functions of the value of the magnetic fields associated with the MXG and MXS sextupole familites. The shading of the planes is a guide to where the chromaticities are positive and negative in this perspective drawing. The planes themselves represent the best reproduction of about 15 measurements over a range of MXG and MXS values. The planes are determined with a precision that is a few percent of the largest values shown here. The places where the chromaticity goes to zero represent places where the beam oscillation rates become independent of the particle momentum. These places are desirable operating points since they are usually associated with very long storage times for the circulating beam. The zero values form straight lines, as shown by the dashed lines in the figure. It happens that for the COSY storage ring these lines are almost parallel. Their separation is governed by the third sextupole family, MXL. Figure 33 shows the best overlap, which comes for MXL = -0.2 /m^{-3}. Because long polarization lifetimes appeared to be associated with these places of zero chromaticity, the settings of Fig. 33 were chosen as the starting point for a series of polarization lifetime scans.

The final result is shown in Fig. 34 as a function of the

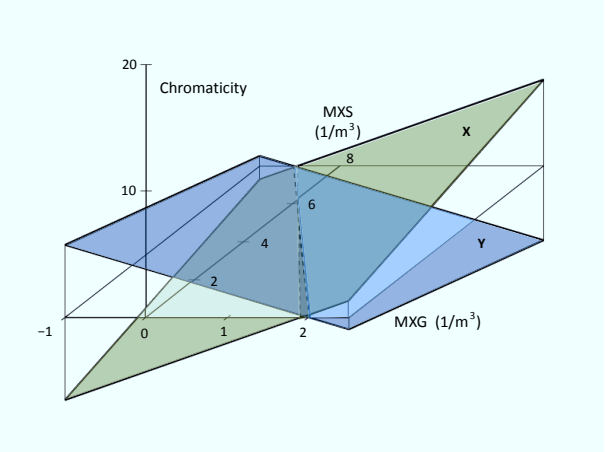

Fig. 33: The two planes in this projection drawing show the values of the X and Y chromaticities as functions of the settings of the fields in the MXG and MXS sextupole families. The shading of the two planes is meant to illustrate where the chromaticity is positive or negative (or visible around the edge of the zero chromaticity plane). Dashed lines show where these planes cross zero chromaticity.

strength of the field in the MXG and MXS sextupole families. The zero chromaticity lines are shown by the two colored bands in the picture. The width of the bands indicates the error in determining each chromaticity. While the two zero chromaticity lines do not perfectly coincide, the difference is not statistically significant, so we may regard these lines as being the same.

In making the polarization scans, it is useful to make different beam setups to emphasize the roles of the different sextupole families. In order to make MXS prominent, we produced a beam that was wide horizontallly by heating it with a white noise electric field. Likewise for MXG, a beam was created in which there were large synchrotron oscillations of the individual beam particles along the beam direction, thus producing momentum variations that would show up as beam displacements near the MXG magnets. The location of the best polarization lifetime is shown for four scans with each type of beam. The best location for the horizontally wide beam is a black dot; the best location for large longitudinal oscillations is a red circle. The errors on these symbols are smaller than the symbol. The points where the polarization lifetime is the largest correlate well with the positions of zero chromaticity. One interpretation of this result is that both long polarization lifetime and zero chromaticity depend on establishing a property in the ring that minimizes how much a change in the particle momentum will produce a change in the path length as a particle goes around the ring.

Without making any effort to mitigate polarization loss, the polarization lifetime is typically tens of milliseconds. The improvements described here together have led to an increase of about 10^5 in this lifetime. This, in concert

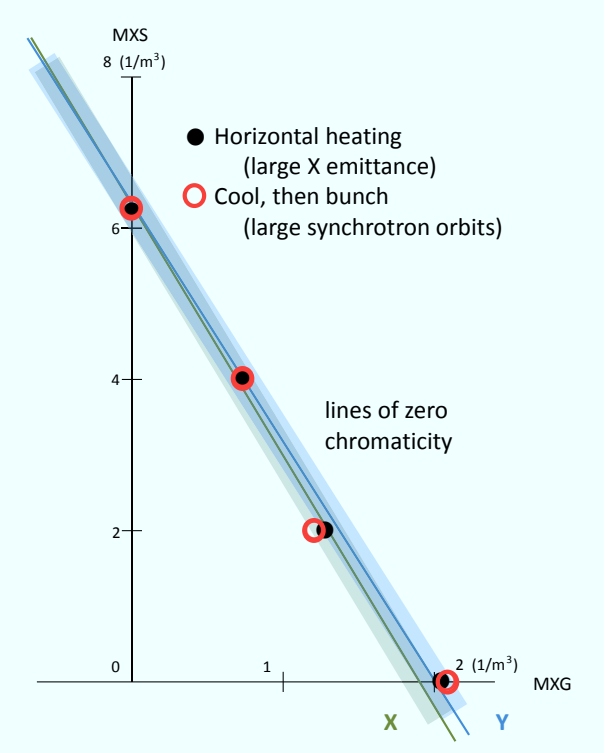

Fig. 34: On the plane of MXS and MXG sextupole values, the two bands indicate the error margin for locating the places where the X or Y chromaticity is zero (with MXL set to -0.2 /m^{-3}). Scans of the polarization lifetime using two different beam setups (horizontally wide and longitudinally extended) gave values where the polarization lifetime went through a maximum, which is shown here by either a black dot or a red ring.

with another study completed earlier demonstrating that polarization changes as small as parts per million may be measured in spite of changing beam geometry or detector sensitivity to rate, means that these issues do not present any obstacle to a storage ring search for an EDM meeting the required sensitivity.

4.3 Technical Developments

A prototype RF Wien filter has been developed and successfully commissioned with lower power to carry out a feasibility test (see Fig. 35). The device was operated at the $f_{rev}\,|\gamma G - 1|$ harmonic of the spin precession frequency at roughly 871 kHz. Similar measurements at the $f_{rev}\,|\gamma G + 1|$ harmonic at 630 kHz are planned. The benefit of lower RF frequency is less damping of the induced oscillation of the vertical polarization component.

By a 90° rotation of the device around the beam axis, this RF E/B dipole in Wien filter mode will modulate the spin tune via the MDM. In conjunction with the fields distributed along the accelerator ring this leads to an EDM induced polarization build-up of the vertical polarization component.

Fig. 35: Photograph of the RF Wien filter as installed in the COSY ring.

A second prototype device based on a strip-line design is also developed together with the High-Frequency Institute of RWTH Aachen University.
For the final EDM ring, high-field electrostatic deflectors have to be developed. Major development steps are the optimization of the shape of electrostatic field plates with suitable magnet coil configurations and R&D work on surface treatments that can yield high electric field gradients. For an All-in-One EDM storage ring with a radius of $r = 30$ m, transverse electric fields of roughly 17 MV/m and magnetic fields up to 1.6 kG are required in combined electrostatic/magnetic field deflectors. Electrostatic deflectors, previously employed as beam separators in the Tevatron, have been transferred from Fermi National Accelerator Laboratory (FNAL) to Jülich to get experience on surface treatment and operation of high voltage electrostatic field plates and finally to refurnish this devices to further increase field gradients towards the requirements for the final ring.

4.4 Beam and Spin Tracking

Full spin-tracking simulation of the entire experiment is absolutely crucial to explore the feasibility of a first direct EDM measurement at COSY and a planned dedicated EDM storage ring. For a detailed study during the storage and buildup of the EDM signal, one needs to track a large sample of particles for billions of turns. Given the complexity of the tasks, particle and spin dynamics simulation programs must be benchmarked and tracking results compared to beam experiments performed at COSY, to ensure the required accuracy of the obtained simulation results. COSY Infinity[Nucl. Inst. and Meth. in Phys. Res. A 558 (2005)] and Mode [Proc. 5th International Particle Accelerator Conference (IPAC 14), Dresden, Germany, 2014, MOPME011, ISBN 978-3-95450-132-8] are utilized for this purpose, both based on map generation using differential algebra and the subsequent calculation of the spin-orbital motion for an arbitrary particle. Integrating programs, solving equations of particle and spin motion in electric and magnetic fields using Runge-Kutta integration, have also been used for benchmarking.
The spin motion in homogenous electromagnetic fields has been investigated in case of a non-vanishing EDM. Furthermore the ability to calculate time-dependent transfer maps, which is necessary to model the influence of RF fields on beam and spin motion for the first direct EDM measurement at COSY, was implemented. Since the particle motion is perturbed by imperfections of the storage ring magnets, the existing misalignment commands for shifts, tilts and rotations can be superimposed to study randomized sets of magnet misalignments. The resulting closed orbits can be corrected by the orbit correction system to suppress false spin rotations via the MDM.

4.5 Outlook

The R&D program will continue with prototyping of critical accelerator elements and tests with polarized beams at COSY. Different methods to perform a first direct EDM measurement at COSY will be further investigated by spin-tracking simulations in order to quantify the systematic limits and finally perform an EDM measurement at COSY. For the design study of a dedicated EDM storage ring, lattice design in conjunction with the design of all accelerator elements will be the major task for the JEDI collaboration in the upcoming years.

5 COSY – Operation Statistics

5.1 Beam Time at COSY

For 2014 in total 6888 hours of operation were scheduled. 3192 hours (46.3%) were scheduled for hadron physics user beam time, 1848 hours (26.8%) were scheduled for dedicated beam dynamic studies, equipment tests for HESR and FAIR related activities, 952 hours (13.8%) for precursor experiments on EDM studies. 896 hours (13%) were used for COSY machine development and experimental set-up. (see Fig. 36.) With a shutdown duration of 615 hours (8.9%) the reliability of COSY amounts to more than 90%.

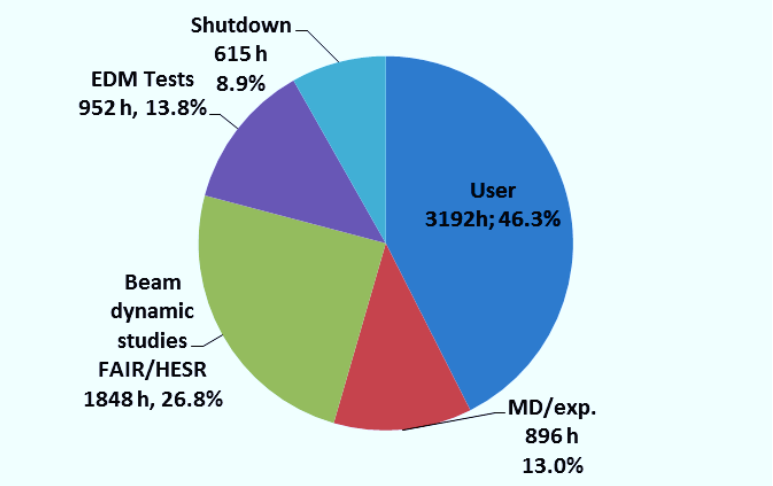

Fig. 36: COSY beam-time statistics in 2014.

6 Progress of the HESR at FAIR

6.1 Project Status

Technical design work of nearly all components of the HESR is finished or in the final stage. Some few items for HESR are purchased by FAIR GmbH. However, the technical supervision is completely covered by our institute. Issues like intermediate storage, pre-assembly, and assembly schedule are coming more into focus.
Sextupole and steerer magnets together with their power converters are a Romanian in-kind contribution to FAIR. Production of the first magnet of each of these kinds started. The power converter design is awaiting acceptance.
Since project start, contracts and orders have been made which already bind 43% of the project costs. 13% of the project cost is spent. Some work packages encountered a delay compared to the original schedule, but all work packages announce that the scheduled start of installation can be confirmed.

6.2 Magnets and Power Converters

For dipole and quadrupole magnets the series production could be released. The first dipole magnet (see Fig. 37) and the first quadrupole magnet (see Fig. 38) already passed their factory acceptance test (FAT) and site acceptance test (SAT), and now serve as reference magnets at the producing company. For powering the reference dipole magnet a dedicated test power converter has been acquired and is operational. The power converter for the reference quadrupole magnet is the first one of the regular series production. For each magnet the reproducibility of the magnetic measurements before and after magnet opening is verified. From the second magnet on (dipole or quadrupole), all magnets will be delivered to Jülich, starting in Q1/2015. There, the dipole magnets will be equipped with their vacuum chamber including heating jackets, the alignment feet will be added, and the relevant

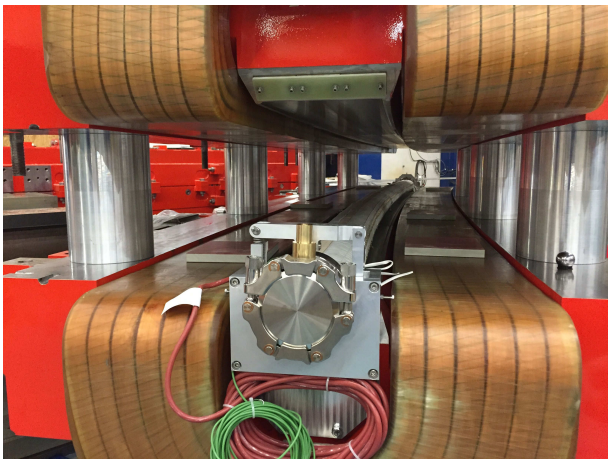

Fig. 37: Opened dipole magnet with vacuum chamber incl. heating jacket.

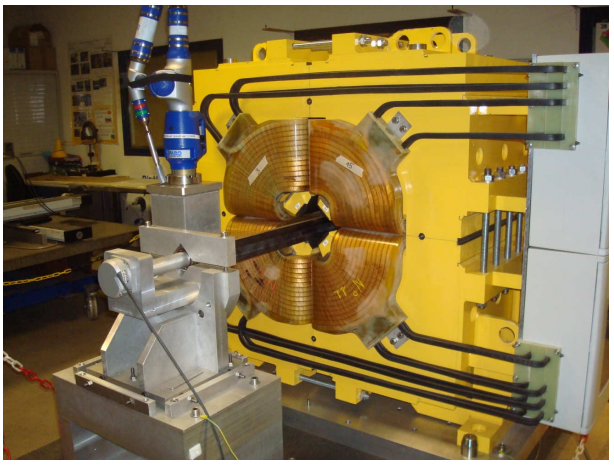

Fig. 38: Quadrupole magnet on measuring bench.

geodetical data will be generated to ease final installation in the tunnel. The quadrupole magnets will be stored after delivery until sextupole and steerer magnets and the beam position monitors will become available. All these items will be integrated into the so-called quadrupole assembly. The complete unit later will be moved into the accelerator building.
Design work for further magnets (injection dipole, injection septum, and PANDA chicane dipoles) is finished. Acquisition is expected in summer 2015.
27 power converters for the quadrupole magnet families have passed the FAT. Presently, they need some modifications as the standard load cable had been changed to coaxial which requires a redesign of the cable inlet. SAT is expected before summer 2015.
The power converter for the injection dipole has been accepted. The ones for the PANDA chicane dipoles are announced to be ready in Q1/2015.
The power converters for the main dipole magnets only can be ordered just in time to be ready when all magnets will have been installed as no suitable test load for commissioning is available.

6.3 Injection and RF Cavities

The HESR has been originally designed for storage and acceleration of up to 10^{11} antiprotons for internal target experiments with high momentum resolution up to nearly $1 \cdot 10^{-5}$ in the momentum range 1.5 GeV/c to 15 GeV/c. The well-established stochastic stacking method is however not applicable. Instead a different method using moving barriers and stochastic filter momentum cooling is established to accumulate 10^{10} antiprotons within 1000 s. Recently, it was proposed to prove the feasibility of operating the HESR storage ring with heavy ion beams with the special emphasis on the experimental program of the SPARC collaboration at FAIR. The magnetic rigidity range from 5 to 50 Tm allows the storage of typical reference ions such as $^{132}Sn^{50+}$ and $^{238}U^{92+}$ in the kinetic energy range 165 MeV/u up to roughly 5 GeV/u. In re-

cent simulation studies a bare $^{238}U^{92+}$ beam with N = 10^8 ions and a kinetic energy 740 MeV/u is kicked injected from the CR into the HESR. To transfer the beam from the CR to the HESR it is essential to provide a gap of 318 ns for the CR's extraction kicker. Therefore, an adiabatic rebunching of the DC-beam is employed. The initial rms-relative momentum spread of $1.5 \cdot 10^{-4}$ in the DC-beam of the CR will increase to $3.3 \cdot 10^{-4}$ (rms) when the beam becomes bunched with an rms-bunch length of 110 ns. A nearly Gaussian shaped ion beam is then kicked injected into the HESR. The horizontal as well as vertical emittance is $\varepsilon_{rms} = 0.125$ mm mrad. The barrier bucket (BB) cavity needed for longitudinal beam manipulation has been developed in Jülich and following the design of the multi-harmonic cavity operational in COSY. The voltage required for HESR operation can (in combination with solid state amplifiers) only be achieved if water cooling is replaced by air cooling. The distribution of the air between the ferrite cores turned out to be critical. After several optimization loops the final test was successful (see Fig. 39), and the cavity design could be finalized. Start of production in the Jülich on-campus workshops is scheduled for autumn/winter 2015.

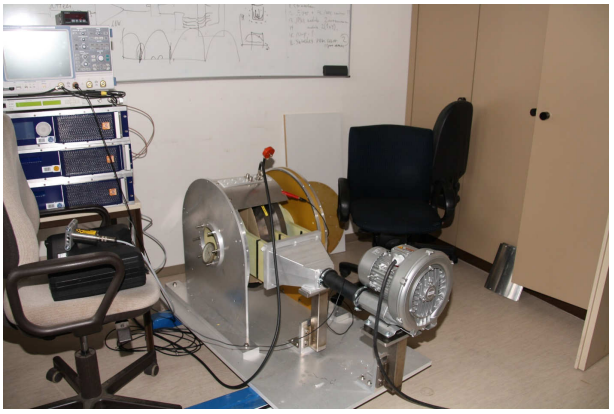

Fig. 39: Test bench for air cooling of RF ferrites. Achieved parameters: temperature rise of 10 C (steady state) at 1.4 MHz, 220 W forward power, 380 V peak voltage.

The hardware for the kicker injection into HESR is built at two locations: the 4 magnets and the current bearing parts are covered by the contract with a company (6.4 mrad total kick angle, 4.5 kA, 50 kV), all the remaining parts including test tank are being provided by Jülich. Design will allow pole reversal as p and pbars will have to be injected into HESR. Vacuum baking will also be possible. Production of the magnets has been released, the design concept for the pulser has been agreed upon, and the test tank is in production in Jülich. Release of the series production is expected in summer 2015. The complete assembly of the test tank is shown in Fig. 40.

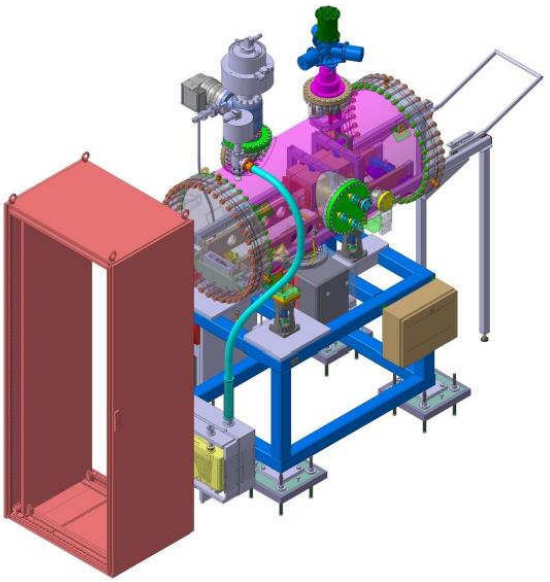

Fig. 40: Test tank for injection kicker magnets.

6.4 Vacuum and Beam Diagnostics

For all HESR the needed stainless steel has been delivered after a tedious acquisition process. Now the straight and bent beam pipes are being produced, Assembly of a bent beam pipe into the dipole magnet was successful and thus the series production of the bent pipe could be released.

The vacuum system between the dipole magnets ('quadrupole assembly') has been detailed. The design includes securing for transportation. The chambers where the vacuum pumps will be attached ('pumping cross') have been put to tender. All accepted competitors for this tender will deliver their prototypes in Feb 2015. For the largest vacuum section a very detailed specification is being worked out to serve as a template for all vacuum sections with respect to instrumentation and control planning.

The work packages 'Injection' and 'Stochastic Cooling' have been supported by designing the associated vacuum chambers. The space management for the complete HESR has been refined taking into account the latest data from all the production companies. These data are basis for planning the 'transport into tunnel' activity. Close collaboration with FAIR and GSI is ensuring seamless integration of all components into the different FAIR wide data bases.

The magnet assembly area in Jülich has been set up. Storage capacities are found to be sufficient for one quarter of the total magnet production. Renting additional storage area close to Darmstadt is planned for autumn 2015.

6.5 Stochastic Cooling and Heavy Ion Operation

The HESR lattice with zero dispersion in the straights has been optimized for the PANDA internal target experiment and stochastic cooling with a transition gamma $\gamma_{tr} = 6.23$. The lattice can however be adjusted for transition gamma values between 6 and 25. A hydrogen target with a density $N_T = 4 \cdot 10^{15}$ cm^{-2} is used for internal target experiments. In the simulations it is assumed that the target is located at zero position and angle dispersion. A transverse emittance growth due to the beam-target interaction is then solely determined by multiple-angle scattering in the target. The simulations reveal that beam cooling alone cannot compensate the strong mean energy loss and energy loss straggling in the case of thick targets. It is essential to utilize the barrier bucket (BB) cavity of the HESR to compensate the strong mean energy loss.

In the HESR newly designed ring slot coupler structures for the (2 - 4) GHz stochastic cooling system come into operation. They have been experimentally tested at COSY and in Dubna.

Transverse and longitudinal stochastic cooling will be provided. Transverse cooling in beam-target experiments is necessary to compensate the emittance increase due to the beam-target interaction. However the major task of cooling assisted by the BB cavity is to compensate the strong mean energy loss and the energy loss straggling caused by the beam-target interaction. To accomplish this goal the filter as well as the Time-Of-Flight (TOF) technique will be applied for momentum cooling. The TOF cooling method is the preferable choice when the frequency spread of the beam at low energies is large and thus would exceed the notch filter cooling acceptance. At higher energies the frequency spread is smaller due to adiabatic damping and a smaller frequency slip factor. Then the filter cooling technique is applicable and provides the fastest momentum cooling.

For an internal target experiment at 740 MeV/u the CR uranium beam bunch is kicked injected into the gap between two movable barriers with the maximum available barrier peak voltage of 2 kV. After injection the barriers are moved and the beam can adiabatically debunch within 500 ms. During debunching the momentum spread in the beam is reduced. It is visible in Fig. 41 that during the first 500 ms the number of ions with a relative momentum spread of $|\Delta p/p| \leq 5 \cdot 10^{-5}$ is increased. After one second stochastic cooling is switched on and the momentum spread is further reduced. The internal target is switched on at t = 3 s. The increasing fraction of particles with a relative momentums spread of $|\Delta p/p| \leq 5 \cdot 10^{-5}$ is due to the ongoing momentum cooling. An equilibrium is reached after 6s. About 70% of the ions have a fractional momentum spread less than $5 \cdot 10^{-5}$.

The studies included the simulation of injection and acceleration of a bare uranium beam to the 4.5 GeV/u. The acceleration time to flat top energy amounts to 50 s since the maximum cavity peak voltage is limited to 2 kV and the highest magnetic field ramp rate is dB/dt = 25 mT/s.

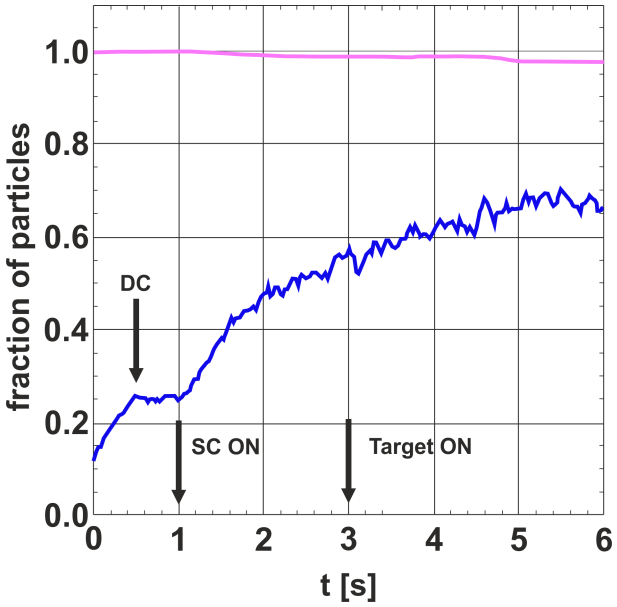

Fig. 41: Fraction of ions with relative momentum spread within $|\Delta p/p| \leq 5 \cdot 10^{-5}$ (blue) and $3 \cdot (\Delta p/p)_{inj}$ at injection (magenta) versus time. At 500 ms (DC) the final barrier position is reached. The beam is now nearly a DC beam. Stochastic TOF cooling is switched ON at t = 1 s (SC ON). The target is inserted at t = 3 s (Target ON).

An intermediate flat top at 3 GeV/u is necessary to avoid transition crossing. After debunching at 3 GeV/u the lattice optics is changed from γ_{tr} = 6.23 to γ_{tr} = 14.6. The beam is then recaptured with the h = 1 cavity and accelerated to the final energy. An internal target experiment with stochastic momentum cooling at 4.5 GeV/u has been studied. The simulations predict that after 10 s an equilibrium relative momentum spread of $5 \cdot 10^{-5}$ should be possible.

The present studies predict that in the modularized start version of FAIR a bare uranium ion beam bunch from the CR can be injected into the HESR. The envisaged design of the cavities and the components of the stochastic cooling system in the HESR permit that the beam can either be prepared with TOF stochastic cooling assisted by the BB cavity for an internal target experiment at 740 MeV/u or it can be accelerated to the maximum available energy of 4.5 GeV/u within 50 s with the maximum available magnetic field ramp rate. Fast stochastic filter momentum cooling can then be applied supported by the BB cavity for an internal experiment with high momentum resolution.

The hardware for stochastic cooling is in production: The vacuum tanks are being produced by a company. The other parts have been purchased and are being assembled in Jülich. Final assembly of the first tank in a clean room is scheduled for Q2/2015.

7 The $\overline{\text{P}}$ANDA Experiment at FAIR

7.1 Introduction

The future Facility for Antiproton and Ion Research (FAIR) will be one of the largest accelerator facilities in the world giving access to a large variety of different experiments to gain new insights into the structure of matter and the evolution of the universe.

The antiProton Annihilation at Darmstadt ($\overline{\text{P}}$ANDA) experiment is one of the main experiments of FAIR. It utilizes the intense anti-proton beam with excellent momentum resolution provided by the High Energy Storage Ring (HESR) to perform precision measurements in the charmonium energy regime to improve the understanding of Quantum Chromo Dynamics.

In this regime many new and unexpected hidden and open charm states were found in the last decade where the nature of many of theses states is not clear. First proof was found that at least some of theses states could be exotic particles with more than three valence quarks. To distinguish the various theories about the origin of theses states a precise knowledge of the mass and the width of theses states is important. Here $\overline{\text{P}}$ANDA is the only experiment in the world which will be able to determine the width of these states down to 50 keV, compared to an upper limit of a few 1 MeV now.

An intense simulation program is ongoing to develop the needed algorithms and to determine the performance of $\overline{\text{P}}$ANDA once the experiment is running. One example for this are the simulations of the D_{sJ} mesons formed by a heavy c quark and a light s quark.

The signatures of the physics channels $\overline{\text{P}}$ANDA is interested in is very similar to the structure of the background reactions. Therefore, $\overline{\text{P}}$ANDA is not able to select the physically interesting reactions based on a few, fast subdetectors but has to read out the complete dataset of the whole detector. To reduce the huge amount of raw data coming from the detector by a factor of 1000 to a manageable data rate of 200 MByte/s for permanent storage, and detailed analysis, a novel event filter technique is used. This approach sets stringent requirements both on the readout electronics inside the detector and on the online computing capabilities of $\overline{\text{P}}$ANDA to analyze the incoming data stream in real time. To cope with these requirements new front-end electronics have to be developed and new processing architectures like GPUs are under study.

Important for the measurement of open charm states is a powerful background suppression which requires the identification of secondary vertices from D-meson decays with a $c\tau$ $O(100\,\mu m)$. This can only be done by a modern tracking system for charged particles with a Micro Vertex Detector (MVD) in combination with a large volume gaseous detector like a Straw Tube Track (STT). Both systems are under development in Jülich together with other groups inside the $\overline{\text{P}}$ANDA collaboration.

7.2 $D_{sJ}^{(*)}$ meson reconstruction at $\overline{\text{P}}$ANDA

The so-called D_{sJ} mesons are particles formed by a heavy quark c and a light anti-quark $\bar{s}$ (and c.c.); they represent a family of charged particles, with different values of the angular momentum J ($J = 0$, 1, 2 or 3). A system of light-heavy quarks is expected to be treated in a non-reativistic way inside the potential model; therefore, the mass of these states should be very precisely predicted. However, the measurement of the mass of the states $D_{s0}^{*}(2317)^{+}$ and $D_{s1}(2460)^{+}$ does not fit theoretical expectations.
The $\overline{\text{P}}$ANDA experiment at FAIR (Facility for Antiproton and Ion Research) in Darmstadt (Germany) will be able to achieve a quantitatively and qualitatively higher mass resolution than at the B-factories, which is expected to be decisive to measure the width of the $D_{s0}^{*}(2317)^{+}$ and $D_{s1}(2460)^{+}$.
Several theoretical interpretations have been proposed for the new resonant states like hadro-charmonia, hybrids, glueballs, etc. Some of those involves the measurement of the width of these exotic structures, unknown until now. The upper limit is about a few MeV, which is from 10 up to 100 times higher than the predicted width values. High quality calculations as well as measurements are compulsory to decide among the various scenarios for each state.
In $\overline{\text{P}}$ANDA D_s mesons are reconstructed with a reconstruction efficiency $\sim$30%; however, with a preselection requiring p_γ >50 MeV/c and p_{track} > 100 MeV/c, and a dedicated selection involving kinematic variables, the efficiency lowers to $\sim$17% (see Fig. 42). This improves the signal over background ratio (S:B) from 1:10^6 to 1:30. With this selection we expect to collect in between 1500 and 15000 D_{sJ} per day, in the hypothesis that $\overline{\text{P}}$ANDA will run in high resolution mode, e.g. $\mathcal{L}$ = 0.86 pb^{-1}/day. This assumes that the cross section will be in between 10 and 100 nb. Our yield estimation must be scaled by the Branching Fraction (BF) of the D_{sJ} decay mode under study. The reason why we obtain so high rate is that we work on inclusive reconstruction of the D_s recoil, that also allows to obtain higher mass resolution compared to the exclusive reconstruction of the $D_{sJ}^{(*)}$.
The reaction under study will be $p\bar{p} \to D_s^- D_{sJ}^{(*)+}$, with $D_s^- \to K^+K^-\pi^-$. For these analyses, the beam momentum is >8.8 GeV/c. Here we report a study performed with the Monte-Carlo simulation framework of $\overline{\text{P}}$ANDA PandaRoot to reconstruct the mass of the $D_{s0}^{*}(2317)^{+}$, where the signal and background distributions are compared.
The study of the $D_{s0}^{*}(2317)^{+}$, $D_{s1}(2460)^{+}$ and $D_{s1}^{\prime}(2536)^{+}$ is interesting for several reasons:
1. excitation function of the cross section calculation, to extract the measurement of the width (Γ);
2. cross section evaluation;
3. chiral symmetry breaking;
4. mixing of D_{sJ} states with same spin and parity;
5. study of the invariant mass system of $D_s D_{sJ}^{*}$ and search for 4-quark states with *strange* content in the

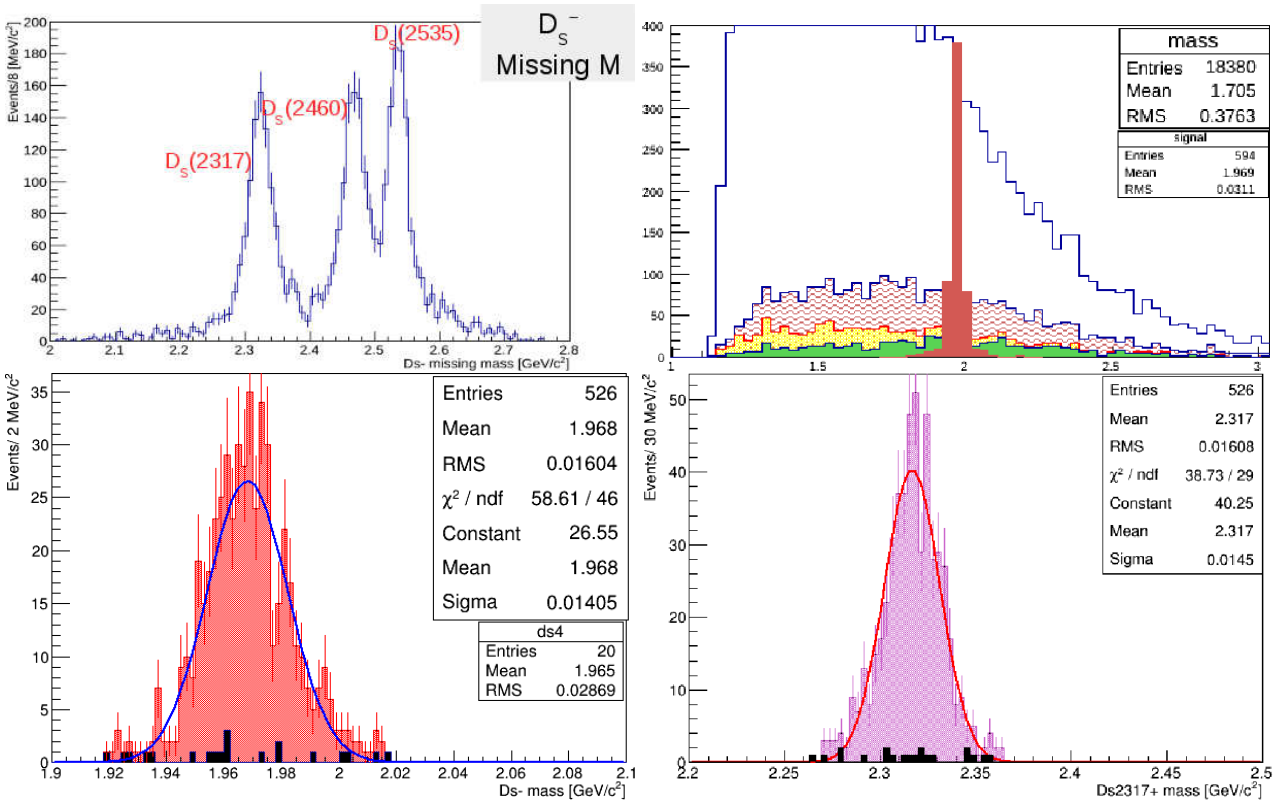

Fig. 42: (left top) Reconstructed mass values of several D_{sJ}, in an inclusive analysis of the channel $\bar{p}p \to D_s^- D_{sJ}^{(*)+}$, as indicated. (right top) Study of the background contribution to $\bar{p}p \to D_s^- D_{s0}^*(2317)^+$, where different colors refer to different sets of selection cuts. (left down) D_s^- reconstruction after a dedicated selection: signal (red) and an arbitrary background sample distribution (black) are compared. (right down) $D_{s0}^*(2317)^+$ mass (violet area), in comparison with the background (black area), after a dedicated selection.

Charmonium field.

Width and mass values of the resonant states will be extracted as parameters of the fit to the excitation function of the cross section. A scan of the invariant mass of the D_{sJ} decay is planned in 100 keV/c^2 steps for this purpose. We plan in the future to complete the simulation and extract mass and width of the $D_{sJ}^{(*)}$ as parameters of the fit.

7.3 Simulated Measurement of the Ds Semileptonic Decay Form Factor

The semileptonic D_s decays are governed by both weak and strong interactions. The strong interaction dynamics can be described by a single form factor $f_+(q^2)$, where q^2 is the invariant mass of the lepton-neutrino system.

In order to evaluate the detector performance in measuring the D_s semileptonic decay form factor of $D_s^+ \to e^+\nu_e\eta$, we simulate the following decay channels with 10,000 events at $\sqrt{s} = 4.108$ GeV: $\bar{p}p \to D_s^+ D_s^-$; $D_s^- \to K^+K^-\pi^-$; $D_s^+ \to e^+\nu_e\eta$; $\eta \to \pi^+\pi^-\pi^0$; $\pi^0 \to \gamma\gamma$. This simulation is done by using the GEANT4 transport code for the particle tracking through the complete $\overline{\text{P}}$ANDA detector. With the present software, the decay chain is reconstructed with an efficiency of $\varepsilon(D_s^-) = 17\%$ and $\varepsilon(\eta) = 11\%$. Table 2 summarizes the preliminary results of the reconstruction resolutions for D_s^- and η.

Table 2: Resolutions of reconstructed D_s^- and η candidates.

	σ_{mass}	σ_{vtx} [μm]			σ_{mom} [%]	
	[GeV/c^2]	x	y	z	p_t	p_z
D_s^-	0.0155	67	68	150	3.0	1.4
η	0.0084	287	296	909	2.2	1.7

After reconstructing the intermediate particles D_s^- and η, the kinematics of the undetected neutrino can be calculated based on a four-momentum condition. The maximum $M^2(e^+\nu_e)$ is consistent with the physical limitation $q^2 \leq (M_{D_s} - M_\eta)^2 \approx 2.02$ GeV$^2/c^4$. Figure 43 shows the results of the lepton-neutrino system. The reconstruction efficiency is $\varepsilon(e^+\nu_e) = 2\%$.

Assuming the cross section on the production of a D_s pair is 20 nb with a beam momentum of 8.0 GeV/c, we estimate the production rate to be approximately 90 events per month for a luminosity of 2×10^{32} cm^{-2}s^{-1}. The upcoming steps will include a modification of the present software to improve the reconstruction efficiency and an investigation of the background channels.

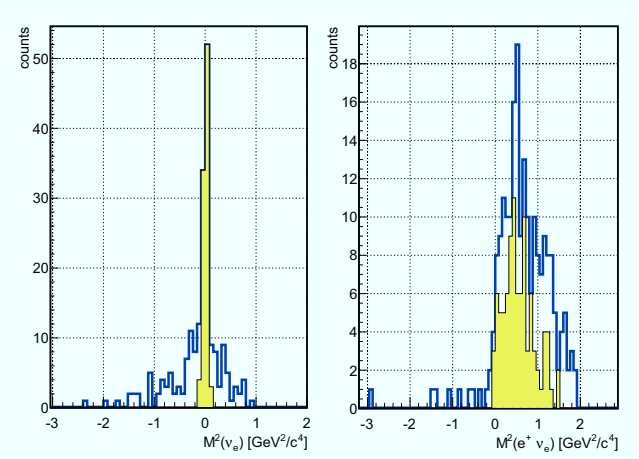

Fig. 43: Left: mass squared of ν_e candidates. Right: invariant mass squared of lepton-neutrino system. The blue line shows the distributions of all candidates; the yellow filed indicates a mass window selection on ν_e, i.e. $\left|M^2_{\nu_e}\right| < 0.1\ \mathrm{GeV}^2/c^4$.

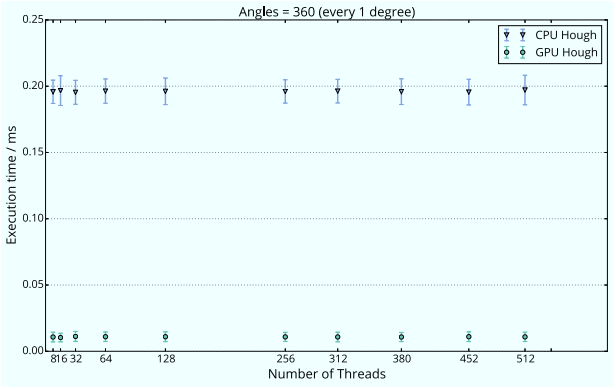

Fig. 44: Computation time of the Circle Hough algorithm when the circle center coordinates are computed on the GPU (green points), compared to a computation on the CPU (purple triangles). The GPU was a NVIDIA GTX 580, the CPU was an Intel Core i5 (3.3 GHz). On the x axis, the number of threads used for the GPU code is shown.

7.4 GPU Online Tracking Algorithms

As background and signal events at $\overline{\mathrm{P}}$ANDA's investigated energy regime have similar signatures, a hardware-level trigger is not foreseen for the experiment. Instead, a fast software trigger takes over this task. The raw data stream of the detector of 200 GB/s (at 2×10^7 event/s) has to be reduced by three orders of magnitude to match the available storage space for further, in-depth offline analysis. A step in the reduction process of the software trigger is online track reconstruction: Discrete detector hits are used to reconstruct the trajectory of the particle creating the hits. The trajectory, or *track*, can then be used to deduce the particle properties and make a triggering decision.

We evaluate the feasibility of using GPUs, Graphics Processing Units, for online tracking. GPUs offer high-performance computing capabilities at a low price budget if the GPU's ability of parallel data processing can be exploited. Currently, we investigate three different categories of parallel tracking algorithms: The Riemann Track Finder, using Riemann surfaces for track reconstruction of highly-parallel seeded track candidates; the Triplet Finder, an extensively GPU-optimized first-stage algorithm capable of track reconstruction without event time information; different Hough Transforms, which create multitudes of possible tracks per hit in order to find the most probable track by comparisons across all created tracks in a set of hits.

One of the Hough Transforms currently investigated is a transformation involving the direct generation of sets of circles. The algorithm, dubbed Circle Hough, neglects multiple scattering and assumes that a circle is in a first approximation a description of a particles' track. The algorithm is designed to detect *primary particles*, particles originating from the interaction point and going through the currently processes hit point (x_i, y_i). A circle can mathematically always be formulated by means of three points. With the interaction point $(0,0)$ being one, (x_i, y_i) another point, the Circle Hough samples through all possible circle center points, creating valid circles going through $(0,0)$ an (x_i, y_i). According to the equation

$$(x_C, y_C)_{ij} = (x_i + s_{ij}\cos\varphi_j, y_i + s_{ij}\sin\varphi_j) \tag{6}$$

$$s_{ij} = \frac{\rho_i^2 - x_i^2 - y_i^2}{x_i\cos\varphi_j + y_i\sin\varphi_j + \rho_i} \tag{7}$$

the circle centers are computed. φ_j is the the sampled angle, $\varphi_j \in [0°, 360°]$, ρ_i the isochrone drift radius of a STT hit (0 if the hit is not a STT hit). Different hit points originating from the same track share the same values of the circle center. When filling the coordinates of the generated center coordinates, (x_C, y_C) into a histogram, the bin with the highest multiplicity holds the coordinates of the circle best describing a tracking going through the hit points. The algorithm is currently investigated in terms of its reconstruction quality, the different parameters tuned to match simulated data with good agreement. At the same time, the algorithm is ported to a version running on a GPU. The core, the generation of the circle center points (x_C, y_C), is offloaded to the device and invoked by an interface with $\overline{\mathrm{P}}$ANDA's simulation framework PandaRoot. The first implementation of the GPU code provides parallelism with respect to the computed circle centers: Per hit, all circle centers are computed at the same time. A speed-up, compared to the CPU version, of 20× can be reached for the computations, see Fig. 44. The x axis of this plot shows the dependence of the computation time on the number of threads with which the GPU is called. Further performance optimization, especially by increasing the amount of parallelly run data, are possible and part of our research.

$\overline{\mathrm{P}}$ANDA's ambitious computational goals require a broad

variety of hardware at different stages of the data acquisition chain. This, in turn, requires communication protocols able to trasmit data with high performance (transmission rates, latency, consistency) and a strong degree of flexibility. In a Message Queue (MQ) environment, both data and control packages (messages) are exchanged asynchronously between senders and receivers through a control structure (queue) making for an inherently flexible, easily scalable architecture. FairMQ is the implementation of MQ within the FairRoot environment, offering an abstract high-level interface which is independent from the low-level transport libraries. To explore the possibilities of using FairMQ in association with a GPU-based implementation of a tracking algorithm, we developed a standalone, proof-of-concept system. Hit data is parsed from an input file, transmitted using FairMQ, and processed using CPU or GPU implementations of the Circle Hough algorithm. First performance tests with no data processing or computational overload show that, for optimal values of the message size, the FairMQ transmission rate is limited by the underlying interface (5 GB/s between two TCP/IP sockets over PCI Express).

7.5 Test Beam Measurements of the new ToPix4 MVD Pixel Readout ASIC

The $\overline{\text{P}}$ANDA experiment will deal with very high interaction rates up to 2×10^7 interactions/s. Since the MVD is the innermost detector it has to handle a high flux of particles. In the "hottest" areas if the MVD a pixel front end module has to handle an average particle rate of up to 2.9×10^6 counts/s for a full size front end. For a peak rate even more than 4×10^6 counts/s can be assumed. Due to the readout concept of $\overline{\text{P}}$ANDA the full data stream of the MVD has to be read out, which is a novel and challenging feature for this kind of detector. To test the rate capability of the recent ToPix prototype (ToPix 4) a dedicated testbeam was performed at the COSY accelerator. The ToPix 4 is a reduced size prototype with 640 pixels arranged in four double-columns. The final ASIC will have 12,760 pixels arranged in 55 double-columns with 116 pixel per column.

The last testbeam at the COSY accelerator was done 2012 with the ToPix 3 prototype read out with the Torino readout system and the Jülich Digital Readout System (JDRS). This year the same setups were deployed. The JDRS setup was enlarged compared to 2012 in hardware in software to handle four ToPix 4 prototypes instead of one in a beam-telescope setup (see Fig. 45). The testbeam was done with a proton beam with p_{Beam} = 2.95 GeV/c from COSY.

In comparison to the ToPix 3 has the ToPix 4 an extended end-of-column logic and hitdata handling. Hitdata from all four double columns are send in frames with a frame number. This enables the creation of a unique time stamp and the sorting of the data on a bigger time scale. Figure 46 shows the hitdata displayed as a function of the time stamp. This measurement was done for ca. 13 minutes, covering 10 spills of the proton beam (extraction time and beam pauses). With this global time stamp the tracking of particles through the four ToPix 4 ASICS is possible and at the moment ongoing.

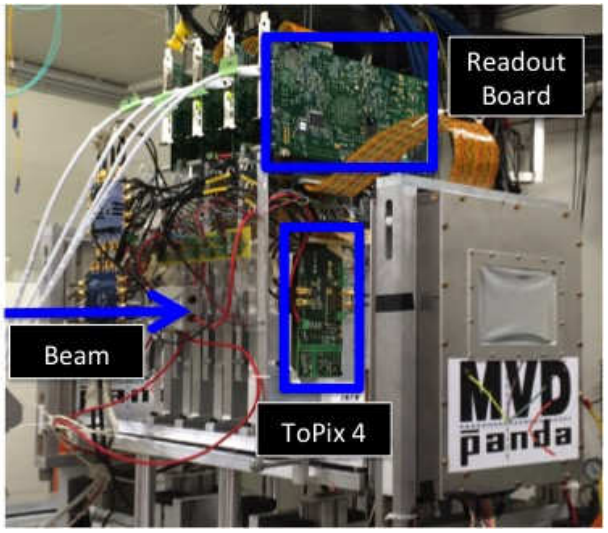

Fig. 45: Photograph of the testbeam setup of four ToPix 4 prototypes (center PCB) and the JDRS readout boards (upper PCB). The proton beam is coming from the left side.

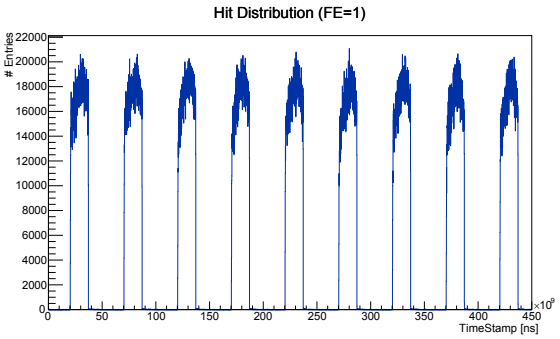

Fig. 46: Histogram of hitdata measured by ToPix 4 as a function of the global time stamp. In the histrogram the nine individual spills are clearly visible.

Various other measurements have been done during this testbeam. Figure 47 shows an example of the ongoing analysis. The hitmap of a single ToPix 4 is shown. The beam spot is visible in the upper part. The pixels of the first and the last row are connected to a sensor area which is twice as large as for the other pixels. Due to this these pixels see double the number of hits compared to the other pixels.

7.6 Development of a New Readout ASIC for the MVD Strip Detector

For the MVD's strip sensors, a readout front-end is being developed together with the INFN Torino group and the University of Gießen. The application specific integrated

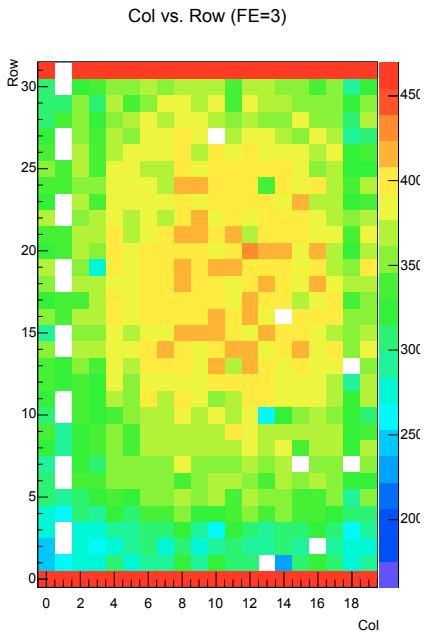

Fig. 47: Hitmap of a ToPix 4 during the testbeam. In the center part the beam spot is visible. The pixels in the first and the last row are connected to a sensor area which is twice as large as for other pixels. Thus they see twice as many hits.

circuit (ASIC) needs to deliver an accurate time (<10 ns) and charge (resolution: 8 bit) information, while using less than 4 mW per channel for an expected peak rate of 40 kHz per channel. Because of the given requirements, a simple architecture especially for the analog domain has to be used.

The ASIC fulfilling these requirements will be called $\overline{\text{P}}$ANDA Strip ASIC (PASTA) and its basic concept relies on leading-edge discriminators, providing time information for the crossing of a threshold from the input signal. With that, the time of arrival on the leading edge of the pulse is measured as well as the pulse length with a second point on the falling edge. The latter gives a time over threshold which is correlated with the collected charge and thus represents a measurement thereof.

Two discriminators with independent threshold levels are used to fulfill two goals: A precise time of arrival measurement is done with a low threshold ($V_{\text{th\_T}}$) to minimize the effect of time walk. [1] The second, higher threshold ($V_{\text{th\_E}}$) ensures a stable time over threshold measurement because noise fluctuations on the signal have less impact on the time jitter when the slope is steep (see Fig. 48).

While the main aspects of the development in the digital part has been reported already in last year's short contribution their finalization continued in 2014. This regards especially the completion of the newly designed control logic for data taking as well as the protection for radiation

[1] One is interested in the true starting time of the signal. Increasing the threshold will lead to delayed times because of the pulse's slope. This phenomenon is called time walk.

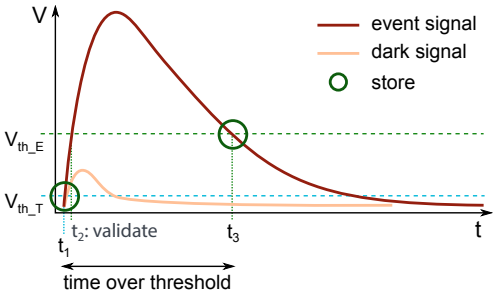

Fig. 48: A simplified signal after the pre-amplifier. Two discriminator levels deliver four points in time, t_1 and t_3 are stored in the default operation mode for the time of arrival and the time over threshold. Only if the signal exceed $V_{\text{thr\_E}}$ it is processed.

effects in the whole digital design.

Aiming at a final design, digital and analog parts have been combined and simulations performed to verify a proper functionality. This leads to a layout with an input channel pitch of 63.8 μm for 64 channels and an expected power consumption of less than 4 mW per channel.

In parallel to the ASIC's development, an adaptation of the readout system for ASICs, developed in the IKP's MVD group, towards PASTA has started. This includes the preparation for the expected event and configuration data format as well as the specifics of data transmission.

Final checks of the ASIC have to be done to verify a fully functional design which will be submitted to an ASIC foundry early 2015. Thorough testing of the prototype will follow, involving the afore-mentioned readout system whose adaptation to the PASTA interface must also be finished.

7.7 The $\overline{\text{P}}$ANDA - Straw Tube Tracker

The construction and installation of the PANDA-Straw Tube Tracker (STT) is being carried out in a joint project by institutions in Germany (FZ Jülich), Italy (LNF INFN Frascati, INFN and Univ. of Pavia, INFN and Univ. of Ferrara), Poland (IFJ PAN Krakow, Jag. Univ. Krakow, AGH Krakow), Romania (IFIN-HH Bucharest), and USA (North West. Univ. Evanston).

The IKP is responsible for parts of the mechanical construction and electronic readout system together with ZEA-2. A major task of IKP is the straw series production including assurance tests of all single straw tubes for the STT. By the end of 2013 a pre-series straw production run was carried out to verify all assembly steps and define the production quality controlling. The produced pre-series straws will be used for in-beam and dedicated pre-series tests of the STT system which are required by the $\overline{\text{P}}$ANDA -Collaboration and FAIR council. The final straw production for the PANDA-STT started in 2014. Including a large amount of spares about 8000 straws in total have to be produced in the upcoming years.

The simultaneous measurement of the drift time for the

spatial information and deposited charge for the specific energy-loss information, both with high resolution and in the $\overline{\text{P}}$ANDA specific environment of high particle intensities, variety of particle species, high multiplicities and broad momentum range, is a novel feature for a straw tracker. It requires the development of a new custom-designed electronic readout system for the STT. Two different readout concepts are under investigation, including test measurements to finally decide for the best suited option. The decision between the two concepts for the final readout of the STT will be based on the obtained performance results, the complexity of the readout system and economical considerations.

One concept is based on a full pulse shape measurement and analysis of the amplified and shaped straw signal by using a flash-ADC with FPGA readout for each channel. The pulse analysis done in the FPGA delivers the leading edge (LE) and pulse integral and has to be efficiently done in real-time at hit rates up to 1 MHz per straw channel. The pulse integral is a direct measurement of the deposited ionization charge by the track's energy-loss in a straw. The high sampling rate of 240 MHz of the flash-ADC guarantees a sufficient time resolution for the LE-measurement of about 1 ns. In this concept all electronics including the high voltage distribution are located outside the $\overline{\text{P}}$ANDA spectrometer. The individual straws are connected to single, about 10 m long coaxial cables which feed the signal on high voltage level to the transimpedance amplifiers integrated in the FADC readout boards.

The other concept is based on an amplifier-shaper-discriminator (ASIC) which measures the pulse start time and width (time-over-threshold) of a straw signal. Both time information are readout by a digitizing Time-Readout-Board (TRB). The ASIC features a charge preamplifier stage, a pole-zero cancellation network, a shaper stage, a tail cancellation network, a discriminator circuit, a baseline holder and a fast differential output (LVDS norm). The prototype chip has an additional analog output for each channel to deliver both, the digitized pulse information as well as the full analog pulse shape for a direct comparison. The control and settings of the ASIC parameters is done via FPGA implemented in the TRB readout boards. The electronic boards containing the ASICs and high voltage distribution are located front-end at the detector with few cm long cabling to the individual straws. The discriminator signals are transfered via about 10 m long micro twisted-pair cables to the TRB readout boards outside the $\overline{\text{P}}$ANDA spectrometer. The front-end boards feature a low power consumption of about 30 mW per channel to avoid a dedicated cooling system. The correlation between pulse width (time-over-threshold) and pulse amplitude has to be calibrated.

In 2014 a first series of test measurements (3×1 week) with proton and deuteron beams at COSY was carried out in the Big Karl beam area (Fig. 49). For each of the two different readout systems a separate straw prototype setup was used. Several scintillators and additional straw chambers were aligned in the beam line for monitoring the beam profile and for trigger and timing. In total measurements with six different proton beam momenta and three different deuteron beam momenta were carried out in the momentum range from 0.6 to 3.0 GeV/c. The tests of both readout systems consisting of proto-

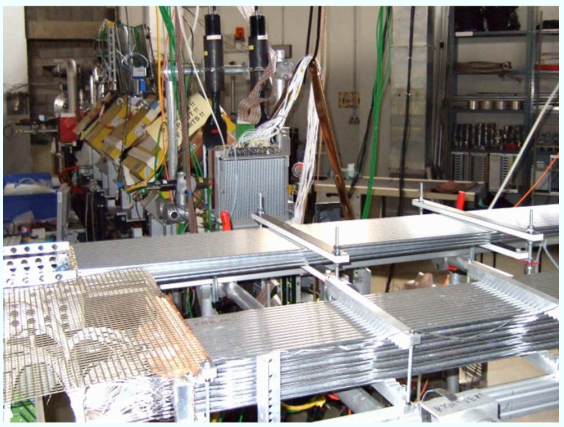

Fig. 49: The two straw prototype detector setups in the COSY Big-Karl beam area. The beam is coming from the back.

type setups, each with about 100 channels were successful. A first data-base of measurements with a pre-defined range of operation parameters (straw gas gain range, electronic amplification factors, discriminator threshold settings, high and low beam intensities, broad and narrow beam profiles) allows a systematic study of the measurement resolutions and efficiencies in connection to the specific settings. A large dynamical signal range of about a factor of 5 (dE/dx) in the straws was covered by the different proton and deuteron beam momenta.

In total about 50 data runs (1.6 GByte each) were taken for each momentum and for both readouts and separate data acquisitions. For the FADC-based readout also data in the so-called raw mode (recording and output of all sampling points) were taken to study and optimize the pulse shape analysis methods in detail. The analysis of the data-sets is still ongoing and is distributed to groups in Krakov, Pavia and Jülich. The goals are to determine the spatial resolution, the dE/dx-calibration and resolution in the time-over-threshold and charge measurements, fit dE/dx as a function of the momentum for the protons and determine the proton deuteron separation power. The data allow to check and verify the electronic readout designs, optimize the electronic parameters and the data analysis methods.

Figure 50 shows as an example the measured straw times and time-over-threshold (ToT) for the 800 MeV/c proton beam after a calibration of the times and ToT for each channel. The maximum drift times are about 150 ns. The ToT distribution shows the characteristic rise towards shorter drift times. A small beam induced background (multiple tracks) on the low percent level is visible at

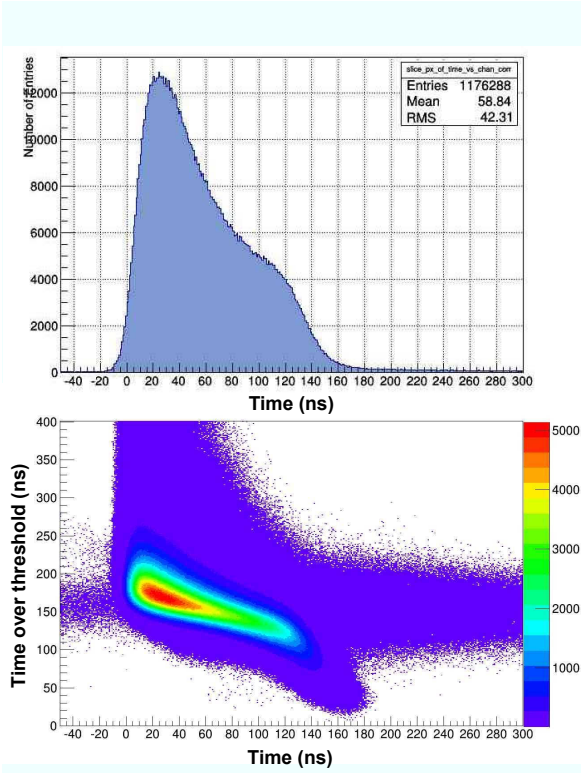

Fig. 50: Measured time and time-over-threshold for the 800 MeV/c proton beam (all times in ns). Upper: Time spectra for selected straws in the beam spot. Lower: Time-over-threshold versus time for all straws.

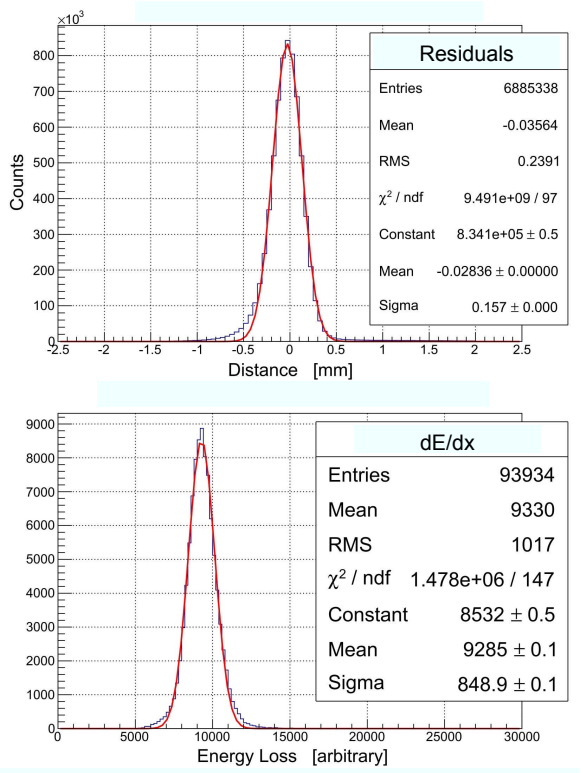

Fig. 51: Results of the beam tests for the FADC-based readout. Upper: Residual distribution of reconstructed tracks for 1.3 GeV/c proton beam. Lower: Specific energy-loss distribution (dE/dx) for the same proton beam momentum and after truncating the 20 % track hits with highest dE/dx.

times greater than 150 ns or less than -10 ns. The next steps in the analysis are the calibration of the isochrone - drift time relation and the track reconstruction to determine the spatial resolution. Then the ToT information to determine the specific energy-loss will be investigated for the proton and deuteron beams at different momenta.
For the prototype with the FADC-based readout a spatial resolution of the track reconstruction of about 155-160 μm and energy-loss resolution of 9.0-9.2 % has been obtained for protons with a momentum of 1.0, 1.3, and 2.0 GeV/c (see Fig. 51). The analysis of the proton-deuteron separation is still ongoing.
The COSY proton and deuteron beams in the momentum range of 0.6 to 3.0 GeV/c are ideally suited to test the PID capability of the STT and allow a direct extrapolation to the proton, kaon and pion separation power in the lower momentum region below 1 GeV/c of interest for $\overline{\text{P}}$ANDA.

7.8 KOALA Experiment at HESR

One goal of the $\overline{\text{P}}$ANDA experiment is to achieve an absolute precision of the luminosity determination $\frac{\Delta L}{L} \leq 3\%$ in order to fulfill the broad physics goals. Therefore, a concept for a luminosity monitor based on measuring antiproton-proton elastic scattering in the Coulomb-nuclear interference (CNI) region has been presented.

The idea is to track the antiprotons scattered near the beam axis with a multiple layer setup based on high-voltage monolithic active pixel sensors (HV-MAPS). The detector will be located about 10 m downstream from the interaction point and cover the polar angle range θ=3–8 mrad. Simulation studies indicated that the precision of the luminosity determination for the concept is limited by the small acceptance range of the squared 4-momentum transfer t covered by the detector. In order to achieve the desired precision of 3% it requires the knowledge of the physics quantities σ_{tot}, ρ and b describing the dependence of the antiproton- proton elastic cross section on t in the CNI region. To alleviate the poor knowledge of σ_{tot}, ρ and b for antiproton-proton interactions in the momentum region of $\overline{\text{P}}$ANDA, an independent experiment called KOALA at HESR, dedicated to the measurement of antiproton-proton elastic scattering, has been proposed.

The KOALA experiment at HESR will measure a large range of the squared 4-momentum transfer t-distribution of antiproton-proton elastic scattering in order to determine the parameters of total cross section σ_{tot}, the ratio, ρ, of the real part to the imaginary part of the forward elastic scattering amplitude and nuclear slope b. The idea is to measure the scattered beam particles at forward an-

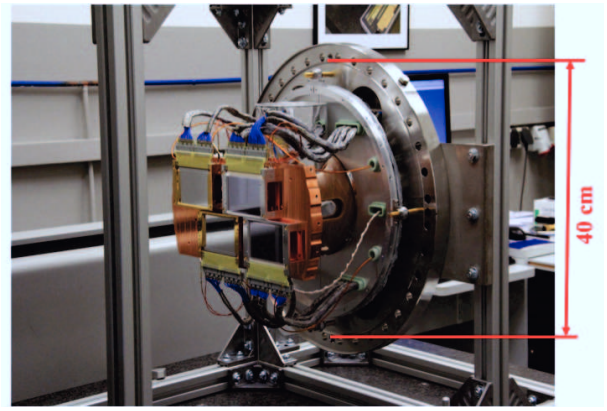

Fig. 52: Recoil detector assembled for a beam test at COSY. The two germanium detectors are fixed at the left side of the copper cold plate and two silicon detectors are located at the right side.

gles by tracking detectors and the recoil target protons near 90° by energy detectors. The $\overline{\text{P}}$ANDA luminosity monitor detector can be used for the forward measurement and the recoil protons will be measured by a new recoil detector. The forward measurement will track the scattered antiprotons. The recoil detector will measure both the kinetic energy and the polar angle of the recoil protons since t is directly proportional to the proton's kinetic energy T_{p}, i.e. $|t| = 2m_{\text{p}}T_{\text{p}}$. The recoil detector will measure the energy of the recoil protons within an angular range (recoil angle defined as $\alpha \equiv 90° - \theta_{\text{lab}}$) $0° < \alpha < 19°$.

7.8.1 Recoil Arm

One of the recoil arms of the KOALA experiment has been designed and built. It was commissioned at COSY by measuring proton-proton elastic scattering since the recoil particles are exactly the same for both antiproton-proton elastic scattering at HESR and proton-proton elastic scattering at COSY. To realize these ideas the recoil arm has been designed to match the existing hydrogen cluster target chamber at the ANKE platform at COSY.

A picture of the recoil detector as used for the commissioning is shown in Fig. 52. Two silicon strip sensors produced by MICRON with customized dimensions of 76.8 mm (length) x 50 mm (width) x 1 mm (thickness) have been placed at about 1 m from the target to cover the recoil angles, α=0°–5.7°. This corresponds to the region in which the silicon detector can stop the recoil protons with energies up to 12 MeV. Each silicon detector has 64 strips with 1.2 mm pitch. In addition, two germanium strip detectors produced by SEMIKON with 5 and 11 mm thickness have been set up in 2 rows as well. They can measure the recoil protons with energies up to 60 MeV. Both germanium detectors have 67 readout strips and a strip pitch of 1.2 mm in a sensitive area of 80.4 mm (length) x 50 mm (width).

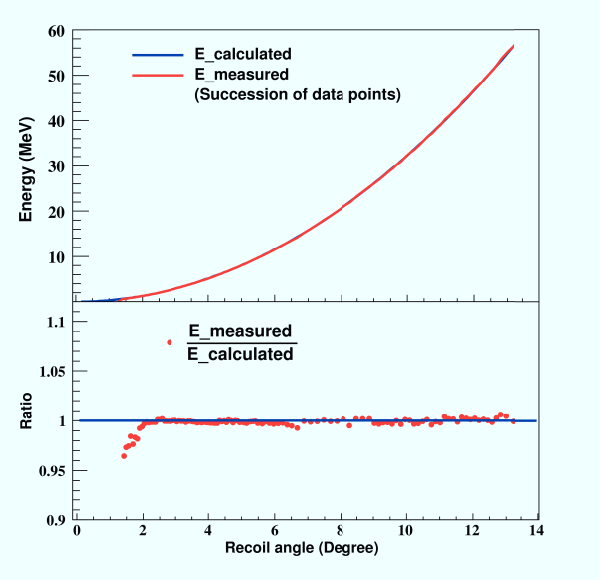

Fig. 53: (upper part) The blue line and red data points show the expected energy curve and measured energy of recoil protons as a function of recoil angle, respectively. The ratio between the measured to expected energy in a given strip is presented in the lower frame.

7.8.2 Commissioning at COSY

Data of the proton-proton elastic scattering at the beam momenta of 1.7, 2.5, 2.8 and 3.2 GeV/c have been taken in two separate commissioning weeks. All following results are based on the data sample at a beam momentum of 3.2 GeV/c.

After clustering a preliminary energy curve as a function of recoil angle is shown in the upper plot of Fig. 53. The measured energy in red overlapps the calculated ideal energy curve denoted in blue. The lower frame of Fig. 53 shows the ratio of the measured energy to the expected energy. The precision of 1% for energy measurement has been achieved after detector alignment.

The detector energy threshold is the minimum energy of the recoil protons for which the elastically scattered protons can be identified. It appears as the background signal rate becomes comparable or even higher than the signal in the small recoil angle region. The criteria to evaluate the energy threshold is to judge whether the proton signal is separable from the background. Figure 54 shows a plot of energy (after clustering) versus strip number measured by the first silicon detector at the smallest recoil angle as well as two single strip energy spectra. The two arrows on the energy plot of Si#1 point to the strips No. 4 and No. 20. The lower left histogram of Fig. 54 shows a clear recoil proton energy distribution on strip No. 4, which is separated from the background. The lower right corner of Fig. 54 depicts that the proton's energy measured by strip No. 20 partially overlaps the background. It indicates that it will be difficult to separate the interesting proton signal from the background when the recoil proton

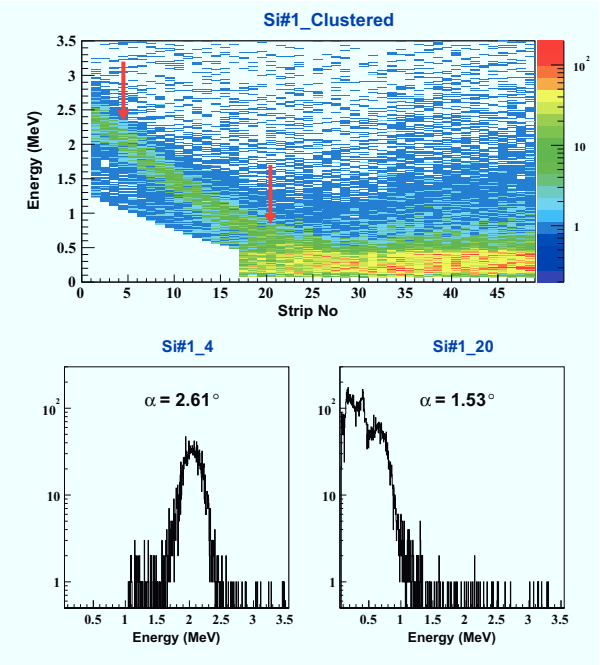

Fig. 54: (upper) Histogram of proton energy versus strip number of the first silicon detector. The lower histograms present the energy histograms of strip No. 4 (lower left) and No. 20 (lower right), which are marked by the red arrows in the upper frame.

energy is lower than 600 keV, i.e. $|t|$ =0.001 (GeV/c)^2. A coincidence with the forward measurement should enable a lower detector energy threshold. This can be expected when the full setup of the KOALA experiment at HESR is available.

7.9 Preassembly at IKP

The Pre-Assembling of the PANDA-Detector in Jülich aims at a significant gain of time in view of the final commissioning of the detector at FAIR. The functional interaction of the several complex detector components including the triggerless readout using a demonstrator data acquisition system (DAQ) will be probed at highest event rates using proton beams of COSY. Tests of individual detector components (STT, MVD, EMC, Shashlyk-calorimeter, TOF-system, forward tracking, luminosity monitor) are ongoing or in preparation, respectively in order to assure the claimed specifications of all modules. Currently in particular the STT and MVD –both already existing as prototype detectors– are tested. In combination with the EMC all pre-assembled detectors will be read out using the –to be developed– hardware-triggerless DAQ with the intention of proving the concept of reading out detectors having quite different time constants. Among the optimization of detector parameters, also calibrations are taking place or are in progress/planned. As for example the EMC consisting of 16000 crystals needs to be pre-calibrated using cosmic rays, but also π^0-decays

Fig. 55: Experimental hall at COSY for PANDA preassemly.

following the bombardement of Cluster-Jet targets with the COSY proton beam. For a later use at FAIR a cluster Jet target is required in order to test the performance with regard to density, beam life time, vacuum conditions in realistic beam environment. During the last few month, the former TOF-experiment has been removed from its location and the hall is now ready for hosting equipment to be tested in beam.

8 Further Experimental Activities

8.1 Polarized Fusion

The idea to use nuclear-polarized particles as fuel for future thermonuclear fusion reactors has been discussed since many years. For magnetic confinement as well as for inertial fusion the total cross section can be increased by a significant amount. Especially for the dominant nuclear fusion reaction, $d + t \rightarrow {}^4\mathrm{He} + n$ (and the $d + {}^3\mathrm{He} \rightarrow {}^4\mathrm{He} + p$ reaction), a factor of up to 1.5 is expected in the energy range relevant in a fusion reactor. In addition, the polarization of the projectiles allows control of the ejectile trajectories. At plasma energies below 50 keV the differential cross section only weakly depends on the angular distribution of the ejectiles. At higher energies a preference for forward and backward scattering appears. This effect can be increased or decreased by using polarized fuel and offers the possibility to simplify the energy extraction from the plasma to the reactor wall or to concentrate the neutron flux onto defined wall areas. In general, the energy gain of a fusion reactor does not depend linearly on the total cross section. Simulations for ITER have shown that the energy output can be increased by a factor of 2 with polarized fuel. Besides the cross section increase the focusing of the ejectiles can be used to concentrate the neutron flux on the outer blanket. Therefore, less cooling would be needed for the inner wall and the coils to induce the magnetic field can be mounted closer to the plasma. This, in turn, will increase the magnetic field B inside the plasma and further boosts the energy output ($\sim B^{7.84}$). For laser-induced inertial fusion the energy gain can also be increased and the laser power can be reduced in parallel, which will decrease the acquisition costs appreciably.
Although polarized fuel seems a promising method to increase the efficiency of future fusion reactors, a few fundamental questions still must be answered:

8.1.1 What is the spin-dependence of the *dd*-fusion reactions?

For the reactions $d + d \rightarrow t + p$ and $d + d \rightarrow {}^3\mathrm{He} + n$, which are mostly used in all experimental fusion setups until now and will always contribute in parallel to the main fusion reaction, the situation is unclear. Therefore, the measured value of the so called "quintet-suppression factor", the ratio of the total cross section $\sigma_{1,1}$ for parallel deuteron spins (quintet state) to the unpolarized total cross section σ_0, is very interesting for fundamental physics to test the different predictions. In a dedicated experiment, under preparation at the PNPI in Gatchina, Russia, and in collaboration with the University of Ferrara, Italy, as well as the IKP, it is planned to measure the spin-correlation coefficients of the DD reactions at energies below 100 keV. From these measurements the behavior of the differential and the total cross sections as a function of different combinations of polarized deuterons can be deduced. Even if the parallel spin adjustment turns out to be not helpful, other spin combinations might help to suppress the neutrons for neutron-lean reactors or increase both total cross sections for a higher energy output. First components of the setup, *e.g.* the polarized deuteron source, are operating and the experiments will start in summer 2015.

8.1.2 How to produce and store enough polarized fuel?

In order to feed a Tokamak reactor an amount of more than 10^{21} polarized atoms per second is needed. This seems not to be a problem for ^{3}He and T, which both can be polarized by optical pumping in macroscopic amounts. But pure polarized deuterium atoms are produced by atomic beam sources (ABS) only and this will limit the production to about 5×10^{16} deuterium atoms per second. In addition, these radical atoms cannot be stored. In collaboration between the University of Cologne, PNPI and IKP the recombination of nuclear polarized atoms on different surfaces was investigated to avoid depolarization. One important outcome of this joined project was that it is possible to recombine polarized hydrogen atoms into molecules without polarization losses on special surfaces. With this method the production of polarized deuterium molecules will be investigated in 2015. In a further step we will try to freeze out these molecules and to store them without polarization losses for a reasonable time.

8.1.3 Does the polarization survive in the different fusion plasmas?

In 1982 Kulsrud et al. predicted that the lifetime of polarized fuel in a Tokamak reactor should be sufficiently long to influence the total cross section. However, this statement has not been verified experimentally yet. A first proposal of such a test measurement for the DIII Tokamak in San Diego was published recently. The same problem appears for laser-induced fusion. A collaboration of the Heinrich-Heine University Düsseldorf and PGI-6 and IKP of the FZJ is now investigating this question with the help of high-power (few 100 TW) lasers. The idea is to produce beams of polarized $^3\mathrm{He}^{++}$ ions by ionizing polarized ^{3}He gas and accelerating the ions to energies in the lower MeV range. If the nuclear polarization of the ^{3}He atoms is conserved at least partially in the $^3\mathrm{He}^{++}$ ions, this proofs for the first time that nuclear polarization can survive in laser-induced plasmas. In a first test measurement at the PHELIX laser at GSI Darmstadt it was recently shown that both single- and double-ionized ^{4}He and ^{3}He ions can be produced by laser-acceleration from a gas jet up to energies of 9 MeV. Figure 56 shows the helium ion signals behind a Thomson parabola spectrometer at ion emission angles 90° relative to the laser-propagation direction. As the next step the $^3\mathrm{He}^{++}$ ions will be laser-accelerated from polarized ^{3}He atoms and their polarization will be measured with a nuclear-reaction polarimeter. For this secondary scattering reaction, the ^{3}He ions will be directed on a CD_2 foil

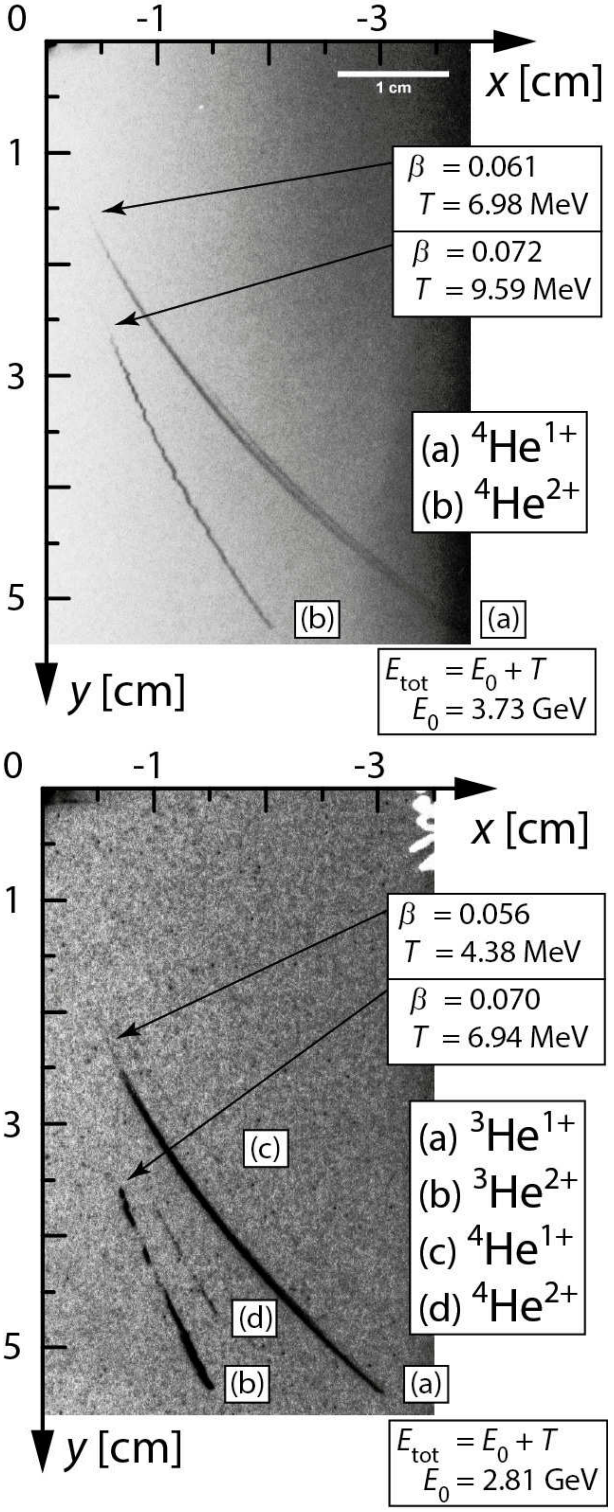

Fig. 56: Signal of laser-accelerated $^{3,4}He^{1+,2+}$ ions from the PHELIX laser at GSI Darmstadt.

where they will fuse with deuterium. The angular distribution of the secondary protons from the D(^{3}He, p)^{4}He reaction carry the information about the polarization of the incoming laser-accelerated ^{3}He ion beam. A similar polarimeter, based on the elastic proton scattering off silicon, has already been used for measurements with laser-accelerated proton beams. For the measurements with helium ions it has been calibrated at the Jülich TANDETRON which accelerates unpolarized $^3He^{2+}$ ions to energies of ~ 2 MeV and beam currents of up to nA.

8.2 ATHENA—Proposal for an HGF infrastructure for Accelerator R & D

The Helmholtz Centers are playing a leading role for the development and operation of particle accelerators in Germany. Ten-thousands of users from science, medicine and industry rely on the high-quality particle beams and light pulses that are supplied by the HGF user facilities. Continuous developments and integration of new technologies are of highest relevance to strengthen the competitiveness of accelerator-based research in the international scope.

The HGF centers DESY, FZJ ((represented by M.Büscher (Peter-Grünberg-Institute) and A.Lehrach), GSI with HI-Jena, HZB, HZDR und KIT, together with partner universities, have identified plasma technology as the tool to realize ultra-compact (and cost-efficient) accelerators for electrons, protons, ions and photons. Consequently, these centers have proposed a common "Accelerator Technology HElmholtz iNfrAstructure" ATHENA (https://www.helmholtz-ard.de/e234535/), in order to development this technology towards a regular user operation.

At the Forschungszentrum Jülich research for ATHENA will be performed at JuSPARC, the Jülich Short-Pulsed Particle and Radiation Centre (http://www.fz-juelich.de/jusparc). JuSPARC is planned to be built next to the COSY accelerator hall; it will be an interdisciplinary center for collaborative research with ultra-short pulsed photon and particle beams. These beams will be generated employing the radiation from a high-power, short-pulse laser (power above 1 PW at pulse durations in the 10 fs range) with highest possible repetition rate, using nonlinear up-conversion in the case of photons and novel target technologies for the production of (polarized) particles.

Within JuSPARC, IKP-4 will be in charge of experiments aiming at the generation of polarized hadron beams, in particular of $^3He^{2+}$ ions. First experiments in this direction have already been performed at the Arcturus Laser facility of Düsseldorf University and at PHELIX/GSI. As a result of the experiments, a method to measure the degree of polarization of Laser-accelerated particles has been developed [Phys. Plasmas 21, 023104 (2014)] and the ion acceleration from a He-gas target to energies up to a few MeV has been achieved (see section 8.1.3, Fig. 56).

9 Theoretical Investigations

9.1 Introduction

The IKP theory group studies the strong interactions in their various settings — spanning topics in hadron structure and dynamics, the nuclear many-body problem and symmetry tests in Quantum Chromodynamics (QCD) as well as physics beyond the Standard Model. The first focus of the theory group is the formulation and application of effective field theories for precision hadron and nuclear physics based on the symmetries of QCD. The second focus is related to high performance computing in nuclear and hadronic physics, spear-headed by the work on nuclear lattice simulations. Since July 2012, the group is heavily involved in the activities of the collaborative research center "Symmetries and the emergence of structure in QCD" (CRC 110) together with researchers from Bonn University, TU München, IHEP (Beijing, China) and Peking University (China). Some of the high-lights of these activities are discussed in the following.

9.2 Precision NN potential at fifth order in the chiral expansion

Chiral effective field theory (EFT) provides a solid foundation for analyzing low-energy hadronic observables in harmony with the symmetries of quantum chromodynamics (QCD), the underlying theory of the strong interactions. It allows one to derive nuclear forces and currents in a systematically improvable way order by order in the chiral expansion, based on a perturbative expansion in powers of $Q \in (p/\Lambda,\, M_\pi/\Lambda)$, where p refers to the magnitude of the three momenta of the external particles, M_π is the pion mass and Λ is the breakdown scale of chiral EFT. Being combined with modern few- and many-body methods, the resulting framework based on solving the nuclear A-body Schrödinger equation with interactions between nucleons tied to QCD via its symmetries represents nowadays a commonly accepted approach to *ab initio* studies of nuclear structure and reactions

First, we have constructed improved nucleon-nucleon potentials derived in chiral effective field theory up to next-to-next-to-next-to-leading order (N3LO). We argue that the nonlocal momentum-space regulator employed in the earlier chiral two-nucleon potentials is not the most efficient choice, in particular since it affects the long-range part of the interaction. We are able to significantly reduce finite-cutoff artefacts by using an appropriate regularization in coordinate space which maintains the analytic structure of the amplitude. The new potentials do not require the additional spectral function regularization to cut off the short-range components of the two-pion exchange and make use of the low-energy constants c_i and d_i determined from pion-nucleon scattering without any fine tuning. We also introduce a new procedure for estimating the theoretical uncertainty from the truncation of the chiral expansion that replaces previous reliance on cutoff variation.

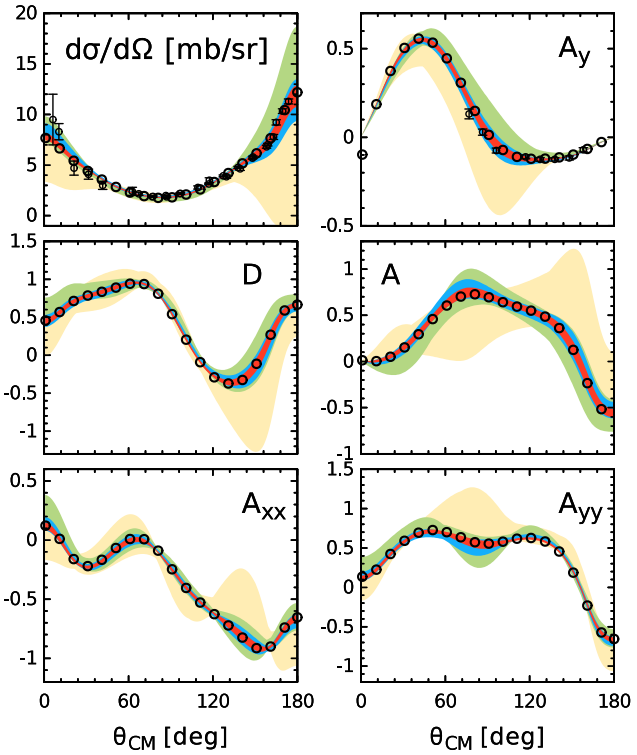

Fig. 57: Predictions for the np differential cross section $d\sigma/d\Omega$, the vector analyzing power A_y, the polarization transfer coefficients D and A and the spin correlation parameters A_{xx} and A_{yy} at $E_{\rm lab} = 200\,$MeV calculated up to N4LO. Open circles refer to the result of the Nijmegen PWA. The bands of increasing width show the estimated theoretical uncertainty at N4LO (red), N3LO (blue), N2LO (green) and NLO (yellow).

Second, we have worked out the nucleon-nucleon potential at fifth order in chiral effective field theory (N4LO). We find a substantial improvement in the description of nucleon-nucleon phase shifts as compared to the N3LO results. This provides clear evidence of the corresponding two-pion exchange contributions with all low-energy constants being determined from pion-nucleon scattering. The N4LO corrections to nucleon-nucleon observables appear to be of a natural size which confirms the good convergence of the chiral expansion for nuclear forces, see Fig. 57. Furthermore, the obtained results provide strong support for the novel way of quantifying the theoretical uncertainty due to the truncation of the chiral expansion. This work opens up new perspectives for precision *ab initio* calculations in few- and many-nucleon systems and is especially relevant for ongoing efforts towards a quantitative understanding the structure of the three-nucleon force in the framework of chiral effective field theory. For more information see arXiv:1412.4623 [nucl-th].

9.3 Ab initio calculation of the sprectum and structure of ^{16}O

Nuclear lattice simulations have been established as a new quantum many-body method that allows for truely *ab initio* calculation of the properties of atomic nuclei. Here, we report on the investigation of the spectrum and structure of ^{16}O. In fact, since the early work of Wheeler in 1937, there have been quite a few theoretical studies of ^{16}O based on alpha cluster models and some experimental evidence for alpha-particle states in ^{16}O from the analysis of decay products has been reported. While such models have been able to describe some of the puzzles in the structure of ^{16}O on a phenomenological (or geometrical) level, there has so far been no support for the alpha cluster structure of ^{16}O from first-principles calculations. In the framework of nuclear lattice simulations we have calculated of the low-lying even-parity states and have provided evidence that the nucleons in the ground state of ^{16}O are arranged in a tetrahedral configuration of alpha clusters. For the first excited 0^+ state, we find a predominantly square configuration of alpha clusters, the rotational excitations of which include the first 2^+ state, cf. Fig. 58. These cluster configurations can be obtained in two ways. First, one can investigate the time evolution of the various cluster onfigurations shown in Fig. 58 and extract e.g. the corresponding energies as the Euclidean time goes to infinity. Second, one can also start with initial states that have no clustering at all. One can then measure the four-nucleon correlations. For such initial states, this density grows with time and stays on a high level. For the cluster initial states, these correlations start out at a high level and stay large as a function of Euclidean time. This is a clear indication that the observed clustering is not build in by hand but rather follows from the strong four-nucleon correlations in the ^{16}O nucleus. The energies for the lowest even-parity states come out close to their experimental values, we find $E(0_1^+) = -131.3(5)\,[-127.62]$, $E(0_2^+) = -123(2)\,[-121.57]$, $E(2_1^+) = -123(2)\,[-120.70]$, all in MeV and the numbers in the square brackets refer to experiment. We have also calculated the correponding charge radii r, the quadrupole moments Q, and the electromagnetic transition amplitudes for $E2$ and $E0$ transitions at LO. When accounting for the underbinding at LO by rescaling, the corresponding numbers are in agreement with experiment. In particular, we are able to explain the empirical value of $B(E2, 2_1^+ \to 0_2^+)$, which is $\simeq 30$ times larger than the Weisskopf single-particle shell model estimate. This provides further confirmation of the interpretation of the 2_1^+ state as a rotational excitation of the 0_2^+ state. Much remains to be studied in the ^{16}O system, such as the computation of the odd-parity spectrum and the inclusion of corrections beyond LO for the electromagnetic observables. For more information see Phys. Rev. Lett. **112** (2014) 10, 102501 [arXiv:1312.7703 [nucl-th].

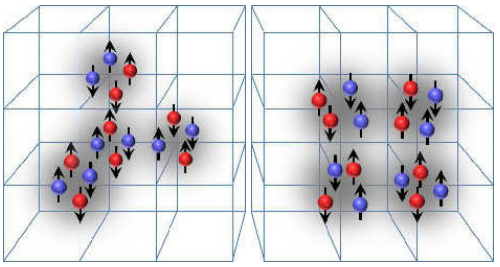

Fig. 58: Schematic illustration of the alpha cluster initial states with tetrahedral (left) and square (right) configurations.

Fig. 59: Flow-time dependence of the topological susceptibility $\chi_{\rm top}$ at 3 different lattice spacings (β values).

9.4 The QCD topological susceptibility from the gradient flow

Lattice QCD (LQCD) calculations offer the possibility of numerically evaluating hadronic observables directly from QCD. Here we report on our investigations on calculating hadronic matrix elements relevant to symmetry tests in both QCD and beyond the Standard Model, using the "Gradient Flow" technique first introduced, in the context of QCD, by Lüscher. Though steady progress has been made in calculating the binding and scattering energies of few hadron systems, calculations of hadronic matrix elements continue to suffer from poor signal-to-noise ratio. Furthermore, the operator structure of these matrix elements typically have unwanted renormalization mixings within LQCD regulator, which in turn makes the extrapolation of matrix elements to the continuum limit very difficult, if not impossible. Many of these issues can be alleviated, and in some cases eliminated, by using the Gradient Flow.

When implementing the Gradient Flow, operators are evolved to an additional time direction, the so-called flow-time direction (in addition to the usual 3 spatial and 1 temporal directions of LQCD). The determination of these operators at positive flow-time is done after the usual LQCD generation of gauge configurations, and so

the computational effort to implement the Gradient Flow is controllable. As opposed to operators within the normal LQCD framework (i.e. at zero flow-time), operators at non-zero flow time have much better renormalization behaviour, as was formally shown by Lüscher. Our early investigations of the topological susceptibility confirm this behaviour and demonstrates the power of the Gradient Flow for lattice QCD calculations. In Fig. 59 we show the flow-time dependence of the topological susceptibility χ_{top} for three different β couplings, corresponding to three different lattice spacings. In the continuum limit for every flow time $t > 0$ we expect the topological susceptibility to be independent of the flow-time t. In this case we can perform a safe continuum limit at a given fixed value of the flow-time t and the final result should be independent of t. As can be seen from Fig. 59, excluding a very small region close to the t = 0 boundary where cutoff effects dominate, the topological susceptibility is essentially flow-time independent and suffers, within the current statistical precision, small discretization uncertainties. A continuum extrapolation can now be performed.
This particular calculation of the topological susceptibility (and from it the topological charge) is a necessary component to calculating the nucleon EDM coming from the strong-θ term in QCD. In the near future we will also use the Gradient Flow to investigate higher dimension operators whose origins come from BSM physics.
For more information see PoS LATTICE **2014** (2014) 251 [arXiv:1409.2735 [hep-lat]].

9.5 Electric dipole moments of the deuteron, helion and triton

Electric Dipole Moments (EDMs) of sub-atomic particles imply the simultaneous violation of parity (P) and time-reversal (T) symmetry and hence by the CPT theorem also the violation of CP, where C denotes the charge-conjugation symmetry. According to a theorem of the eminent Russian physicist Andrey Sakharov, CP violation is one of the necessary conditions that the matter surplus in our universe has dynamically been generated during its evolution. However, the CP violation by the complex phase of the Cabibbo-Kobayashi-Maskawa (CKM) matrix of the Standard Model (SM) is insufficient to account for the matter-antimatter asymmetry observed by the successive KOBE, WMAP, and Planck satellite missions. Thus there is empirical evidence that other mechanism(s) of CP violation within and/or beyond the SM have to exist.
A single measurement of a non-zero EDM signal, even though such a result would already be spectacular by itself, would not suffice to identify the underlying source(s) of P and T violation. Rather EDM measurements of several light nuclei are in general required to impose constraints on the sources of P and T violation within and beyond the SM.
We were able to show that the proposed measurements of the electric dipole moments of light nuclei in storage rings would put strong constraints on models of flavor-diagonal CP violation. In fact, we have succeeded to do the first *consistent and complete* calculation of *all* nuclear interactions (including two-nucleon contact and genuine three-nucleon ones) relevant and contributing to the EDMs of deuteron, helion and triton up to and including next-to-leading order in the framework of chiral effective field theory, the extension of chiral perturbation theory to baryon systems.
In this way, a *controlled and systematic* evaluation of the EDMs of light nuclei has become feasible in complete generality — only the pertinent prefactors of these interactions have still to be determined by lattice QCD or estimated by NDA (naive dimensional analysis) or other ways from the underlying CP-violating dimension-six sources or models as *e.g.* supersymmetric models, two-Higgs models etc. Moreover, the confirmation or falsification of scenarios with a dominating QCD θ-term or a minimal left-right symmetric interaction are in the future possible, *without* any further theoretical input, just from the comparison of our predictions to the experimental data of the neutron, proton, deuteron, and helion EDMs.
In particular, the EDM contributions induced by the CP-violating three-pion operator were calculated for the first time. They do not only renormalize the CP- and isospin-violating pion-nucleon coupling by nearly 50% but also introduce a non-locality into this interaction which might be of relevance especially at higher nuclear densities, as for instance for the nuclei in atomic or molecular EDM measurements. Furthermore, we have discovered the effects of CP-violating nucleon-nucleon *contact* interactions to be at least an order of magnitude larger than those found in previous studies based on phenomenological models for the CP-conserving nucleon-nucleon interactions. In fact, these contact interactions cannot be neglected any longer — as it is still the case for EDM studies with diamagnetic atoms — whenever color-gluonic dimension-six sources are of comparable order as their (color)-quark counter parts. arXiv:1411.5804 [hep-ph].

9.6 Hyperons in nuclear matter

Recently, we derived a hyperon-nucleon (YN) interaction up to next-to-leading order (NLO) in chiral effective field theory (EFT). It involves contributions from one- and two-pseudoscalar-meson exchange diagrams (π, K, η) and from four-baryon contact terms without and with two derivatives. SU(3) flavor symmetry is imposed for constructing the YN interaction. The assumed SU(3) symmetry allows us to fix all the coupling constants at the various meson-baryon vertices, and it reduces the number of free parameters which arise within the EFT approach in form of low-energy constants (LECs) associated with the aforementioned contact terms. With this interaction an excellent reproduction of available low-energy ΛN and ΣN scattering data could be achieved as reflected in a total χ^2 of about 16 for the 36 data points included in the

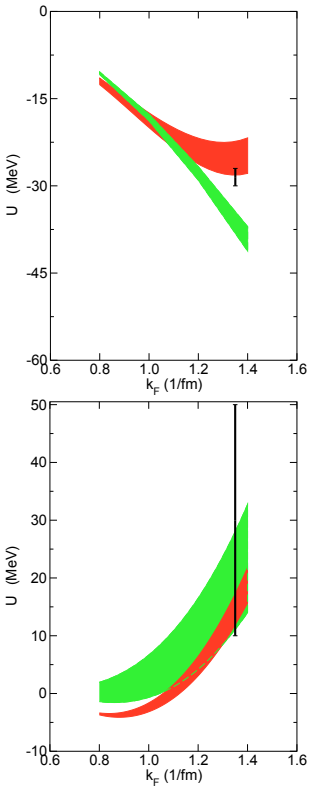

Fig. 60: The s.p. potentials $U_\Lambda(p_\Lambda = 0)$ and $U_\Sigma(p_\Sigma = 0)$ as a function of the Fermi momentum k_F. Results for our NLO (LO) interaction are indicated by red (green) bands. The black lines indicate the "empirical" values.

fit.

Now we investigated also the properties of our YN interactions in nuclear matter. Specifically, we calculated the single particle (s.p.) potential of the Λ and Σ hyperons in nuclear matter obtained in a conventional G-matrix calculation based on the standard (gap) choice for the intermediate spectrum. The hyperon s.p. potentials in symmetric nuclear matter provide further insight into the properties of the elementary YN interaction.

Results for the Λ s.p. potential $U_\Lambda(p_\Lambda)$ at $p_\Lambda = 0$ are presented in Fig. 60 as a function of the Fermi momentum k_F. The latter is related to the nuclear density by $\rho = (2/3\pi^2)k_F^3$. The bands indicate uncertainties due to the employed regularization scheme. At the saturation point of nuclear matter where $k_F = 1.35$ fm^{-1} our NLO calculation (red band) suggests a potential depth of around 25 MeV. This is very well in line with the "empirical" value for the Λ binding energy in nuclear matter of about -28 MeV, deduced from the binding energies of finite Λ hypernuclei (and indicated by the black line in Fig. 60). The leading-order (LO) interaction (green band) yields a depth of around 36 MeV at the saturation point. Interestingly, in case of the NLO interaction one observes an onset of repulsive effects already at rather moderate densities. Such repulsive interactions play an important role in the discussion of dense baronic matter and the constraints derived from massive neutron stars.

The Σ-nuclear potential is found to be repulsive, in agreement with phenomenological information (cf. Fig. 60). Furthermore, it turned out that a weak Λ-nuclear spin-orbit interaction, suggested by measurements of level splittings for specific hypernuclei, can be achieved within our framework by an appropriate adjustment of a particular LEC corresponding to an antisymmetric ΛN–ΣN spin-orbit interaction that arises at NLO in chiral EFT. For more information see Nucl. Phys. A **936** (2015) 29 [arXiv:1411.3114 [nucl-th]].

9.7 Is the $Y(4260)$ a $D_1\bar{D}$ molecule?

Traditionally, (heavy) mesons were described in the classification of the most simple realization of the quark model, where mesons are treated as $\bar{q}q$ states. This has been challenged in recent years by a large number of mesonic states discovered in the mass range of heavy quarkonia. This is especially obvious for the $Z_c^+(3900)$, $Z_c^+(4020)$, $Z_b^+(10610)$ and $Z_b^+(10650)$ since they are charged but decay either via transitions to heavy quarkonia or decays into open charm or bottom states. But there is also a significant number of neutral hidden flavor states which neither in mass nor in decay patterns match to the quark model. A prominent player amongst those is the $Y(4260)$. Although high above the lowest open charm threshold, it does not decay into $\bar{D}D$, but was so far only seen in the $J/\psi\pi\pi$, the $\gamma X(3872)$ and possibly the $h_c\pi\pi$ final states. We proposed recently that the $Y(4260)$ could be predominantly a $D_1(2420)\bar{D}$ (understood as a short hand notation for the state with $C = -$) bound system, for this would explain naturally why the $Z_c^+(3900)$ was seen in the $Y(4260) \to J/\psi\pi\pi$ and the $X(3872)$ in $Y(4260) \to X(3872)\gamma$ if both the Z_c and the X were predominantly $D^*\bar{D}$ systems. In a subsequent work to be presented here we discussed some additional implications of that assignment.

A shallow bound state of two stable mesons strongly couples to its constituents, which leads to very much enhanced near threshold cross sections for the scattering of those particles. In case of a resonance formed from two mesons, which is unstable due to unstable constituents and possible transitions of the constituents to lighter final states, this key feature turns into unusual line shapes. In case of the $Y(4260)$ we found that a large $D_1(2420)\bar{D}$ component leads to an asymmetric line shape of the $Y(4260)$ in the $J/\psi\pi\pi$ final state (cf. upper panel of Fig. 61) as well as the $h_c\pi\pi$ final state. In consequence within our study the $Y(4260)$ turned out to have a mass of the order of 4220 MeV, significantly reduced in comparison to the mass of 4260 MeV deduced from a fit to the same data using a symmetric Breit-Wigner function.

In addition, we also investigated the decay of the $Y(4260)$ into $D^*\bar{D}\pi$. Since $D^*\pi$ is the main decay mode of the $D_1(2420)$, this final state is the one that most directly accesses the constituents of the $Y(4260)$, if it is dominated by its molecular component. It turns out that in this sce-

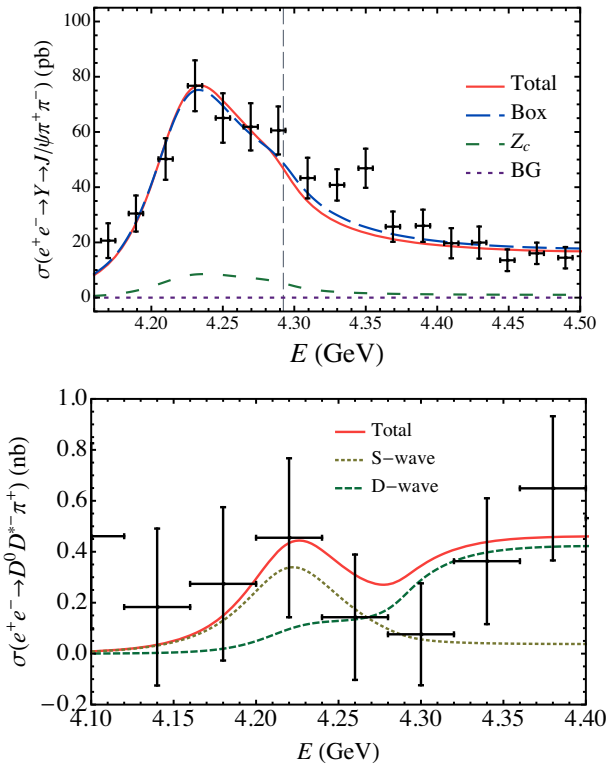

Fig. 61: Unusual line shapes of the $Y(4260)$ from a prominent $D_1(2420)\bar{D}$ component. Upper panel: line shape in the $J/\psi\pi\pi$ channel. Lower panel: line shape predicted for the $D\bar{D}^*\pi$ channel.

nario the cross section predicted for $e^+e^- \to D\bar{D}^*\pi$ is indeed quite unusual (cf. lower panel of Fig. 61), since the rate above the nominal $D_1\bar{D}$ threshold located at around 4.29 GeV is as high as the rate at the peak related to the $Y(4260)$. Other key observables are the angular distributions of the $D\bar{D}^*\pi$ final state, since we also found that the D–wave nature of the decay $D_1(2420) \to D^*\pi$ leaves a visible imprint in the observables. We regard these prediction as *the* smoking gun to prove or disprove a prominent molecular nature of the $Y(4260)$. For more information see Phys. Rev. D **90** (2014) 7, 074039 [arXiv:1310.2190 [hep-ph]].

9.8 Phonon effects in radiative neutron capture cross sections

Radiative neutron capture plays an important role in nucleosynthesis during the r-process. Astrophysical calculations require cross sections both for stable nuclei and unstable neutron-rich isotopes whose life times are too short for experimental investigations with presently available technology. Nuclear many-body theories based on effective nucleon interactions allow extrapolations to short-lived isotopes. Most available calculations employ the mean field approximation that tends to underestimate the neutron capture cross sections in the experimentally known stable isotopes. The phonon degree of freedom provides important correlations neglected in the mean field approximation. In the last decade, a *self consistent* treatment of the phonons has been developed, the so-called *Quasiparticle Time Blocking Approximation (QTBA)*. It relies on effective interaction of the Skyrme family that reproduce both binding energies and radii of the known isotopes. In Fig. 62, the radiative neutron capture cross section leading to the isotope ^{120}Sn obtained within the QTBA is compared with experimental data. Uncertainty bands due to incomplete knowledge of the s-wave resonance spacing are shown. A significant enhancement of the neutron capture cross sections with respect to the mean field approximation(QRPA;blue) is found. Recently, gamma ray strength functions for Sn-isotopes below the neutron separation threshold have been determined using the (^{3}He, ^{3}He' γ) reaction. The present method is able to reproduce the experimental strength functions in ^{118}Sn and ^{122}Sn below 5 MeV. In the neutron-rich isotope ^{72}Ni, it predicts an enhancement of the electromagnetic dipole strength in the vicinity of 12.4 MeV. For more information see arXiv:1412.0268 [nucl-th].

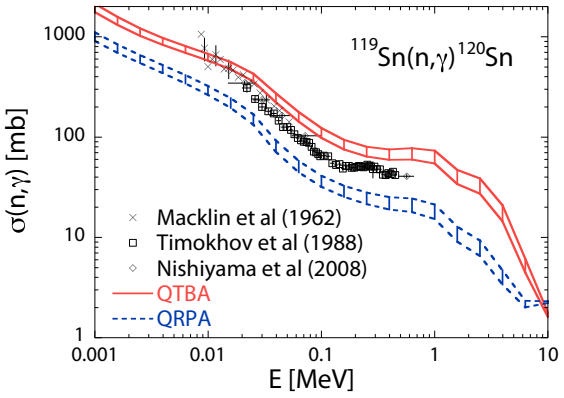

Fig. 62: Radiative neutron capture cross section for ^{120}Sn.

A Councils

A.1 PAC – COSY Program Advisory Committee

(until February 2014)

Prof. M. Anselmino	L'Universita di Torino, Italy
Prof. E. Epelbaum	Universität Bochum, Germany
Prof. M. Garçon	CEA-Saclay, France (Chairperson)
Prof. N. Kaiser	TU München, Germany
Prof. B. Kämpfer	FZ Dresden-Rossendorf, Germany
Prof. O. Kester	GSI Darmstadt, Germany
Prof. A.K. Opper	George Washington University, USA
Prof. P. Salabura	Jagellonian University Cracow, Poland
Prof. U. Thoma	Universität Bonn, Germany
Prof. H. Weise	DESY, Hamburg, Germany
Prof. H. Wilschut	KVI Groningen, Netherlands

A.2 CBAC – COSY Beam Time Advisory Committee

(since December 2014)

Prof. K. Aulenbacher	Universität Mainz, Germany
Prof. A. Chao	SLAC Stanford, USA
Prof. O. Kester	GSI Darmstadt, Germany
Prof. C.J. Schmidt	GSI Darmstadt, Germany
Prof. E. Steffens	Universität Erlangen-Nürnberg, Germany (Chairperson)
Prof. G. Trubnikov	JINR Dubna, Russia
Prof. M. Weber	KIT, Karlsruhe, Germany

B Publications–Journal Articles

B.1 Journals

1. **Observation of $e^+e^- \to \gamma X(3872)$ at BESIII**
   M. Ablikim *et al.*
   Phys. Rev. Lett. **112** 092001 (2014)

2. **Precision measurements of $B(D^+ \to \mu^+\nu_\mu)$, the pseudoscalar decay constant f_{D^+}, and the quark mixing matrix element $|V_{cd}|$**
   M. Ablikim *et al.*
   Phys. Rev. D **89** 051104 (2014)

3. **Observation of a charged $(D\overline{D}^*)^\pm$ mass peak in $e^+e^- \to \pi D\overline{D}^*$ at $\sqrt{s} = 4.26$GeV**
   M. Ablikim *et al.*
   Phys. Rev. Lett. **112** 022001 (2014)

4. **Observation of a Charged Charmoniumlike Structure in $e^+e^- \to (D^*\overline{D}^*)^\pm\pi^\mp$ at $\sqrt{s} = 4.26$GeV**
   M. Ablikim *et al.*
   Phys. Rev. Lett. **112** 132001 (2014)

5. **Charge symmetry breaking in $dd \to {}^4\mathrm{He}\pi^0$ with WASA-at-COSY**
   P. Adlarson *et al.*
   Phys. Lett. B **739** 44 - 49 (2014)

6. **Measurement of the $\eta \to \pi^+\pi^-\pi^0$ Dalitz plot distribution**
   P. Adlarson *et al.*
   Phys. Rev. C **90** 045207 (2014)

7. **Neutron-proton scattering in the context of the $d^*(2380)$ resonance**
   P. Adlarson *et al.*
   Phys. Rev. C **90** 035204 (2014)

8. **Cross section ratio and angular distributions of the reaction $p + d \to {}^3\mathrm{He} + \eta$ at 48.8 MeV and 59.8 MeV excess energy**
   P. Adlarson *et al.*
   Eur. Phys. J. A **50** 100 (2014)

9. **Evidence for a New Resonance from Polarized Neutron-Proton Scattering**
   P. Adlarson *et al.*
   Phys. Rev. Lett. **112** 202301 (2014)

10. **A framework for the calculation of the $\Delta N\gamma^*$ transition form factors on the lattice**
    A. Agadjanov *et al.*
    Nucl. Phys. B **886** 1199 - 1222 (2014)

11. **Partial twisting for scalar mesons**
    D. Agadjanov, U. Meißner and A. Rusetsky
    J. High Energ. Phys. **2014** 103 (2014)

12. **Finite-volume corrections to the CP-odd nucleon matrix elements of the electromagnetic current from the QCD vacuum angle**
    T. Akan, F. Guo and U. Meißner
    Phys. Lett. B **736** 163 - 168 (2014)

13. **Measuring the Polarization of a Rapidly Precessing Deuteron Beam**
    Z. Bagdasarian *et al.*
    Phys. Rev. ST Accel. Beams **17** 052803 (2014)

14. **Measurement of the analysing power in proton–proton elastic scattering at small angles**
    Z. Bagdasarian *et al.*
    Phys. Lett. B **739** 152 - 156 (2014)

15. **Effective field theory calculations of $NN \to NN\pi$**
V. Baru, C. Hanhart and F. Myhrer
Int. J. Mod. Phys. E **23** 1430004 (2014)

16. **The Physics of the B Factories**
A.J. Bevan *et al.*
Eur. Phys. J. C **74** 3026 (2014)

17. **Two-loop sunset integrals at finite volume**
J. Bijnens, E. Boström and T. Lähde
J. High Energ. Phys. **2014** 19 (2014)

18. **Two-baryon systems with twisted boundary conditions**
R.A. Briceño *et al.*
Phys. Rev. D **89** 074509 (2014)

19. **Strong and radiative decays of the $D_{s0}^*(2317)$ and $D_{s1}(2460)$**
M. Cleven *et al.*
Eur. Phys. J. A **50** 149 (2014)

20. **Determination of the η'-Proton Scattering Length in Free Space**
E. Czerwiński *et al.*
Phys. Rev. Lett. **113** 062004 (2014)

21. **A study of the parity-odd nucleon-nucleon potential**
J. de Vries *et al.*
Eur. Phys. J. A **50** 108 (2014)

22. **Unraveling models of CP violation through electric dipole moments of light nuclei**
W. Dekens *et al.*
J. High Energ. Phys. **2014** 69 (2014)

23. **Direct X(3872) production in e^+e^- collisions**
A. Denig *et al.*
Phys. Lett. B **736** 221 - 225 (2014)

24. **Supernova constraints on MeV dark sectors from e+e- annihilations**
H.K. Dreiner *et al.*
Phys. Rev. D **89** 105015 (2014)

25. **Ab Initio Calculation of the Spectrum and Structure of ^{16}O**
E. Epelbaum *et al.*
Phys. Rev. Lett. **112** 102501 (2014)

26. **Sequential and simultaneous emission of particles from $p + \mathrm{Al}$ collisions at GeV energies**
M. Fidelus *et al.*
Phys. Rev. C **89** 054617 (2014)

27. **Local chiral effective field theory interactions and quantum Monte Carlo applications**
A. Gezerlis *et al.*
Phys. Rev. C **90** 054323 (2014)

28. **Low-energy neutron-deuteron reactions with N^{3}LO chiral forces**
J. Golak *et al.*
Eur. Phys. J. A **50** 177 (2014)

29. **Break-up channels in muon capture on ^{3}He**
J. Golak *et al.*
Phys. Rev. C **90** 024001 (2014)

30. **Enhanced breaking of heavy quark spin symmetry**
F. Guo, U. Meißner and C. Shen
Phys. Lett. B **738** 172 - 177 (2014)

31. **Production of Charged Heavy Quarkonium-Like States at the LHC and Tevatron**
F. Guo, U. Meißner and W. Wang
Commun. Theor. Phys. **61** 354 - 358 (2014)

32. **Production of charm-strange hadronic molecules at the LHC**
F. Guo *et al.*
J. High Energ. Phys. **2014** 138 (2014)

33. **Production of the bottom analogs and the spin partner of the X(3872) at hadron colliders**
F. Guo *et al.*
Eur. Phys. J. C **74** 3063 (2014)

34. **The electromagnetic form factors of the proton in the timelike region**
J. Haidenbauer, X. Kang and U. Meißner
Nucl. Phys. A **929** 102 - 118 (2014)

35. **Production of charmed pseudoscalar mesons in antiproton-proton annihilation**
J. Haidenbauer and G. Krein
Phys. Rev. D **89** 114003 (2014)

36. **Remarks on pole trajectories for resonances**
C. Hanhart, J.R. Pelaez and G. Rios
Phys. Lett. B **739** 375 - 382 (2014)

37. **Hadronic shift in pionic hydrogen**
M. Hennebach *et al.*
Eur. Phys. J. A **50** 190 (2014)

38. **A recoil detector for the measurement of antiproton-proton elastic scattering at angles close to 90°**
Q. Hu *et al.*
Eur. Phys. J. A **50** 156 (2014)

39. **ADC-Based Real-Time Signal Processing for the PANDA Straw Tube Tracker**
L. Jokhovets *et al.*
IEEE T. Nucl. Sci. **61** 3627 - 3634 (2014)

40. **Antinucleon-nucleon interaction in chiral effective field theory**
X. Kang, J. Haidenbauer and U. Meißner
J. High Energ. Phys. **2014** 113 (2014)

41. **B_{l4} decays and the extraction of $|V_{ub}|$**
X. Kang *et al.*
Phys. Rev. D **89** 053015 (2014)

42. **Lattice effective field theory for medium-mass nuclei**
T.A. Lähde *et al.*
Phys. Lett. B **732** 110 - 115 (2014)

43. **Dalitz plot analysis of $\eta_c \to K^+K^-\eta$ and $\eta_c \to K^+K^-\pi^0$ in two-photon interactions**
J. Lees *et al.*
Phys. Rev. D **89** 112004 (2014)

44. **Antideuteron production in $\Upsilon(nS)$ decays and in $e^+e^- \to q\bar{q}$ at $\sqrt{s} \approx 10.58$GeV**
J. Lees *et al.*
Phys. Rev. D **89** 111102 (2014)

45. **Search for the decay $\overline{B}^0 \to \Lambda_c^+ \overline{p} p \overline{p}$**
J. Lees *et al.*
Phys. Rev. D **89** 071102 (2014)

46. **Measurements of direct CP asymmetries in $B \to X_s\gamma$ decays using sum of exclusive decays**
J. Lees *et al.*
Phys. Rev. D **90** 092001 (2014)

47. **Evidence for the baryonic decay $\overline{B}^0 \to D^0\Lambda\overline{\Lambda}$**
J. Lees *et al.*
Phys. Rev. D **89** 112002 (2014)

48. **Measurement of Collins asymmetries in inclusive production of charged pion pairs in e^+e^- annihilation at BABAR**
J. Lees *et al.*
Phys. Rev. D **90** 052003 (2014)

49. **Evidence for the decay $B^0 \to \omega\omega$ and search for $B^0 \to \omega\phi$**
J. Lees *et al.*
Phys. Rev. D **89** 051101 (2014)

50. **Measurement of the $B \to X_s\ell^+\ell^-$ Branching Fraction and Search for Direct CP Violation from a Sum of Exclusive Final States**
J. Lees *et al.*
Phys. Rev. Lett. **112** 211802 (2014)

51. **Search for lepton-number violating $B^+ \to X^-\ell^+\ell'^+$ decays**
J. Lees *et al.*
Phys. Rev. D **89** 011102 (2014)

52. **Reduction of the proton radius discrepancy by 3σ**
I.T. Lorenz and U. Meißner
Phys. Lett. B **737** 57 - 59 (2014)

53. **Breaking and restoration of rotational symmetry on the lattice for bound state multiplets**
B. Lu *et al.*
Phys. Rev. D **90** 034507 (2014)

54. **Superdeformed Λ hypernuclei within relativistic mean field models**
B. Lu *et al.*
Phys. Rev. C **89** 044307 (2014)

55. **Nuclear forces and ab initio calculations of atomic nuclei**
U. Meißner
Nucl. Phys. A **928** 64 - 72 (2014)

56. **Life on earth – An accident? Chiral symmetry and the anthropic principle**
U. Meißner
Int. J. Mod. Phys. E **23** 1461005 - (2014)

57. **Generalized heavy-to-light form factors in light-cone sum rules**
U. Meißner and W. Wang
Phys. Lett. B **730** 336 - 341 (2014)

58. **$B_s \to K^{(*)}\ell\overline{\nu}$, angular analysis, S-wave contributions and V_{ub}**
U. Meißner and W. Wang
J. High Energ. Phys. **2014** 107 (2014)

59. **A method for fast feature extraction in threshold scans**
M.C. Mertens and J. Ritman
Nucl. Instr. Meth. Phys. Res. A **735** 615 - 619 (2014)

60. **Isospin effects in the exclusive $dp \to {}^3\mathrm{He}\,\pi^+\pi^-$ reaction**
M. Mielke *et al.*
Eur. Phys. J. A **50** 102 (2014)

61. **Microscopic description of octupole shape-phase transitions in light actinide and rare-earth nuclei**
K. Nomura *et al.*
Phys. Rev. C **89** 024312 (2014)

62. **Review of Particle Physics**
K.A. Olive *et al.*
Chinese Phys. C **C38** 090001 - (2014)

63. **Absence of spin dependence in the final state interaction of the View the $\vec{d}\,p \to {}^3\mathrm{He}\,\eta$ reaction**
M. Papenbrock *et al.*
Phys. Lett. B **734** 333 - 337 (2014)

64. **Finite volume effects in low-energy neutron–deuteron scattering**
A. Rokash *et al.*
J. Phys. G **41** 015105 - (2014)

65. **Photocouplings at the pole from pion photoproduction**
D. Rönchen *et al.*
Eur. Phys. J. A **50** 101 (2014)

66. **Complete set of deuteron analyzing powers for dp elastic scattering at 250-294 MeV/nucleon and the three-nucleon force**
K. Sekiguchi *et al.*
Phys. Rev. C **89** 064007 (2014)

67. **Nucleon electric dipole moments and the isovector parity- and time-reversal-odd pion–nucleon coupling**
C. Seng *et al.*
Phys. Lett. B **736** 147 - 153 (2014)

68. **Dependence and Influence of Projectile Energy and Target Mass on the Production of Light Charged Particles and Intermediate Mass Fragments in Proton Induced Reactions**
S.K. Sharma *et al.*
Nucl. Data Sheets **119** 307 - 309 (2014)

69. **Chiral Ward identities, automatic improvement and the gradient flow**
A. Shindler
Nucl. Phys. B **881** 71 - 90 (2014)

70. **The reaction $\pi N \to \pi\pi N$ in chiral effective field theory with explicit $\Delta(1232)$ degrees of freedomikp**
D. Siemens *et al.*
Phys. Rev. C **89** 065211 (2014)

71. **Stochastic Beam Cooling in the Storage Rings COSY and the future HESR with Internal Target Operation**
H. Stockhorst *et al.*
ICFA Beam Dyna. Newsl. **64** 12 (2014)

72. **2N and 3N Systems in a Three Dimensional Formalism**
K. Topolnicki *et al.*
Few-body systems **55** 835 - 838 (2014)

73. **$Y(4260)$: Hadronic molecule versus hadro-charmonium interpretation**
Q. Wang *et al.*
Phys. Rev. D **89** 034001 (2014)

74. **New experimental upper limit of the electron-proton spin-flip cross section**
C. Weidemann *et al.*
Nucl. Instr. Meth. Phys. Res. A **759** 6 - 9 (2014)

75. **Electric dipole moments of the nucleon and light nuclei**
A. Wirzba
Nucl. Phys. A **928** 116 - 127 (2014)

76. **Probing the nature of $Y(4260)$ in the isospin violating process $Y(4260) \to J/\psi\eta\pi^0$**
X. Wu *et al.*
Phys. Rev. D **89** 054038 (2014)

B.2 Conference proceedings

1. A. Adinets *et al.*
   Triplet Finder: On the Way to Triggerless Online Reconstruction with GPUs for the PANDA Experiment
   International Conference on Computational Science, Cairns, Australia: 06/10/2014 - 06/12/2014
   Procedia computer science 29 113 - 123

2. N. Alinovskiy *et al.*
   2 MeV electron cooler for COSY and HESR - first results
   5th International Particle Accelerator Conference, Dresden, Germany: 06/15/2014 - 06/20/2014
   Proceedings of IPAC 2014 765-767 (2014)

3. V. Baru *et al.*
   Non-perturbative pion dynamics for the X(3872)
   13th International Workshop on Meson Production, Properties and Interaction (MESON2014), Cracow, Poland: 05/29/2014 - 06/03/2014
   Eur. Phys. J. Web of Conferences 81 05005

4. V. Baru *et al.*
   The multiple-scattering series in few-nucleon systems
   13th International Conference on Meson-Nucleon Physics and the Structure of the Nucleon (MENU 2013), Rome, Italy: 09/30/2014 - 10/04/2014
   Eur. Phys. J. Web of Conferences 73 06005

5. A. Bussone *et al.*
   Lattice QCD Study of B-meson Decay Constants from ETMC
   8th International Workshop on the CKM Unitarity Triangle (CKM2014), Wien, Austria: 09/08/2014 - 09/12/2014
   arXiv:1411.5566

6. L. Cao and J. Ritman
   Simulations on the measurement of the D_s meson semileptonic form factor with the PANDA detector
   2nd Workshop on FAIR NExt Generation of ScientistS, Berlin, Germany: 09/16/2013 - 09/21/2013
   J. Phys.: Conf. Ser. 503 012024

7. I. Ciepal *et al.*
   Studies of the Three-Nucleon System Dynamics in the Deuteron-Proton Breakup Reaction
   25th International Nuclear Physics Conference, Florence, Italy: 06/02/2013 - 06/07/2013
   Eur. Phys. J. Web of Conferences 66 03019 -

8. I. Ciepal *et al.*
   Investigation of the Three-Nucleon System Dynamics in the Deuteron-Proton Breakup Reaction
   22nd European Conference on Few-Body Problems in Physics, EFB22, Cracow, Poland: 09/09/2013 - 09/13/2013
   Few-body systems **55** 639 - 644 (2014)

9. E. Czerwinski *et al.*
   Close to threshold η' meson production in proton-proton collisions at COSY-11
   MESON 2014, 13th International Workshop on Production, Properties and Interaction of Mesons, KRAKÓW, POLAND: 05/29/2014 - 06/03/2014
   Eur. Phys. J. Web of Conferences 81 02003

10. E. Czerwinski, P. Moskal and M. Silarski
    Study of the NNη' Production with COSY-11
    Second International Symposium on Mesic Nuclei, Cracow, Poland: 09/22/2013 - 09/25/2013

Act. Phys. Pol. B 45 739

11. D. Deermann, T. Stockmanns and J. Ritman
Characterization of the PANDA MVD Trapezoidal Silicon Strip Sensors and Their First Operation in a Proton Beam
TIPP2014, Amsterdam, The Netherlands: 06/02/2014 - 06/06/2014

12. J.E. Drut and T. Lähde
Velocity renormalization in graphene from lattice Monte Carlo
31st International Symposium on Lattice Field Theory, Mainz, Germany: 07/29/2013 - 08/03/2013
Proceedings of Science 7

13. A. Goerres *et al.*
A free-running, time-based readout method for particle detectors
Workshop on fast Cherenkov detectors - Photon detection, DIRC design and DAQ, Giessen, Germany: 09/04/2013 - 09/06/2013
J. Instrum. 9 C03025

14. J. Haidenbauer
Hyperon-Nucleon Interaction in Chiral Effective Field Theory
22nd European Conference on Few-Body Problems in Physics, (EFB22), Cracow, Poland: 09/09/2013 - 09/13/2013
Few-body systems **55** 753 - 756 (2014)

15. V. Hejny
Charge Symmetry Breaking in $dd \rightarrow {}^4\mathrm{He}\pi^0$ with WASA-at-COSY
MESON 2014 - 13th International Workshop on Production, Properties and Interaction of Mesons, Cracow, Poland: 05/29/2014 - 06/03/2014
Eur. Phys. J. Web of Conferences 81 03007

16. M. Hodana *et al.*
Study of the η-Meson Production with Polarized Proton Beam
Second International Symposium on Mesic Nuclei, Cracow, Poland: 09/22/2013 - 09/25/2013
Act. Phys. Pol. B 45 697

17. W. Krzemien *et al.*
Search for the η-mesic ${}^4\mathrm{He}$ with WASA-at-COSY
International Nuclear Physics Conference, Firenze, Italy: 06/02/2013 - 06/07/2013
Eur. Phys. J. Web of Conferences 66 09009

18. W. Krzemień *et al.*
Search for the Manifestation of the Mesic Nuclei on the $dd \rightarrow {}^3\mathrm{He}\mathrm{N}\pi$ Excitation Function Measured with WASA-at-COSY
Second International Symposium on Mesic Nuclei, Cracow, Poland: 09/22/2013 - 09/25/2013
Act. Phys. Pol. B 45 689

19. T. Lähde *et al.*
The Hoyle state in nuclear lattice effective field theory
58th DAE Symposium on Nuclear Physics, Anushakti Nagar, Mumbai, India: 12/02/2013 - 12/06/2013
Pramana 83 651 - 659

20. T. Lähde *et al.*
Lattice effective field theory for nuclei from A = 4 to A = 28

31st International Symposium on Lattice Field Theory, Mainz, Germany: 07/29/2013 - 08/03/2013
Proceedings of Science 7

21. S. Lunardi *et al.*
Tracking with Straw Tubes in the PANDA Experiment
25th International Nuclear Physics Conference, Firenze, Italy: 06/02/2013 - 06/07/2013
Eur. Phys. J. Web of Conferences 66 11007 -

22. S. Lunardi *et al.*
Nuclear lattice simulations: Status and perspectives
Eur. Phys. J. Web of Conferences **66** 01012 - (2014)

23. M. Mai, P.C. Bruns and U. Meißner
Pion photoproduction in a gauge-invariant chiral unitarity framework
Int. J. Mod. Phys. Conf. Ser. **26** 1460075 - (2014)

24. U. Meißner
Life on earth – An accident? Chiral symmetry and the anthropic principle
Seventh International Symposium on Chiral Symmetry in Hadrons and Nuclei, Beijing, China: 10/27/2013 - 10/30/2013
WORLD SCIENTIFIC, 2014. - ISBN 978-981-4618-21-2978-981-4618-22-9

25. M. Mertens *et al.*
Triplet based online track finding in the PANDA-STT
Hyperfine Interact. **229** 153 - 158 (2014)

26. P. Moskal, W. Krzemien and M. Skurzok
Search for the eta-mesic helium by means of WASA detector at COSY
the XV International Conference on Hadron Spectroscopy, Nara, Japan: 11/01/2013 - 11/30/2013
arXiv:1402.1152

27. A. Nogga
Light Hypernuclei Based on Chiral Interactions at Next-to-Leading Order
22nd European Conference on Few-Body Problems in Physics, EFB22, Cracow, Poland: 09/09/2013 - 09/13/2013
Few-body systems **55** 757 - 760 (2014)

28. E. Prencipe
Status and perspectives for $\bar{P}ANDA$ at FAIR
37th Intenational Conference of High Energy Physics, 2014, Valencia, Spanien: 07/02/2014 - 07/09/2014
arXiv:1410.5201

29. E. Prencipe and WASA-at-COSY Collaboration
Study of light mesons with WASA-at-COSY
13th International Conference on Meson-Nucleon Physics and the Structure of the Nucleon, Rome, Italy: 09/30/2013 - 10/04/2013
Eur. Phys. J. Web of Conferences 73 03012

30. A. Pyszniak *et al.*
Studies on implementation of pellet tracking in hadron physics experiments
13th International Workshop on Production, Properties and Interaction of Mesons, Cracow, Poland: 05/29/2014 - 06/03/2014
Eur. Phys. J. Web of Conferences 81 06008

31. Y. Senichev *et al.*
Spin tune parametric resonance investigation
5th International Particle Accelerator Conference, Dresden, Germany: 06/15/2014 - 06/20/2014
ISBN: 978-3-95450-132-8

32. Y. Senichev *et al.*
Spin tune decoherence in multipole fields
5th International Particle Accelerator Conference, Dresden, Germany: 06/15/2014 - 06/20/2014

33. M. Skurzok *et al.*
Search for the ^{4}He$-\eta$ bound state in $dd \to (^4\mathrm{He}-\eta)_{\mathrm{bound}} \to {}^3\mathrm{He}\,n\pi^0$ and $dd \to (^4\mathrm{He}-\eta)_{\mathrm{bound}} \to {}^3\mathrm{He}\,p\pi^-$ reactions with the WASA-at-COSY facility
13th International Workshop on Production, Properties and Interaction of Mesons, Cracow, Poland: 05/29/2014 - 06/03/2014
Eur. Phys. J. Web of Conferences 81 02020

34. H. Stockhorst *et al.*
Simulation Study of Heavy Ion Beam Injection and Acceleration in the HESR for Internal Target Experiments with Cooling
5th International Particle Accelerator Conference, Dresden, Germany: 06/15/2014 - 06/20/2014
ISBN 978-3-95450-132-8

35. H. Stockhorst *et al.*
Stochastic Cooling of a Polarized Proton Beam at COSY
International Workshop on Beam Cooling and Related Topics, Mürren, Switzerland: 06/10/2013 - 06/14/2013
ISBN 978-3-95450-140-3

36. Y.N. Uzikov and J. Haidenbauer
Spin Effects in the Interaction of Antiprotons with the Deuteron at Low and Intermediate Energies
22nd European Conference on Few-Body Problems in Physics (EFB22), Cracow, Poland: 09/09/2013 - 09/13/2013

37. Y.N. Uzikov and J. Haidenbauer
Spin dependence of the interaction of antiprotons with the deuteron
20th International Symposium on Spin Physics (SPIN 2012), Dubna, Russia: 09/17/2012 - 09/22/2012
Phys. Part. Nuclei 45 196 - 198

38. P. Wintz and PANDA tracking group
The central straw tube tracker in the PANDA experiment
Hyperfine Interact. **229** 147 - 152 (2014)

39. A.A. Filin *et al.*
Complete next-to-next-to-leading order calculation of $NN \to NN\pi$ in chiral effective field theory
13th International Workshop on Meson Production, Properties and Interaction, MESON2014, Cracow, Poland: 05/29/2014 - 06/03/2014
Eur. Phys. J. Web of Conferences 81, 03003

40. M. Zurek and M. Albrow
Central Exclusive $\pi^+\pi^-$ Production in $p\bar{p}$ Collisions at $\sqrt{s} = 0.9$ and 1.96 TeV at the Tevatron
13th International Workshop on Production, Properties and Interaction of Mesons, Cracow, Poland: 05/29/2014 - 06/03/2014
Eur. Phys. J. Web of Conferences 81 04013

C Talks and Colloquia

C.1 Conference talks (invited)

1. J. de Vries
   Electric dipole moments of complex systems
   Quark confinement and the hadron spectrum IX, St. Petersburg, Russia: 09/08/2014 - 09/12/2014

2. J. de Vries
   The theory of electric dipole moments: a motivation for JEDI
   10-year Anniversary of German-Georgian Science Bridge, Tbilisi, Georgia: 07/07/2014 - 07/12/2014

3. D. Grzonka
   Xi Production in Low Energy Antiproton Annihilation
   Strangeness production in stopped antiproton annihilation, Satellite workshop at SMI, Wien, Austria: 09/20/2014

4. D. Grzonka
   Search for polarization effects in the antiproton production process
   II International Symposium on Applied Nuclear Physics and Innovative Technologies, Collegium Maius, Jagiellonian University, Kraków, Poland: 09/24/2014 - 09/27/2014

5. D. Grzonka
   Hadron physics with WASA at AD/CERN
   ADUC/ELENA Meeting, CERN, Geneva, Switzerland: 01/14/2014 - 01/15/2014

6. D. Grzonka
   Science Funding in Europe: "HORIZON 2020"
   6th Georgian-German School and Workshop in Basic Science, Tblisi, Georgia: 07/07/2014 - 07/12/2014

7. J. Haidenbauer
   Baryon-baryon interaction in chiral effective field theory
   International School for Strangeness Nuclear Physics, Sendai, Japan: 01/13/2014 - 01/19/2014

8. J. Haidenbauer
   Hyperon-nucleon interactions from chiral EFT
   Hadrons from Quarks and Gluons, hirschegg, austria: 01/12/2014 - 01/18/2014

9. J. Haidenbauer
   Hyperon-nucleon interaction
   Workshop on "Perspectives of high resolution spectroscopy at Jefferson Lab", Newport News, USA: 05/27/2014 - 05/29/2014

10. J. Haidenbauer
    Baryon-baryon interactions in chiral effective field theory
    Workshop on "Bound states and resonances in effective field theory and lattice QCD calculations", Benasque, Spain: 07/21/2014 - 07/31/2014

11. J. Haidenbauer
    Nucleon-Nucleon and Hyperon-Nucleon Interactions
    26th Indian-Summer School & SPHERE School of Physics, Prague, Czech Republic: 09/03/2014 - 09/07/2014

12. C. Hanhart
Dispersion theory to connect $\eta \to \pi\pi\gamma$ to $\eta \to \gamma^*\gamma$
Workshop on light meson dynamics, Mainz, Germany: 02/10/2014 - 02/12/2014

13. C. Hanhart
gamma gamma physics (theory)
Hadronic contributions to the muon anomalous magnetic moment: strategies for improvements of the accuracy of the theoretical prediction, Mainz, Germany: 04/01/2014 - 04/05/2014

14. C. Hanhart
Form Factors for $B \to \pi\pi\ell\nu$
Lattice meets continuum, Siegen, Germany: 09/29/2014 - 10/02/2014

15. V. Hejny
Charge Symmetry Breaking in $dd \to {}^4\mathrm{He}\,\pi^0$ with WASA-at-COSY
13th International Workshop on Meson Production, Properties and Interaction, Cracow, Poland: 05/29/2014 - 06/03/2014

16. A. Lehrach
Storage Ring Based EDM Search - Achievements and Goals
21st International Symposium on Spin Physics, Beijing, China: 10/20/2014 - 10/24/2014

17. A. Lehrach
Beam and spin dynamics at hadron storage rings
9th International Conference in Charged Particle Optics, Brno, Czech Republic: 08/31/2014 - 09/05/2014

18. S. Liebig
Light hypernuclei in a no-core shell model approach
CRC 110 Collaboration Meeting, Weihai, China: 07/25/2014 - 07/29/2014

19. T. Luu
Hyper-Nuclei and other things from Lattice QCD
CRC 110 Workshop, Weihai, China: 07/25/2014 - 07/30/2014

20. A. Nogga
Theory of three-nucleon forces
6th Georgian-German School and Workshop in Basic Science, Tbilisi, Georgia: 07/07/2014 - 07/12/2014

21. A. Nogga
Few-Body Hypernuclei
Workshop on hypernuclear physics “Perspectives of high resolution hypernuclear spectroscopy at Jlab”, Newport News, VA, USA: 05/27/2014 - 05/29/2014

22. E. Prencipe
Search for exotic charmonium states
Heavy Quarks and Leptons conference, Mainz, Germany: 08/25/2014 - 08/29/2014
arXiv:1411.0720

23. F. Rathmann
Search for Electric Dipole Moments in Storage Rings
Niccolò Cabeo School 2014 Vacuum and broken symmetries: from the quantum to the cosmos, Ferrara, Italy:

05/25/2014 - 05/29/2014

24. J. Ritman
Ramping up PANDA for First Physics with Antiprotons at FAIR
Combined Meeting of the FAIR and GSI Science Councils, Darmstadt, Germany: 10/23/2014

25. J. Ritman
Using Antiprotons for High Precision Studies of Hadrons
International Conference on Science and Technology for FAIR in Europe 2014, Worms, Germany: 10/13/2014 - 10/17/2014

26. J. Ritman
The PANDA Experiment: a facility to map out exotic and charmed hadrons
Second International Symposium on applied nuclear physics and innovative technologies in Krakow, Cracow, Poland: 09/24/2014

27. S. Schadmand
Dalitz decay of the omega meson
CLAS collaboration meeting - HSWG, Jefferson Lab, USA: 03/05/2014 - 03/08/2014

28. V. Serdyuk and PANDA-Kollaboration
The PANDA Central Straw Tracker
STORI14 9th International Conference on Nuclear Physics at Storage Rings, Sankt Goar, Germany: 09/28/2014 - 10/03/2014

29. T. Stockmanns
HPC Computing at the PANDA Experiment
HIC for FAIR Physics Day: HPC Computing, Frankfurt Institute for Advanced Studies, FIAS, Germany: 11/11/2015

30. A. Wirzba
Electric dipole moment of the nucleon and light nuclei
Hadrons from Quarks and Gluons, International Workshop XLII on Gross Properties of Nuclei and Nuclear Excitations, Hirschegg, Austria: 01/12/2014 - 01/18/2014

31. A. Wirzba
Two Lectures on Low-energy consequences of physics beyond the Standard Model with special emphasis on electric dipole moments
Graduiertenkolleg School 2014: Particle and Astro-particle Physics in the Light of LHC, Bad Honnef, Germany: 08/25/2014 - 08/29/2014

32. A. Wirzba
Dispersive approach to the eta transition form factor
MesonNet Meeting, Frascati, Italy: 09/29/2014 - 10/01/2014

33. M. Zurek
Investigations of the charge symmetry breaking reaction $dd \rightarrow {}^4\mathrm{He}\,\pi^0$ with the WASA-at-COSY
MesonNet 2014 International Workshop, Frascati, Italy: 09/29/2014 - 10/01/2014

C.2 Conference contributions

1. L. Bianchi
   Combination of message queues and GPUs for the event building of the PANDA experiment.
   GPU Computing at High Energy Physics Conference, Pisa University, Italy: 09/11/2014

2. L. Bianchi
   Combination of message queues and GPUs for the event building of the PANDA experiment.
   International Conference on Science and Technology for FAIR in Europe 2014, Worms, Germany: 10/13/2014 - 10/17/2014

3. J. Bsaisou
   EDMs of Light Nuclei in Chiral Effective Field Theory
   DPG-Frühjahrstagung (Hadronen und Kerne), Frankfurt, Germany: 03/17/2014 - 03/21/2014

4. L. Cao, J. Ritman and PANDA Collaboration
   Simulations of the Measurement of the Form Factor for the D_s Semileptonic Decay with the PANDA Detector
   DPG-Frühjahrstagung, Frankfurt, Germany: 03/17/2014 - 03/21/2014

5. L. Cao, J. Ritman and PANDA Collaboration
   Simulated Measurements of the D_s Semileptonic Decay Form Factor with the PANDA Detector
   the 37th International Conference on High Energy Physics (ICHEP), Valencia, Spain: 07/02/2014 - 07/09/2014

6. J.R. de Elvira *et al.*
   Roy–Steiner equations for πN scattering
   Seventh International Symposium on Chiral Symmetry in Hadrons and Nuclei, Beijing, China: 10/27/2013 - 10/30/2013

7. D. Deermann, T. Stockmanns and J. Ritman
   Characterization of the PANDA MVD Trapezoidal Silicon Strip Sensors and Their First Operation in a Proton Beam
   TIPP2014, Amsterdam, The Netherlands: 06/02/2014 - 06/06/2014

8. D. Deermann, T. Stockmanns and J. Ritman
   Characterization of the PANDA MVD Trapezoidal Silicon Strip Sensors and the Development of their Readout System
   DPG Frühjahrstagung, Frankfurt, Germany: 03/17/2014 - 03/21/2014

9. S. Esch, T. Stockmanns and J. Ritman
   The Influence of Additional Semiconductor Discs on the Reconstruction of $\overline{\Lambda}\Lambda$ in the PANDA Experiment
   DPG Frühjahrstagung, Frankfurt, Germany: 03/17/2014 - 03/21/2014

10. A. Goerres
    Time-Based Silicon Strip Readout ASIC for the PANDA Detector at FAIR
    FEE 2014, Argonne National Laboratory, Lemont, IL 60439, USA: 05/20/2014 - 05/23/2014

11. A. Goerres *et al.*
    The PASTA Chip - A Free-Running Readout ASIC for Silicon Strip Sensors in PANDA
    DPG-Frühjahrstagung, Frankfurt, Germany: 03/17/2014 - 03/21/2014

12. D. Gotta
Ultimate Precision X-ray Spectroscopy of Hadronic Atoms
Sixth Georgian-German School and Workshop in Basic Science, Tbilisi, Georgien: 06/06/2014

13. D. Gotta
Pionic Hydrogen and Friends
International Conference on Exotic Atoms, Vienna, Austria: 09/15/2014 - 09/19/2014

14. B. Gou
Initial Research of np Scattering with Polarized Deuterium Target at ANKE/COSY 25'
The 21st International Symposium on Spin Physics (Spin2014), Peking University, Beijing, China: 10/20/2014 - 10/24/2014

15. J. Haidenbauer
Hyperon-nucleon interaction in chiral effective field theory
International Conference on Particles and Nuclei (PANIC 2014), Hamburg, Germany: 08/24/2014 - 08/29/2014

16. F. Hauenstein
Spin Triplet $p\Lambda$ Scattering Length and Polarization Observables in the $pp \to pK\Lambda$ Reaction
ECT* Workshop on Achievements and Perspectives in Low-Energy QCD with Strangeness, Trento, Italy: 10/27/2014 - 10/31/2014

17. F. Hauenstein and COSY-TOF Collaboration
Determination of the $p\Lambda$ Scattering Length from the Reaction $\overrightarrow{p}p \to pK^+\Lambda$
DPG Frühjahrstagung, Frankfurt, Germany: 03/17/2014 - 03/21/2014

18. V. Hejny
Measurements of Electric Dipole Moments of Charged Particles at Storage Rings
Particles and Nuclei International Conference 2014, Hamburg, Germany: 08/24/2014 - 08/29/2014

19. A. Herten
Enabling the Next Generation of Particle Physics Experiments: GPUs for Online Track Reconstruction
GPU Technology Conference 2014, San Jose, USA: 04/26/2014

20. A. Herten
Online Tracking on GPUs at PANDA
Fifth International Workshop for Future Challenges in Tracking and Trigger Concepts 2014, Frankfurt, Germany: 05/13/2014

21. A. Herten
Enabling the Next Generation of Particle Physics Experiments: GPUs for Online Track Reconstruction
Workshop on Fast Data Processing on GPUs, CUDA Center of Excellence, TU Dresden, Germany: 05/15/2014

22. A. Herten
Online Tracking on Graphics Processing Units for PANDA
PhD Students Poster Session, Ruhr-Universität Bochum, Germany: 06/13/2014

23. A. Herten
GPU-based Online Tracking for the PANDA Experiment
GPU Computing at High Energy Physics Conference, Pisa University, Italy: 09/11/2014

24. A. Herten
GPU-based Online Tracking for the PANDA Experiment
2nd Annual Workshop of the NVIDIA Application Lab Workshop 2014, Supercomputing Centre Jülich, Germany: 10/08/2014

25. A. Herten *et al.*
GPU Implementations of Online Track Finding Algorithms at PANDA
DPG Frühjahrstagung, Frankfurt, Germany: 03/17/2014 - 03/21/2014

26. Q. Hu, H. Xu and J. Ritman
Performance Test and Commissioning of Recoil Detector of HESR Day-One Experiment
DPG Frühjahrstagung, Frankfurt, Germany: 03/17/2014 - 03/21/2014

27. S. Jowzaee
ΣN cusp effect and angular distributions in the the CMS frame in the $pp \to pK^+\Lambda$ reaction
DPG-Frühjahrstagung, Frankfurt, Germany: 03/17/2014 - 03/21/2014

28. S. Leiber, J. Ritman and P. Wintz
The electronic readout of the PANDA Straw Tube Tracker
DPG-Frühjahrstagung, Frankfurt, Germany: 03/17/2014 - 03/21/2014

29. T. Luu
Few-body Physics from Lattice QCD
XIth Quark Confinement and the Hadron Spectrum, St. Petersburg, Russia: 09/08/2014 - 09/12/2014

30. S. Mey
An RF E×B Dipole for Spin Manipulation at COSY - Prototype Commissioning and First Measurements
DPG-Frühjahrstagung der Sektion Kondensierte Materie, Dresden, Germany: 03/30/2014 - 04/04/2014

31. S. Mey
A Novel RF-ExB Spin Manipulator at COSY
6th Georgian-German School and Workshop in Basic Science, Tblisi, Georgia: 07/07/2014 - 07/12/2014

32. P. Moskal
Few-body aspects of the near threshold pseudoscalar meson production
22nd European Conference on Few Body Problems in Physics, Cracow, Poland: 09/09/2013 - 09/13/2013

33. E. Prencipe
Search for exotics at BABAR
Particles and Nuclei International Conference 2014, Hamburg, Germany: 08/25/2014 - 08/29/2014
arXiv:1411.0571

34. E. Prencipe
Search for exotics at BABAR
ICNPF, FAIR Workshop, Kolymbari, Greece: 07/29/2014 - 07/29/2014

35. E. Prencipe
Search for exotics in the rare decay $B \to J/\psi KKK$ at BABAR
3rd International Conference on New Frontiers in Physics, Kreta, Griechenland: 07/28/2014 - 08/06/2014
arXiv:1410.5657

36. E. Prencipe and PANDA Collaboration
Perspectives of Open Charm Physics at $\bar{P}ANDA$
3rd International Conference on New Frontiers in Physics, Kreta, Griechenland: 07/28/2014 - 08/06/2014
arXiv:1410.5680

37. E. Prencipe and PANDA Collaboration
Perspectives of Open Charm Physics at $\bar{P}ANDA$
Hirschegg 2014, Hadrons from Quarks and Gluons, Hirschegg, Kleinwalsertal, Austria: 01/12/2014 - 01/18/2014

38. E. Prencipe and PANDA Collaboration
Perspectives on Open Charm Physics with $\bar{P}ANDA$
DPG Frühjahrstagung, Frankfurt, Germany: 03/17/2014 - 03/21/2014

39. E. Prencipe and PANDA Collaboration
Search for hybrids at BABAR: study of the rare decays $B \to J/\psi KKK$, and search for $B0 \to J/\psi\phi$.
DPG Frühjahrstagung, Frankfurt, Germany: 03/17/2014 - 03/21/2014

40. A. Shindler
Beyond the Standard Model Matrix Elements with the gradient flow
The XXXII International Symposium on Lattice Field Theory, New York, USA: 06/23/2014 - 06/28/2014

41. A. Shindler
Beyond the Standard Model Matrix Elements with the gradient flow
XI Quark confinement and the hadron spectrum, Saint Petersburg, Russia: 09/08/2014 - 09/12/2014

42. H. Stockhorst *et al.*
Stochastic Cooling of a Polarized Proton Beam at COSY
International Workshop on Beam Cooling and Related Topics, Mürren, Switzerland: 06/10/2013 - 06/14/2013

43. A. Wirzba
Electric dipole moments of the nucleon and light nuclei
XLV. Arbeitstreffen Kernphysik in Schleching, Schleching, Germany: 02/20/2014 - 02/27/2014

44. A. Wirzba
Theory IV: Physics beyond the Standard Model
Hadron Physics Summer School 2014, Schloss Rauischholzhausen, Germany: 09/01/2014 - 09/05/2014

45. H. Xu
The status of Day-1 Experiment at HESR
ICNFP2014 - The 3rd International Conference on New Frontiers in Physics, Crete, Greece: 07/28/2014 - 08/06/2014

46. A. Zink *et al.*
Ein DIRC Demonstrationsdetektor für das WASA-at-COSY und PANDA Experiment
DPG Frühjahrstagung, Frankfurt, Germany: 03/17/2014 - 03/21/2014

47. M. Zurek
Exclusive Central Meson Production in Proton Antiproton Collisions at the Tevatron at $\sqrt{s}$ = 1960 GeV and 900 GeV
13th International Workshop on Production, Properties and Interaction of Mesons, Cracow, Poland: 05/29/2014 - 06/03/2014

48. M. Zurek
Exclusive Central Meson Production in Proton Antiproton Collisions at the Tevatron at $\sqrt{s}$ = 1960 GeV and 900 GeV
International Workshop on Diffraction in High-Energy Physics, Primosten, Croatia: 09/10/2014 - 09/17/2014

C.3 Talks (non-conference)

1. J. Bsaisou
EDMs of Light Nuclei in Chiral Effective Field Theory
PhD Thesis Defense, Bonn, Germany: 04/25/2014

2. L. Cao
Simulations on the Measurement of the D_s semileptonic form factor with the PANDA Detector
32nd CANU, 9th JCHP-FFE Workshop and 1st CBAC-Meeting, Bad Honnef, Germany: 12/15/2014 - 12/16/2014

3. J. de Vries
Hadronic and nuclear parity violation in chiral effective field theory
Technical University Munich: 04/17/2014

4. J. de Vries
Hadronic parity violation in chiral effective field theory
University of Bonn

5. A. Goswami
Analysis of the $pp \to pp\eta$ data set from the WASA-at-COSY campaign
32nd CANU, 9th JCHP-FFE Workshop and 1st CBAC-Meeting, Bad Honnef, Germany: 12/15/2014 - 12/16/2014

6. M. Hartmann
Workshop on J-PARC Hadron Physics,"Cosy-Experiments: A general overview and selected results"
Shirakata, Tokai Ibaraki 319-1106, Japan: 02/10/2014 - 02/12/2014

7. S. Jowzaee
Results on hyperon production at COSY-TOF
32nd CANU, 9th JCHP-FFE Workshop and 1st CBAC-Meeting, Bad Honnef, Germany: 12/15/2014 - 12/16/2014

8. A. Kacharava
21th International Symposium on Spin2014
Bijing, China: 10/20/2014 - 10/24/2014

9. T. Luu
Simulating Carbon Nano-Structures with Lattice Methods
Dublin, Ireland: 04/02/2014

10. K. Pysz
Readout system for high spatial and energy resolution of PANDA Central Tracker
32nd CANU, 9th JCHP-FFE Workshop and 1st CBAC-Meeting, Bad Honnef, Germany: 12/15/2014 - 12/16/2014

11. F. Rathmann
Search for Permanent Electric Dipole Moments (Proposal for the 1st half of 2015)
CBAC Meeting, Bad Honnef, Germany: 12/15/2014 - 12/16/2014

12. J. Ritman
The PANDA Experiment: a facility to map out exotic and charmed hadrons
Kolloquiumsvortrag, Newport News, USA: 04/25/2014

13. J. Ritman
IKP in transition from using COSY as a precision machine for hadron physics to preparing the HESR and FAIR experiments as well as exploring the potential for a storage ring EDM search
32nd CANU, 9th JCHP-FFE Workshop and 1st CBAC-Meeting, Bad Honnef, Germany: 12/15/2014 - 12/16/2014

14. J. Ritman
Investigating the properties and interactions of (exotic) charmed hadrons with antiproton annihilation experiments
Budapest, Hungary: 04/29/2014

15. A. Shindler
Chiral Ward identities, automatic O(a) improvement and the gradient flow
CERN, Switzerland

16. A. Shindler
B-physics from lattice QCD...with a twist
CERN, Switzerland

17. A. Shindler
Chiral Ward identities, automatic O(a) improvement and the gradient flow
DESY-Zeuthen, GERMANY

18. A. Shindler
Chiral symmetry, Wilson twisted mass and the gradient flow
Frankfurt, Germany

19. H. Stockhorst, R. Stassen and T. Katayama
Stochastic Beam Cooling in the HESRand Benchmarking Experiments at COSY
32nd CANU, 9th JCHP-FFE Workshop and 1st CBAC-Meeting, Bad Honnef, Germany: 12/15/2014 - 12/16/2014

20. P. Wintz
PANDA STT
32nd CANU, 9th JCHP-FFE Workshop and 1st CBAC-Meeting, Bad Honnef, Germany: 12/15/2014 - 12/16/2014

21. A. Wirzba
Lecture of the Theory of Electric Dipole Moments
JEDI collaboration meeting, Jülich, Germany: 03/06/2014

22. H. Xu
KOALA Experiment
32nd CANU, 9th JCHP-FFE Workshop and 1st CBAC-Meeting, Bad Honnef, Germany: 12/15/2014 - 12/16/2014

D Diploma and Ph.D. Theses

1. Bachelor, Master, Diploma

1. T. Dato
   Bachelor Thesis: Is the η double off-shell form factor separable?
   Rheinische Friedrich-Wlihelms-Universität Bonn, Germany

2. Y. Emonds
   Bachelor Thesis: Parametrisierung von Pion-Formfaktoren
   Rheinische Friedrich-Wlihelms-Universität Bonn, Germany

3. S. Henssler
   Master Thesis: Entwicklung und Evaluierung eines Verfahrens für kinematische Anpassung von Teilchenreaktionenbasierend auf dem Verfahren von Nelder und Mead
   FH Aachen, Campus Jülich, Fachbereich 9:Medizintechnic und Technomathematik, Germany

4. A. Kopp
   Bachelor Thesis: Accelerating the numerical solution of linear systems arising from the numerical simulation of the physical properties of graphene and carbon nanotubes.
   FH Aachen, Campus Jülich, Department 9: Medical Engineering and Technomathematics, Germany

2. Ph.D.

5. J. Bsaisou
   Electric Dipole Moments of Light Nuclei in Chiral Effective Field Theory
   Rheinische Friedrich-Wilhelms-Universität Bonn, Germany

6. S. Esch
   Evaluation of the PANDA Silicon Pixel Front-End Electronics and Investigation of the Lambda bar Lambda Final State
   Ruhr-Universität Bochum, Germany

7. F. Hauenstein
   Proton-Lambda Final State Interaction and Polarization ObservablesMeasured in the $pp \to pK\Lambda$ Reaction at 2.7 GeV/c Beam Momentum
   Friedrich-Alexander-Universität Erlangen-Nürnberg, Germany

8. A. Ivanov
   Nonlinear matrix integration of spin-orbital dynamics of charged particles.
   Saint Petersburg State University, Russia

9. S. Jowzaee
   Self-Supporting straw tube detector for the PANDA and COSY-TOF experiments
   Jagiellonen-Universität Krakau, Polen

10. X. Kang
    Chiral dynamics and final state interactions in semileptonic B meson decay and antinucleon-nucleon scattering
    Rheinische Friedrich-Wilhelms-Universität Bonn, Germany

11. D. Lersch
    Investigation of Dipion Final State Interactions in $pp \to pp\eta[\eta \to \pi^+\pi^-\gamma]$ with the WASA-at-COSY Facility
    Bergische Universität Wuppertal, Germany

12. M. Mielke
    Multi-pion production in deuteron-proton collisions at COSY-ANKE.
    Universität Münster, Germany

13. D. Rönchen
    Baryon resonances in pion- and photon-induced hadronic reactions
    Rheinische Friedrich-Wlihelms-Universität Bonn, Germany

14. D. Zyuzin
    Theoretical study of spin dynamics in a storage ring for the detection of the electric dipole moment.
    Saint Petersburg State University, Russia

E Awards & Offers for Professorships

M. Bai: Director of IKP-4, since Dec. 2014

R. Maier: JARA-Seniorprofessor, RWTH-Aachen und Forschungszentrum Jülich GmbH, 30.01.2015

R. Maier: Honorary doctor of Joint Institute for Nuclear Research (Dubna, Russia)

U.-G. Meißner: Editorial Board of EPJA, Managing Editor—Reviews

J. Ritman: Re-elected as spokesperson of the PANDA collaboration, 2014

R. Stassen Encouraging Prize 'Development and Start-up of the Stochastic Cooling System for Nuclotron Ion Beams at the NICA Accelerator Complex' of the Joint Institute of Nuclear Research (Dubna, Russia)

H. Ströher: Editorial Board of EPJA, Co-Editor

H. Ströher: Honorary doctor of Georgian Technical University

F Funded Projects

Project	Responsible	Funded by
HadronPhysics3-Support (Access)	D. Grzonka	EU-Projekt
HadronPhysics3-Coordination (MesonNet)	D. Grzonka	EU-Projekt
HadronPhysics3-RTD	F. Goldenbaum	EU-Projekt
Straw Tube Tracker	J. Ritman	Industrieprojekt mit GSI
Micro Vertex Detector	J. Ritman	Industrieprojekt mit GSI
POLPBAR Management	H. Ströher	EU-Projekt
POLPBAR Research	H. Ströher	EU-Projekt
HadronPhysics3 - RTD	M. Büscher	EU-Projekt
HadronPhysics3 - RTD	F. Rathmann	EU-Projekt
HGF - Fellow Award C.Roberts Preisgeld	U. Meißner	HGF
HadronPhysics3 - Coordination (EPOS)	C. Hanhart	EU-Projekt
HadronPhysics3 - Coordination (ENC-study)	A. Lehrach	EU-Projekt
HESR -coordination	R. Toelle	Industrieprojekt mit FAIR GmbH
HESR -sonstige Magnete	U. Bechstedt	Industrieprojekt mit FAIR GmbH
HESR -Netzgeräte	M. Retzlaff	Industrieprojekt mit FAIR GmbH
HESR -Hochfrequenz	R. Stassen	Industrieprojekt mit FAIR GmbH
HESR -Injektion	R. Toelle	Industrieprojekt mit FAIR GmbH
HESR -Strahldiagnose	V. Kamerdzhiev	Industrieprojekt mit FAIR GmbH
HESR -Vakuum	F. Esser	Industrieprojekt mit FAIR GmbH
HESR -Stochastische Kühlung	R. Stassen	Industrieprojekt mit FAIR GmbH
HESR -Panda-Integration	D. Prasuhn	Industrieprojekt mit FAIR GmbH
SFB/TRR 110 Quantenchromodynamik TP A01	U. Meißner	SFB
SFB/TRR 110 Quantenchromodynamik TP B03	U. Meißner	SFB
SFB/TRR 110 Quantenchromodynamik TP B07	U. Meißner	SFB
SFB/TRR 110 Quantenchromodynamik TP Z01	U. Meißner	SFB

G JCHP-FFE-Projects

Responsible	Institute	Project
PD Dr. A. Khoukaz	Westfälische Wilhelms-Universität Münster	Mesonenproduktion in Nukleon-Nukleon- und Nukleon-Kern-Stößen an COSY
Prof. Dr. A. Vasilyev	PNPI Gatchina	Development, commissioning and operation of components for the COSY Experiments WASA and ANKE and spin-filtering studies at COSY as preparation for PAX at FAIR
Prof. Dr. S. Vorobyev	PNPI Gatchina	The pn-reaction studies using the ANKE silicon tracking telescopes
Prof. Dr. B. Kämpfer	Forschungszentrum Dresden-Rossendorf	Weiterentwicklung des STT Software Pakets von ANKE zum Einsatz in zukünftigen Experimenten
Prof. Dr. M. Nioradze	Tbilisi State University	NN-elastic scattering studies at COSY
Prof. Dr. O. Willi	Universität Düsseldorf	Measurements of the degree of polarization of laser accelerated protons
PD M. Jezabek	Polish Academy of Sciences	Development of the signal processing method for high performance PANDA STT
Prof. Dr. T. Weis	TU Dortmund	Development of a Fast Orbit Feedback System for the HESR and Beam Tests at COSY
Prof. Dr. P. Moskal	Jagellonian University Krakow	η meson production with polarized proton beam
Prof. T. Johansson	Uppsala University	Study of the $\omega \rightarrow \pi^+\pi^-\pi^0$ Dalitz plot distribution with WASA
Prof. A. Roy	Indian Institute of Technology Indore, India	ω Meson Decays with WASA-at-COSY
PD Dr. D. Eversheim	HISKP Universität Bonn	Time Reversal Invariance Test at COSY (TRIC)
Prof. N. Nikolaev	L.D. Landau Institute Moscow, Russia	Numerical simulations of spin dynamics for JEDI experiments, searching for permanent Electric Dipole Moments of deuterons and protons at COSY
Dr. J. G. Messchendorp	University of Groningen, Kernfysisch Versneller Instituut, Netherlands	Momentum Dependent electron Reconstruction for WASA and the PANDA Pre-Assembly
Prof. R. Varma	Indian Institute of Technology Indore, India	High statistics experiment for omega meson decays with WASA-at-COSY
Prof. A. Roy	Indian Institute of Technology Indore, India	The η meson decay into $\gamma\gamma^*$ in pp reactions with WASA-at-COSY
Prof. Dr. H. Clement	Universität Tübingen	Analysis of $\eta\rho$ Scattering and Two-Pion-Production Data with Respect to ABC Effect and its Associated Resonance in the Two-Baryon-System

Prof. Dr. P. Moskal	Jagellonian University Krakow	Analysis of hyperon production with polarized proton beam
Prof. Dr. H. Clement	Universität Tübingen	Installation of a DIRC-Prototyp Detector for PANDA and Experiments with WASA-at-COSY
Prof. Dr. W. Eyrich	Universität Erlangen-Nürnberg	Experimente an TOF und WASA an COSY
Prof. A. Gerasimov	ITEP Moscow	Development of a Frozen-Pellet Target
Prof. Dr. W. Kühn	Universität Giessen	Realtime Tracking for the PANDA Target Spectrometer
Dr. P. Lenisa	Università degli Studi di Ferrara, Italy	Spin-filtering studies in storage rings
Dr. A. Kulikov	JINR Dubna, Moscow Region, Russia	Spin Experiments at ANKE
Prof. J. Wang	Chinese Academy of Sciences, Lanzhou, China	Commissioning of the HESR day one experiment at COSY
Prof. Dr. A. Schäfer	Universität Regensburg	Mesonen Distributions-Amplituden
Prof. Dr. U. Wiedner	Ruhr-Universität Bochum	Development for the forward endcap of the PANDA EMC and buildup of the final endcap within PANDA in Jülich
Prof. Dr. U. Wiedner	Ruhr-Universität Bochum	Development of the Cryogenic Supply System for tests of the PANDA Target Spectrometer Solenoid
Prof. Dr. K. Brinkmann	Justus-Liebig-Universität Gießen	Development and Validation of a Free-Running Silicon-Strip Front-End ASIC for the PANDA MVD
Prof. H. Chen	Southwest University, School of Physical Science and Technology, China	Simulation and optimization of the PANDA detector to measure the form factor of the $Ds \rightarrow e^{+}\nu^{+}\pi,\eta,\eta`$decay
Dr. P. Lenisa	Università degli Studi di Ferrara, Italy	Spin-tracking studies in storage rings
Prof. U. Wiedner	Ruhr-Universität Bochum	Entwicklung für das Slow-control-System von PANDA

H Conferences (co-)organized by the IKP

H.1 6^{th} Georgian–German School and Workshop in Basic Science

Within the framework of "Georgian–German Science Bridge" (GGSB), institutes of Forschungszentrum Jülich (FZJ) – IKP, IEK, INM, JCNS and ZEA – together with its Georgian partners institutions, the Ivane Javakishvili Tbilisi State University (TSU) and the Georgian Technical University (GTU) are strengthening the scientific, technological and educational cooperation between the two countries. The sixth bi–annual meeting called "Georgian-German School and Workshop in Basic Science" (GGSWBS'14) took place in Tbilisi from July 7 to 12, 2014 (see: http://collaborations.fz-juelich.de/ikp/cgswhp/cgswhp14/). The meeting has also been published in 2014 as "Schriften des Forschungszentrums Jülich, Reihe Schlüsseltechnologien/Key Technologies, Band/Volume 91 (Eds.: A. Kacharava, K. Kotetishvili, H. Ströher)".
The workshop and school focused on the following topics:

- Precision experiments (with hadronic probes)
- Condensed matter physics (with photon and neutron probes)
- Atmospheric sciences (chemistry and models)
- Medical applications (imaging)
- Engineering sciences (simulation and instrumentation)
- Poster sessions of students and topical lectures

Fig. 63: Participants of the workshop.

At the same time it was the anniversary meeting – "Ten Years of GGSB" –in which achievements in the scientific and technological cooperation between the two countries were summarized. In addition discussions and brainstormings about ongoing and future scientific projects were conducted and educational programs (in particular student exchanges) were fostered. The cooperation of Jülich and the Georgian partners has been put on solid ground by a Memorandum–of–Understanding (MoU) and a student exchange program with the Shota Rustaveli National Science Foundation (SRNSF), and students have started Master- and PhD-thesis studies in different FZJ–institutes (Joint Call Georgia-Jülich). The ministry of Education and Science of Georgia (MoE) and FZ–Jülich have agreed to support and further develop the long-term scientific and educational cooperation between a consortium of Georgian Universities and Institutes of FZJ.
For October 2015, it is planned to continue dedicated lecture courses for Bachelor, Master and PhD students in various fields of basic sciences: the so called "Autumn Lectures" will comprise introductory courses in experimental and theoretical physics with emphasis on nuclear, high energy and medical physics as well as frontier technologies together with their applications. A special focus will be laid on practical exercises in laboratories.

H.2 CRC 110 workshop, Weihai, China

Fig. 64: Participants of the CRC 110 workshop.

The general meeting of the CRC 110 took place in Weihai, China, from July 25 to July 29, 2014. The meeting place was the Shangdong University Academic Center Hotel, next to Weihai's International Beach. The meeting consisted of talks by german students and post-docs on the status of the various projects, a midterm review of the contribution form the Chinese PIs and talks from prospective new PIs for the second funding period (FP 2) as well as associates of the CRC. Also, a road map for FP 2 was worked out and a meeting of the board of the CRC took place. From the Chinese side of the CRC, we had 9 PIs, 4 post-docs and 24 students participating. From the German side, there were 9 PIs, 9 post-docs and 10 students. Various associates of the CRC, Chinese reviewers, invited guests as well as NSFC representatives were also present. In total we had 56 Chinese and 32 German

participants. There was ample time for discussion and recreation on the beach.

H.3 Hadron Physics Summer School (HPSS2014)

The Hadron Physics Summer School HPSS2014 took place from September 1 to September 5, 2014, at the conference venue Schloss Rauischholzhausen of the University of Gießen. The HPSS2014 is the continuation of a biannual series of summer school that started in 2002.

More than 40 graduate and advanced undergraduate students from 11 countries and 3 continents participated in the summer school. This school consisted of lectures and working groups on theoretical, experimental and accelerator aspects. The focus was on current issues in hadron physics with emphasis on the latest programs at the accelerators COSY and ELSA (Bonn), also featuring future projects like HESR/PANDA at FAIR, PAX and the search for electric dipole moments of charged particles in storage rings (JEDI) as well as Laser-induced particle acceleration (JuSPARC).

The HPSS2014 was jointly organized by scientists from the Institut für Kernphysik of the Jülich Center for Hadron Physics, Forschungszentrum Jülich, and the Universities Bonn, Bochum and Gießen. The summer school was financed by Forschungszentrum Jülich, the Helmholtz International Center for FAIR, the Transregio TR16 (Subnuclear Structure of Matter) funded by the Deutsche Forschungsgemeinschaft (DFG) and the Collaborative Research Center CRC110 (Symmetries and the Emergence of Structure in QCD) funded by DFG and National Natural Science Foundation of China (NSFC). For more detailed information, see http://collaborations.fz-juelich.de/ikp/hpss2014/index.shtml.

Fig. 65: Participants and organisers of the HPSS2014 at the conference venue Schloss Rauischholzhausen of the University of Gießen.

H.4 PANDA LI. Collaboration Meeting at FZ-Jülich

The PANDA LI. Collaboration Meeting was hosted by IKP at Forschungszentrum Jülich from December 9-12, 2014 and attracted more than 200 participants. During the first two days, Tuesday and Wednesday, up to 4 parallel sessions, in the mornings and afternoons, served to have in-depth discussions on the various aspects the collaboration is working on. The parallel sessions were con-

Fig. 66: Participants of the PANDA LI. Collaboration Meeting.

vened by the respective working groups, including instrumentation and the physics sessions, namely, 'electromagnetic processes', 'hyperons', and 'charmonium, exotics, open charm and electroweak'. This part of collaboration meeting includes technical and collaboration board meetings and the Young Scientists Convent. The plenary sessions were opened on Thursday afternoon by Prof.Dr.-Ing. Wolfgang Marquardt (Chairperson Forschungszentrum Jülich). The ceremony featured the unveiling of a 1:10 model of the PANDA detector. Among the in-

Fig. 67: Unveiling 1:10 model of the PANDA detector by Prof. W. Marquardt (right) and Prof. J. Ritman (left).

vited speakers was the spokesperson of the CLAS12 collaboration, D. Ireland (Glasgow), who elaborated on the upcoming experiments at Jefferson Lab and on possible common physics issues.

I Teaching Positions

Institute	Name	University
IKP-1	PD Dr. A. Gillitzer	Bonn
	PD Dr. F. Goldenbaum	Wuppertal
	Prof. Dr. J. Ritman	Bochum
	PD Dr. S. Schadmand	Köln
	Dr. T. Stockmanns	Bochum
IKP-2	Prof. Dr. D. Gotta	Köln
	Prof. Dr. Dr. h.c. H. Ströher	Köln
	Prof. Dr. J. Pretz	Aachen
IKP-3/IAS-4	Univ. Doz. Dr. J. Haidenbauer	Graz
	Prof. Dr. C. Hanhart	Bonn
	Prof. Dr. S. Krewald	Bonn
	Prof. Dr. T. Luu	Bonn
	Prof. Dr. U.-G. Meißner	Bonn
	Dr. A. Nogga	Bonn
	PD Dr. A. Wirzba	Bonn
IKP-4	Prof. Dr. M. Bai	Bonn
	Prof. Dr. A. Lehrach	Aachen
	Prof. Dr. Dr. h.c. R. Maier	Bonn

J Personnel

J.1 Scientific Staff

Msc Z. Bagdasarian (IKP-2)

Prof. Dr. M. Bai (IKP-4) (since 1st December 2014)

Dr. U. Bechstedt (IKP-4)

DP L. Bianchi (IKP-1) (since 17th March 2014)

Dr. C. Böhme (IKP-4 since September 2014)

DI N. Bongers (IKP-4)

DI R. Brings (IKP-4) (until 31st March 2015)

DP J. Bsaisou (IKP-3/IAS-4)

DI A. Cebulla (IKP-1)

DP M. Cleven (IKP-3/IAS-4) (until 31st January 2014)

Dr. C. Constantinou (since 1st April 2014)

DI F.U. Dahmen (IKP-4)

DP D. Deermann (IKP-1)

Dr. J. de Vries (IKP-3/IAS-4)

Dr. R. Engels (IKP-2)

DP I. Engin (IKP-4)

Dr. S. Esch (IKP-1)

DI F.-J. Etzkorn (IKP-4)

Dr. O. Felden (IKP-TA)

M. Gaißer (IKP-2) (until 30th April 2014)

Dr. R. Gebel (IKP-4)

PD Dr. A. Gillitzer (IKP-1)

DP A. Goerres (IKP-1)

PD Dr. F. Goldenbaum (IKP-1)

Prof. Dr. D. Gotta (IKP-2)

Dr. F. Grümmer (IAS-4) (until 30th September 2014)

Dr. D. Grzonka (IKP-1)

DI W. Günther (IKP-4) (until October 2014)

Univ. Doz. Dr. J. Haidenbauer (IKP-3/IAS-4)

Prof. Dr. C. Hanhart (IKP-3/IAS-4)

Dr. M. Hartmann (IKP-2)

Dr. F. Hauenstein (IKP-1) (since 1st September 2014)

Dr. V. Hejny (IKP-2)

DP N. Hempelmann (IKP-2) (since 1st November 2014)

DP A. Herten (IKP-1)

DP J.-H. Hetzel (IKP-4) (since 1st April 2014)

DP F. Hinder (IKP-4)

DP A. Holler (IKP-4) (until 31st May 2014)

J. Hu (IKP-3/IAS-4) (since 17th November 2014)

MSc M. Jabua (IKP-2)

Dr. A. Kacharava (IKP-2)

Dr. I. Keshelashvilli (IKP-2) (since 1st July 2014)

Dr. V. Kamerdzhiev (IKP-4)

X. Kang (IKP-3/IAS-4)

Prof. Dr. T. Katayama (IKP-4) (until 28th Februar 2014)

C. Körber (IKP-3/IAS-4) (since 1st November 2014)

Prof. Dr. S. Krewald (IKP-3/IAS-4)

Dr. T. Lähde (IKP-3/IAS-4)

Prof. Dr. A. Lehrach (IKP-4)

DP S. Leiber (IKP-1) (until 16th June 2014)

Dr. D. Lersch (IKP-1)

Dr. N. Li (IKP-3/IAS-4)

Dr. S. Liebig (IKP-3)

Dr. B. Lorentz (IKP-4)

Dr. B. Lu (IKP-3/IAS-4)

Prof. Dr. Th. Luu

Prof. Dr. R. Maier (IKP-4)

P. Matuschek (IKP-3/IAS-4) (since 15th August 2014)

Prof. Dr. U.-G. Meißner (IKP-3/IAS-4)

Dr. S. Merzliakov (IKP-2)

DP S. Mey (IKP-4)

DP S. Mikirtytchiants (IKP-2)

Dr. A. Naß (IKP-2)

Dr. A. Nogga (IKP-3/IAS-4)

H. Ohannessian (IKP-1) (since 1st April 2014)

Dr. H. Ohm (IKP-2)

Dr. D. Prasuhn (IKP-4)

Dr. E. Prencipe (IKP-1)

PD Dr. F. Rathmann (IKP-2)

DI M. Retzlaff (IKP-4)

DI A. Richert (IKP-4)

Prof. Dr. J. Ritman (IKP-1)

Dr. E. Roderburg (IKP-1)

DP D. Rönchen (IKP-3) (until 28th February 2014)

DP M. Rosenthal (IKP-4)

PD Dr. S. Schadmand (IKP-1)

M. Schever (IKP-1) (since 1st November 2014)

Dr. R. Schleichert (IKP-2)

DI G. Schug (IKP-4)

Dr. Th. Sefzick (IKP-TA)

Prof. Dr. Y. Senichev (IKP-4)

Dr. V. Serdyuk (IKP-1)

Dr. A. Shindler (IKP-3/IAS-4)

DI M. Simon (IKP-4)

Dr. R. Stassen (IKP-4)

Dr. H. Stockhorst (IKP-4)

Dr. T. Stockmanns (IKP-1)

Prof. Dr. Dr. h. c. H. Ströher (IKP-2)

Msc. M. Thelen (IKP-4)

Dr. R. Tölle (IKP-4)

N. Vaidya (IKP-3/IAS-4) (since 22th September 2014)

DI T. Vashegyi (IKP-4)

Dr. Q. Wang (IKP-3/IAS-4)

DP P. Weiß (IKP-2)

Dr. P. Wintz (IKP-1)

PD Dr. A. Wirzba (IAS-4)

DI J.-D. Witt (IKP-4)

C. Xiao (IKP-3/IAS-4) (since 1st October 2014)

Dr. H. Xu (IKP-1)

Dr. D.-L. Yao (IKP-3/IAS-4)

Dr. E. Zaplatin (IKP-4)

DP M. Zurek (IKP-2)

DP D. Zyuzin (IKP-4) (until 30th September 2014)

J.2 Technical and Administrative Staff

C. Berchem (IKP-TA)

M. Böhnke (IKP-4)

P. Brittner (IKP-4)

J. But (IKP-TA)

W. Classen (IKP-4)

M. Comuth-Werner (IKP-TA)

B. Dahmen (IKP-4)

C. Deliege (IKP-4)

G. D'Orsaneo (IKP-2)

R. Dosdall (IKP-1)

C. Ehrlich (IKP-4)

A. Erben (IKP-2) (until 22nd September 2014)

B. Erkes (IKP-4)

H.-W. Firmenich (IKP-TA)

N. Giese (IKP-TA) (since 15th September 2014)

J. Göbbels (IKP-TA)

T. Hahnraths-von der Gracht (since 1st* February 2014)

R. Hecker (IKP-4)

E. Heßler (IKP-TA) (until 31st December 2014)

M. Holona (IKP-TA)

A. Kelleners (IKP-TA)

A. Kieven (IKP-4)

S. Kistemann (IKP-TA)

B. Klimczok (IKP-TA) (since 15th September 2014)

M. Kremer (IKP-TA)

G. Krol (IKP-4)

M. Küven (IKP-4)

K.-G. Langenberg (IKP-4)

J. Lumbeck (IKP-4) (until 31st July 2014)

H.-P. May (IKP-4) (since Dezember 1st 2014)

C. Müller (IKP-TA) (since 1st February 2014)

S. Müller (IKP-TA)

R. Nellen (IKP-TA) (until 31st December 2014)

D. Prothmann (IKP-TA) (since 19th June 2014)

H. Pütz (IKP-4)

K. Reimers (IKP-4)

A. Richert (IKP-4)

G. Roes (IKP-TA)

N. Rotert (IKP-4)

D. Ruhrig (IKP-4)

F. Scheiba (IKP-4)

H. Schiffer (IKP-TA)

M. Schmühl (IKP-4)

J. Schumann (IKP-1)

H. Simonsen (IKP-TA)

D. Spölgen (IKP-2)

G. Sterzenbach (IKP-1)

J. Strehl (IKP-TA)

J. Uehlemann (IKP-1)

H. Zens (IKP-4)

IKP-1 = Experimental Hadron Structure
IKP-2 = Experimental Hadron Dynamics
IKP-3 = Theory of the Strong Interactions
IKP-4 = Large-Scale Nuclear Physics Equipment
IKP-TA = Technical Services and Administration
IAS-4 = Theory of the Strong Interactions

K Further Contributions

articles available on-line: http://www.fz-juelich.de/ikp/DE/Service/Download/download_node.html

- Analyzing Power of Proton, Kaon, and Lambda in the $\vec{p}p \to pK\Lambda$ Reaction at 2.7 GeV/c
- Developing a Free-Running Readout ASIC for the MVD Strip Sensors
- Simulated Measurement of the D_s Semileptonic Decay Form Factor with the $\overline{\text{P}}$ANDA Detector
- GPU-based Online Tracking Algorithms for the PANDA Experiment
- FEE-free signal processing system for PANDA Straw Tube Tracker
- Test Beam with a PANDA Trapezoidal Prototype Sensor
- Data Analysis of the KOALA Experiment Commissioning at COSY
- Search for polarization effects in the antiproton production process
- Measurement of the analyzing power in $p(pol)d$ elastic scattering at small angles
- The quasi-free reaction $pd \to d + \eta + p_{sp}$ close to threshold at ANKE
- Luminosity determination via dp-elastic scattering at ANKE
- The quasi-free pn-elastic scattering measurements at ANKE
- Investigation of Dipion Final State Interactions in $pp \to pp\eta[\eta \to \pi^+\pi^-\gamma]$ with WASA-at-COSY
- Charge symmetry breaking in the $dd \to {}^4\text{He}\pi^0$ reaction with the WASA-at-COSY experiment
- Investigation of total cross section structures in the $pd \to {}^3\text{He}\eta$ reaction with WASA-at-COSY
- Search for C-violation in the Decay $\eta \to \pi^0 e^+ e^-$ at WASA-at-COSY
- Studying the reaction $pd \to {}^3\text{He}\pi^0$ with WASA-at-COSY
- ToPix 4 Readout System and Test Beam Measurements
- Systematic studies of spin dynamics at COSY in preparation for the EDM searches
- Systematic error investigation of the spin tune analysis for an EDM measurement at COSY
- Development of a new control framework for lattice parameter calculations and particle tracking
- Wien filter studies in MODE
- Upgrade of the Low Energy Polarimeter read-out
- Data Interface between COSY and EDDA-DAQ System
- Beam Position Monitors for the HESR
- Upgrade of the beam profile monitoring system in the COSY IBL
- Automated Compensation of Larmor Rotation in the 2 MeV Electron Cooler
- An RF Wien-filter for EDM Searches at COSY